NUMERICAL SIMULATIONS AND PREDICTIVE MODELS OF UNDRAINED PENETRATION IN SOFT SOILS

A Dissertation

by

HAN SHI

Submitted to the Office of Graduate Studies of
Texas A&M University
in partial fulfillment of the requirements for the degree of

DOCTOR OF PHILOSOPHY

August 2005

Major Subject: Civil Engineering

NUMERICAL SIMULATIONS AND PREDICTIVE MODELS OF UNDRAINED PENETRATION IN SOFT SOILS

A Dissertation

by

HAN SHI

Submitted to the Office of Graduate Studies of
Texas A&M University
in partial fulfillment of the requirements for the degree of

DOCTOR OF PHILOSOPHY

Approved by:

Chair of Committee,	Charles Aubeny
Committee Members,	James D. Murff
	J. N. Reddy
	Harry Hogan
Head of Department,	David Rosowsky

August 2005

Major Subject: Civil Engineering

ABSTRACT

Numerical Simulations and Predictive Models of Undrained
Penetration in Soft Soils. (August 2005)
Han Shi, B.S., China University of Geosciences;
M.S., China University of Geosciences
Chair of Advisory Committee: Dr. Charles Aubeny

There are two aspects in this study: cylinder penetrations and XBP (Expendable Bottom Penetrometer) interpretations. The cylinder studies firstly investigate the relationship between the soil resisting force and penetration depth by a series of rate-independent finite element analyses of pre-embedded penetration depths, and validate the results by upper and lower bound solutions from classical plasticity theory. Furthermore, strain rate effects are modeled by finite element simulations within a framework of rate-dependent plasticity. With all forces acting on the cylinder estimated, penetration depths are predicted from simple equations of motion for a single particle. Comparisons to experimental results show reasonable agreement between model predictions and measurements.

The XBP studies follow the same methodology in investigating the soil shearing resistance as a function of penetration depth and velocity by finite element analyses. With the measurements of time decelerations during penetration of the XBP, sediment shear strength profile is inferred from a single particle kinetic model. The predictions compare favorably with experimental measurements by vane shear tests.

ACKNOWLEDGMENTS

This research was sponsored by the Office of Naval Research and its support is gratefully acknowledged.

I would like to express my sincere gratitude to my advisor, Dr. Charles Aubeny, for his invaluable guidance, encouragement and assistance throughout this research. It was a pleasure and privilege working with him. I also greatly appreciate the tremendous help from Dr. Don Murff during my study. I would also like to thank Dr. J. N. Reddy and Dr. Harry Hogan for serving as the advisory committee.

I would like to extend my thanks to all my friends, and special thanks to Zhigang Yao, for helping me on this research. Finally, I would like to thank my family for their enduring love and support.

TABLE OF CONTENTS

Page

CHAPTER

LIST OF FIGURES

FIGURE Page

FIGURE Page

FIGURE Page

LIST OF TABLES

CHAPTER I

INTRODUCTION [*]

1.1 Scope of Study

This dissertation presents the results of numerical studies that were conducted to develop predictive models for depth of penetration of cylinders in soft sediments and undrained shear strength characterization from impact penetrometer deceleration measurements. The two aspects in this study (cylinder penetration and strength characterization) are independent yet closely related to each other in applications and methodologies.

Prediction of penetration of cylinders into soft soils is relevant to a number of applications, including offshore pipeline burial (Murff et al., 1989; Schapery and Dunlap, 1984) and penetration of a catenary riser at its touchdown point (Willis and West, 2001). In naval mine-clearing operations, prediction of the degree of mine burial into seafloor sediments is a key aspect of mine detection and removal.

Estimation of undrained shear strength of soft seafloor sediments near the mudline is of interest to a number of seafloor engineering applications including burial predictions of objects impacting the seafloor (Chu et al, 2004; Aubeny and Shi, 2005a), analysis of submarine pipeline penetration (Murff et al., 1989), and characterizing

---

This dissertation follows the style and format of *Journal of Geotechnical and Geoenviromental Engineering*.

[*] Part of this chapter is reprinted with permission of ASCE from “Collapse loads for a cylinder embedded in trench in cohesive soil.” by C. P. Aubeny, H. Shi and J. D. Murff, 2005, *International Journal of Geomechanics*, ASCE, scheduled to be published in the 2005.

sediment stiffness in the touchdown zone of catenary risers used by the offshore petroleum industry (Bridge et al., 2004). Sampling and strength testing of soft sediments near the mudline can present considerable challenges due to their low shear strength, sometimes less than 1 kPa. Further, the applications noted above often require strength characterization over a large area extent, which can render conventional seafloor characterization approaches such as quasi-static penetration tests prohibitively expensive or infeasible. In this study we investigate the possibility of estimating sediment shear strength from measurements from penetrometers that fall through a water column and penetrate to shallow depths in the seafloor. Penetrometers that can be deployed from a moving vessel, such as the Expendable Bottom Penetrometer (XBP), are particularly attractive, as they have the potential for providing a relatively inexpensive means of obtaining shallow sediment strengths over a wide area.

Figures 1.1 and 1.2 illustrate the two penetrating objects considered in this research. The cylinder is assumed to be infinitely long, i.e., plane strain conditions are considered, and the XBP is axisymmetric in geometry. Moreover, the cylinder is assumed to be horizontal and the XBP is vertical. When the penetrating object contacts the seafloor it will begin to decelerate in a manner controlled by the net effect of its own weight, the buoyant resistance of the soil, and the shearing resistance of the soil. Pertinent aspects of the problems include: (1) a soil bearing resistance factor that increases with penetration depth, (2) disturbance of the soil due to the large penetration strains, (3) soil shearing resistance that depends on strain rate and therefore penetration velocity, and (4) variable conditions of penetration velocity. A rigorous analysis of these problems involves considerable complexity, including large strains, large deformations, and a contact boundary condition. The simplified approach presented herein provides a means for evaluating collapse load conditions for a penetrating object pre-embedded at a series of penetration depths. Such an approach neglects the large strain aspects of the problem; nevertheless, comparisons of collapse loads predicted from this procedure to experimental measurements (Murff et al., 1989) indicate that the simplified approach can produce realistic estimates of soil resistance. A vertical trench is assumed to form in the wake of the advancing object when the object penetrates past its maximum section (Figures 1.1 and 1.2). This assumption is not entirely consistent with some of the collapse mechanisms considered in this study. However, it is a reasonable assumption for shallow penetrations, and experimental data show open trenches forming above penetrating cylinders to depths of about two to three diameters even in very soft soils having undrained shear strengths on the order of 1 kPa (Aubeny and Dunlap, 2003).

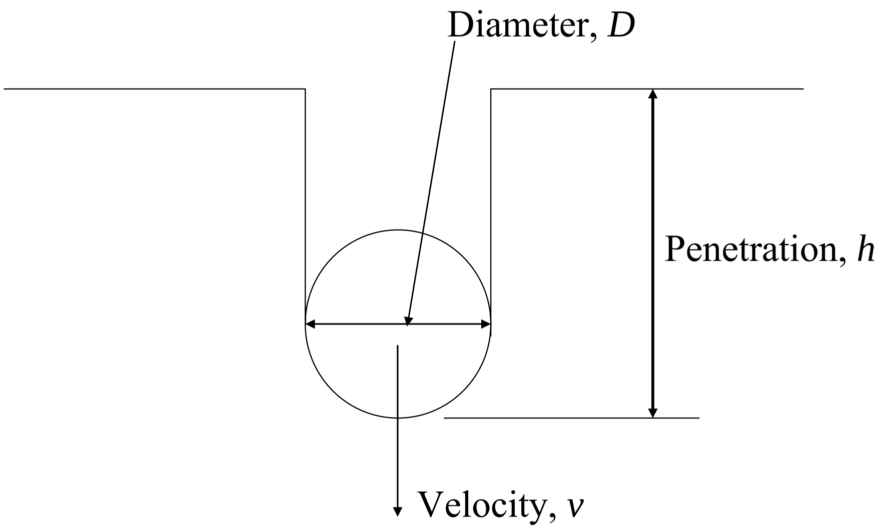

Figure 1.1 Definition Sketch of Penetrating Cylinder (after Aubeny and Shi, 2005a)

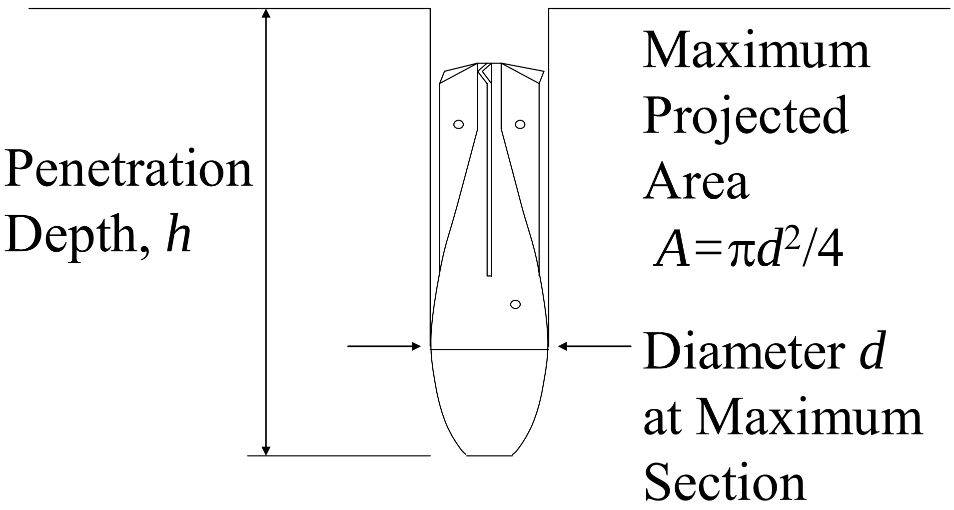

Figure 1.2 Definition Sketch of Penetrating XBP (Aubeny and Shi, 2005b)

Traditional bearing capacity theory for shallow foundations (e.g., Terzaghi, 1943) can not be applied to this research directly because of the non-linear soil-object contact boundary. A simplified approach can be taken assuming an equivalent solution of a strip footing with the width equal to the chord of embedded object at shallow embedment (Small et al., 1971; Ghazzaly and Lim, 1975). In my opinion, this approach over-simplifies the problem and it is not utilized in this research. The strain path method (SPM; Baligh 1985) for deep penetration problems is also not directly applicable since the penetrating objects are still in proximity to the free surface. Given all the considerations above, the finite element method (FEM) was used as a major analytical tool for this research. Additionally, plastic limit analysis methods were used to compare with the results of the FEM.

1.2 Objectives

The objectives of this research may be summarized as follows:

1. Calculate collapse loads for undrained penetration of the cylinder and the XBP in soft soils;
2. Evaluate the strain rate effects on the collapse loads;
3. Develop predictive models for penetration depth of cylinders and strength characterization from dynamic measurements of the XBP.

1.3 Outline of Research

This research consists of three components: rate-independent studies, rate-dependent studies and predictive models.

In the first step we calculate collapse loads for a penetrating object at a series of penetration depths for quasi-static undrained loading conditions, i.e., the strain rate dependence of soil strength is not considered at this stage. Through this step, the relationship between collapse loads and penetration depths is established.

The second step starts from the FEM simulations in the previous step, with the primary refinement being the incorporation of strain rate-dependent shearing resistance into the collapse load calculations. The rate-dependent solutions are then evaluated with reference to the rate-independent solutions. Through this step, the relationship between collapse loads and penetration velocities is established.

The last step develops simplified predictive models. With the soil shearing resistance force defined by the collapse loads as a function of penetration depth and penetration velocity, accelerations can be determined at any instant of time for a penetrating object from simple equations of motion for a rigid body projectile. The penetration depth can then be evaluated through direct integration. On the other hand, with the measurements of accelerations at any given time, the soil shearing resistance force can be inferred and the soil shear strength can be obtained through back-calculation. The predictive models were further calibrated against experimental measurements.

CHAPTER II

BACKGROUND[*]

2.1 Plasticity Concepts

Plasticity theory is a very important tool in soil mechanics and it has been applied extensively. A central concept in plasticity theory is the yield condition, which is a relationship among stress components at which yield starts to occur (Murff, 2002). The yield condition can be written as

$$f(\sigma_{ij}) = 0 \tag{2.1}$$

where σ_{ij} is the stress tensor, representing the six independent components of the stress at a point (i = 1 to 3 and j = 1 to 3).

For undrained condition of purely cohesive soils, possible yield conditions include the von Mises condition and the Tresca condition. The von Mises condition is formulated as

$$J_2^{1/2} - k = 0 \tag{2.2a}$$

where J_2 is the second invariant of the stress deviation tensor, and k is a constant. Written in terms of principal stresses

$$J_2 = \frac{1}{6}[(\sigma_1 - \sigma_2)^2 + (\sigma_2 - \sigma_3)^2 + (\sigma_3 - \sigma_1)^2] \tag{2.2b}$$

where σ_1, σ_2 and σ_3 are major, intermediate, and minor principal stresses, respectively.

---

[*] Part of this chapter is reprinted with permission of ASCE from "Collapse loads for a cylinder embedded in trench in cohesive soil." by C. P. Aubeny, H. Shi and J. D. Murff, 2005, *International Journal of Geomechanics*, ASCE, scheduled to be published in the 2005.

The Tresca condition is written as

$$\frac{\sigma_1 - \sigma_3}{2} = c \tag{2.3}$$

where c is soil undrained shear strength. For plane strain conditions the two yield functions above have an identical form (Murff, 2002).

There are two different kinds of material models in plasticity theory: perfectly plastic and work hardening. Figure 2.1 illustrates an example of these two models. For a perfectly plastic material, stress remains constant and strains increase indefinitely once at yield, whereas stresses continue to increase beyond yield for a work hardening material. If the yield surface in stress space expands symmetrically in all directions it is called isotropic hardening (Murff, 2002).

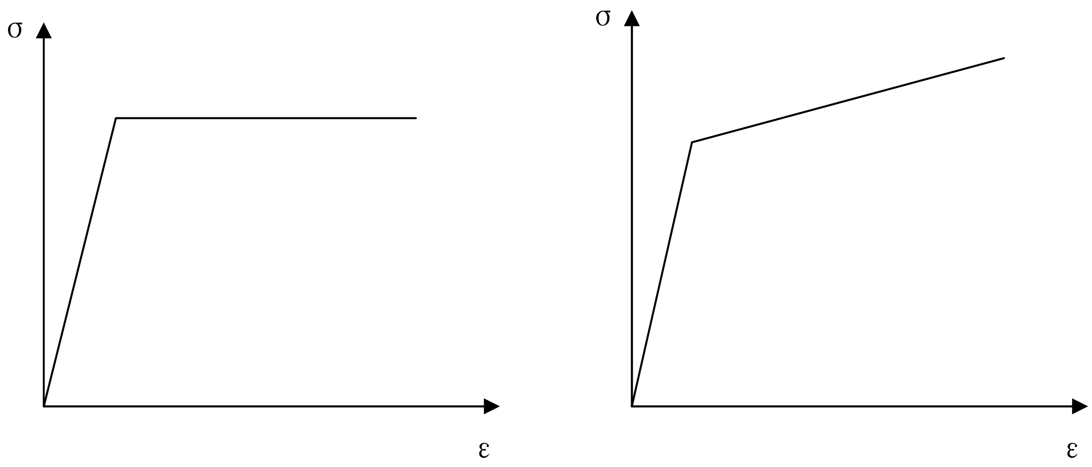

a. Elastic-Perfectly Plastic

b. Work Hardening Plastic

Figure 2.1 Plastic Material Models

The plastic strain increment of a material obeying an associated flow rule is given as (Drucker and Prager, 1952)

$$\dot{\varepsilon}_{ij}^{p} = \lambda \frac{\partial f}{\partial \sigma_{ij}} \tag{2.4}$$

where λ = a positive scalar multiplier

f = the plastic potential which is assumed to be the yield function

σ_{ij} = the corresponding stress

2.2 Plastic Limit Methods

There are two very important plastic limit theorems in estimating collapse loads: the upper bound theorem and the lower bound theorem. The upper bound theorem states: “if an estimate of the plastic collapse load of a body is made by equating internal rate of dissipation of energy to the rate at which external forces do work in any postulated (kinematically admissible) mechanism of deformation of the body, the estimate will be either high or correct” (Calladine, 1969). The lower bound theorem states: “if any stress distribution throughout the structure can be found which is everywhere in equilibrium internally and balances certain external loads and at the same time does not violate the yield condition, those loads will be carried safely by the structure” (Calladine, 1969). This provides a means of estimating the collapse load which is less than or equal to the true value. If a solution based on both bound theorems yields the same result, then it is the exact solution.

2.2.1 Lower Bound Method

First we will look at the method of characteristic (MOC). For a plane strain condition we can write the equations of equilibrium as

$$\frac{\partial \sigma_x}{\partial x} + \frac{\partial \tau_{xy}}{\partial y} = \gamma_x \tag{2.5a}$$

$$\frac{\partial \tau_{xy}}{\partial x} + \frac{\partial \sigma_y}{\partial y} = \gamma_y \tag{2.5b}$$

where σ_x, σ_y are normal stresses in the *x* and *y* direction, τ_{xy} is the shear stress on the *x* and *y* planes, γ_x and γ_y are body forces in the *x* and *y* directions.

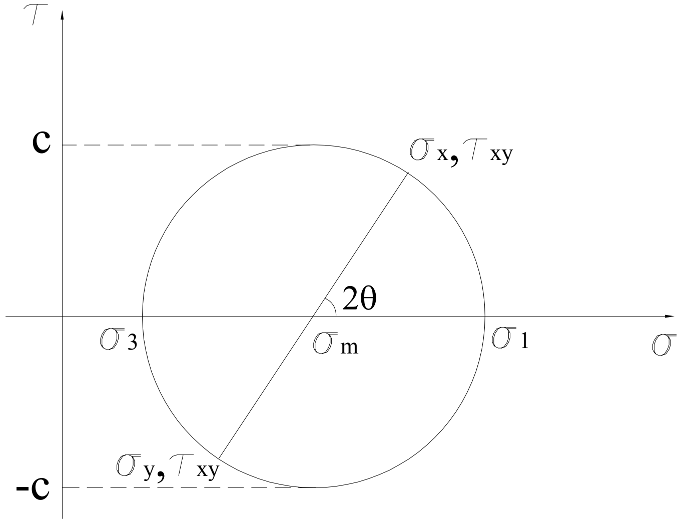

Figure 2.2 Mohr's Circle and Failure Condition (after Murff, 2003)

The soil will also satisfy the yield criterion. For an undrained condition we can write the yield condition as follows, referring to the Mohr's circle (Figure 2.2)

$$(\frac{\sigma_x - \sigma_y}{2})^2 + \tau_{xy}{}^2 = c^2 \tag{2.6}$$

To simplify the problem we define the mean stress σ_m as

$$\sigma_m = \frac{1}{2}(\sigma_x + \sigma_y) \tag{2.7}$$

Furthermore, we define another variable θ which is the angle between major principal stress σ_1 and the *x* axis.

The following relations can be established from the Mohr's circle (Figure 2.2)

$$\sigma_x = \sigma_m + c\cos 2\theta \tag{2.8a}$$

$$\sigma_y = \sigma_m - c\cos 2\theta \tag{2.8b}$$

$$\tau_{xy} = c\sin 2\theta \tag{2.8c}$$

Substituting the above relations into the equilibrium equations, we get

$$\frac{\partial\sigma_m}{\partial x} - 2c\sin 2\theta\frac{\partial\theta}{\partial x} + 2c\cos 2\theta\frac{\partial\theta}{\partial y} = \gamma_x - \cos 2\theta\frac{\partial c}{\partial x} - \sin 2\theta\frac{\partial c}{\partial y} \tag{2.9a}$$

$$\frac{\partial\sigma_m}{\partial y} + 2c\sin 2\theta\frac{\partial\theta}{\partial y} + 2c\cos 2\theta\frac{\partial\theta}{\partial x} = \gamma_y + \cos 2\theta\frac{\partial c}{\partial y} - \sin 2\theta\frac{\partial c}{\partial x} \tag{2.9b}$$

It can be shown that (e.g., Sokolovskii, 1965) two sets of equations comprise characteristics sets of Eqs. 2.9a and 2.9b. These are designated as α and β characteristics. The corresponding equations are as follows:

On an α characteristic

$$\frac{dy}{dx} = \tan(\theta - \frac{\pi}{4}) \tag{2.10a}$$

$$d\sigma_m - 2cd\theta = (\gamma_x - \frac{\partial c}{\partial y})dx + (\gamma_y + \frac{\partial c}{\partial x})dy \tag{2.10b}$$

On a β characteristic

$$\frac{dy}{dx} = \tan(\theta + \frac{\pi}{4}) \tag{2.10c}$$

$$d\sigma_m + 2cd\theta = (\gamma_x + \frac{\partial c}{\partial y})dx + (\gamma_y - \frac{\partial c}{\partial x})dy \tag{2.10d}$$

In the above four equations we have four unknowns which are x, y, σ_m and θ. In some simple cases we can get closed-form solutions, but generally the equations must be solved numerically.

As an example we will consider a case of a smooth strip footing, and we assume that $\gamma_x, \gamma_y = 0$ and $c = c_m + c_1 y$, where c_m and c_1 are constants. Consider a point on the free surface in Figure 2.3. At the free surface the vertical stress $\sigma_3 = 0$ and the horizontal stress $\sigma_1 = \sigma_3 + 2c = 2c$, therefore $\sigma_m = \frac{\sigma_1 + \sigma_3}{2} = c$ and $\theta = 0$. Substitute $\theta = 0$ into Eqs. 2.10a and 2.10c we get $\frac{dy}{dx} = \mp 1$ for α and β characteristics respectively, which means the characteristics at the free surface emanate at an angle of $\mp \frac{\pi}{4}$ and intersect at $\frac{\pi}{2}$. Therefore, the characteristics in this zone are straight and form a triangular region in which θ is constant. For uniform strength case ($c_1 = 0$), from Eq. 2.10b we have

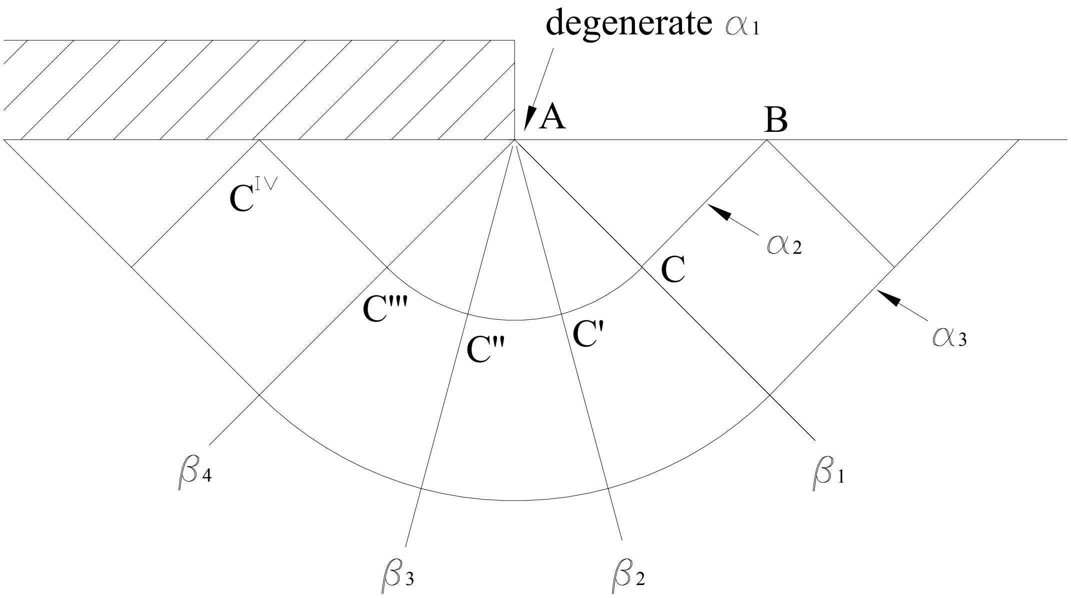

Figure 2.3 Illustration of the Method of Characteristics

$$d\sigma_m = 2cd\theta = 0 \tag{2.11}$$

Therefore σ_m is a constant in this region and it equals *c*.

On the other hand, we consider a point immediate under the footing (Figure 2.3). Assuming the pressure at the footing boundary is σ_0, the vertical stress at the boundary is then $\sigma_1 = \sigma_0$, and the horizontal stress is $\sigma_3 = \sigma_1 - 2c = \sigma_0 - 2c$. So $\sigma_m = \frac{\sigma_1 + \sigma_3}{2} = \sigma_0 - c$ and $\theta = \frac{\pi}{2}$. Substitute $\theta = \frac{\pi}{2}$ into Eqs. 2.10a and 2.10c we get $\frac{dy}{dx} = \pm 1$ for α and β characteristics respectively, which means the characteristics at the footing boundary emanate at an angle of $\frac{\pi}{4}$ and $\frac{3}{4}\pi$ and intersect at $\frac{\pi}{2}$. Therefore, another triangular region forms under the footing. For uniform strength case σ_m is constant in this region and it equals $\sigma_0 - c$.

The region in between these two triangular regions is generally a shear fan. For uniform strength case, the β characteristics are straight and the α characteristics are circular (Murff, 2003). Apparently there is a discontinuity of σ_m at point A, and the change in θ through the shear fan is $\pi - \frac{\pi}{4} - \frac{\pi}{4} = \frac{\pi}{2}$ (Figure 2.3). From Eq. 2.10b we have

$$\vartriangle\sigma_m = 2c\vartriangle\theta = c\pi \tag{2.12}$$

Therefore the change in mean stress across the shear fan is $c\pi$. Recalling that σ_m in the left and the right triangular regions are c and $\sigma_0 - c$ respectively, we have

$$\sigma_0 - c = c + c\pi \tag{2.13}$$

$$\sigma_0 = c(\pi + 2) \tag{2.14}$$

For the non-uniform strength case ($c_1 \neq 0$), we can solve for the collapse load by numerical methods. Consider point A and point B at the free surface in Figure 2.3. At point A and point B the four variables $\sigma_{m,}\theta, x$ and y are all known, so we can then write the following difference equations (Murff, 2003):

On an α characteristic

$$y_C - y_B = (x_C - x_B)\tan(\frac{\theta_C + \theta_B}{2} - \frac{\pi}{4}) \tag{2.15a}$$

$$\sigma_{mC} - \sigma_{mB} - 2(\frac{c_C + c_B}{2})(\theta_C - \theta_B) = -c_1(x_C - x_B) \tag{2.15b}$$

On a β characteristic

$$y_C - y_A = (x_C - x_A)\tan(\frac{\theta_C + \theta_A}{2} + \frac{\pi}{4}) \tag{2.15c}$$

$$\sigma_{mC} - \sigma_{mA} + 2(\frac{c_C + c_A}{2})(\theta_C - \theta_A) = -c_1(x_C - x_A) \tag{2.15d}$$

By combining the above difference equations we can develop recursive relations as follows:

$$x_C = \frac{y_B - y_A + x_A T_{CA} - x_B T_{CB}}{T_{CA} - T_{CB}} \tag{2.16a}$$

$$y_C = \frac{1}{2}[(y_B + y_A) + (x_C - x_B)T_{CB} + (x_C - x_A)T_{CA}] \tag{2.16b}$$

$$\theta_C = \frac{\sigma_{mA} - \sigma_{mB} + 2c_{CB}\theta_B + 2c_{CA}\theta_A + c_1(2x_C - x_A - x_B)}{2c_{CA} + 2c_{CB}} \tag{2.16c}$$

$$\sigma_{mC} = \frac{1}{2}[\sigma_{mA} + \sigma_{mB} + 2c_{CB}(\theta_C - \theta_B) - 2c_{CA}(\theta_C - \theta_A) + c_1(x_B - x_A)] \tag{2.16d}$$

where $T_{CA} = \tan[(\frac{\theta_A + \theta_C}{2}) + \frac{\pi}{4}]$

$$T_{CB} = \tan[(\frac{\theta_B + \theta_C}{2}) - \frac{\pi}{4}]$$

$$c_{CA} = (c_C + c_A)/2$$

$$c_{CB} = (c_C + c_B)/2$$

We can start by assuming $\theta_C = \theta_B$ on the α characteristic and $\theta_C = \theta_A$ on the β characteristic, then we can calculate x_C , y_C, θ_C and σ_{mC} in turn. Substitute the new values into the above equations and recycle until the values of x_C, y_C, θ_C and σ_{mC} are within tolerance (e.g., 10^{-6} for θ_C in this study). The change in θ across the shear fan is $\frac{\pi}{2}$. We can divide it into a number of increments, and integrate the mean stress along the α characteristics.

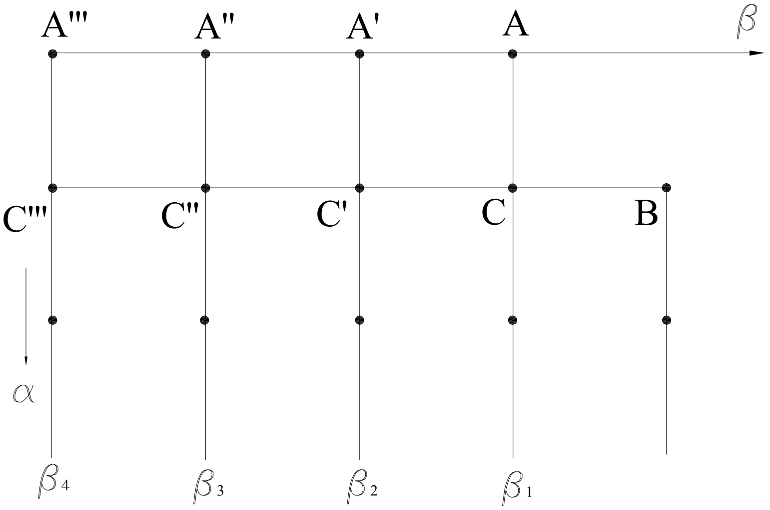

Figure 2.4 Mapped Rectangular Grids of the Radial Fan (Murff, 2003)

Figure 2.4 illustrates the mapped rectangular grids of the radial fan shown in Figure 2.3. The point A in Figure 2.3 is a degenerate α characteristic. We divide the fan into n increments (3 as shown here), so $\Delta\theta = \frac{\theta}{n}$. The degenerate α characteristics A', A'' and A''' have the same x, y coordinates, and θ at A', A'' and A''' are $\Delta\theta$, $2\Delta\theta$, and $3\Delta\theta$ respectively. The mean stresses at A', A'' and A''' can be determined by the following difference equations:

$$\sigma_m(A') = \sigma_m(A) + 2c\Delta\theta \tag{2.17a}$$

$$\sigma_m(A'') = \sigma_m(A') + 2c\Delta\theta \tag{2.17b}$$

$$\sigma_m(A''') = \sigma_m(A'') + 2c\Delta\theta \tag{2.17c}$$

From the conditions at A' and C we can solve for the conditions (x, y, θ, σ_m) at C' using the previously described recursive method. Then we can solve for the conditions at C'' and C''' along the α characteristics.

The point C^{IV} under the footing is a boundary on an α characteristic but not on a β characteristic. We know y and θ at C^{IV} so we can solve the two unknown variables x and σ_m by the two α equations:

$$x_{C^{IV}} = \frac{y_{C^{IV}} - y_{C'''} + x_{C'''}\tan(\frac{\theta_{C'''} + \theta_{C^{IV}}}{2} - \frac{\pi}{4})}{\tan(\frac{\theta_{C^{IV}} + \theta_{C'''}}{2} - \frac{\pi}{4})} \tag{2.18a}$$

$$\sigma_{mC^{IV}} = \sigma_{mC'''} + 2(\frac{c_{C'''} + c_{C^{IV}}}{2})(\theta_{C^{IV}} - \theta_{C'''}) - c_1(x_{C^{IV}} - x_{C'''}) \tag{2.18b}$$

The vertical stress σ_0 at C^{IV} is then

$$\sigma_0 = \sigma_{mC^{IV}} + c_0 \tag{2.19}$$

For non-uniform strength case the vertical pressure under the footing is not uniform, therefore we should proceed to the next α characteristic until it reaches the center of the footing. By integrating the vertical stress and multiplying the result by two we can obtain the collapse load.

To establish a solution of the method of characteristic as a lower bound solution, the stress field needs to be extended beyond the slip line field into the rigid zone (e.g. Randolph and Houlsby, 1984). Once this is done the characteristic solution is said to be a rigorous lower bound (Murff, 2002).

2.2.2 Upper Bound Method

To apply the upper bound method, we define the unknown collapse load F moving at a velocity v_0, the external work rate is then $\dot{W} = Fv_0$. We postulate a kinematically admissible failure mechanism and velocity field, and then we compute the internal rate of energy dissipation $\dot{D}$ satisfying the yield condition and the associated flow rule. By equating the external work to the internal energy dissipation $Fv_0 = \dot{D}$, we can obtain the collapse load F as v_0 will cancel out in the equation.

For a material obeying an associated flow rule (Eq. 2.4), the dissipation rate is calculated by

$$\dot{D} = \sigma_{ij}\dot{\varepsilon}_{ij}^{p} = \lambda\sigma_{ij}\frac{\partial f}{\partial \sigma_{ij}} \tag{2.20}$$

For undrained plane strain conditions the yield function can be written as

$$f = [\frac{(\sigma_x - \sigma_y)^2}{4} + \frac{1}{2}\tau_{xy}^2 + \frac{1}{2}\tau_{yx}^2]^{\frac{1}{2}} - c = 0 \tag{2.21}$$

By substituting Eq. 2.21 into Eq. 2.20 and carrying out the dot product operations we can obtain

$$\dot{D} = \lambda c \tag{2.22}$$

Also, by the associated flow rule the strain rates can be calculated as

$$\dot{\varepsilon}_x = \lambda \frac{\partial f}{\partial \sigma_x} = \frac{\lambda}{4c}(\sigma_x - \sigma_y) \tag{2.23a}$$

$$\dot{\varepsilon}_y = \lambda \frac{\partial f}{\partial \sigma_y} = \frac{-\lambda}{4c}(\sigma_x - \sigma_y) \tag{2.23b}$$

$$\dot{\varepsilon}_{xy} = \dot{\varepsilon}_{yx} = \lambda \frac{\partial f}{\partial \tau_{xy}} = \frac{\lambda}{2c}\tau_{xy} \tag{2.23c}$$

We can see that the volumetric strain rate is $\dot{\varepsilon}_v = \dot{\varepsilon}_x + \dot{\varepsilon}_y = 0$, which implies that the material is incompressible for this yield condition. By substituting Eqs. 2.23a, 2.23b and 2.23c into the yield condition (Eq. 2.21) we can solve for λ, which is

$$\lambda = (2\dot{\varepsilon}_x^2 + 2\dot{\varepsilon}_y^2 + 2\dot{\varepsilon}_{xy}^2 + 2\dot{\varepsilon}_{yx}^2)^{1/2} \tag{2.24}$$

Therefore

$$\dot{D} = c(2\dot{\varepsilon}_x^2 + 2\dot{\varepsilon}_y^2 + 2\dot{\varepsilon}_{xy}^2 + 2\dot{\varepsilon}_{yx}^2)^{1/2} \tag{2.25}$$

Since $\dot{\varepsilon}_x = -\dot{\varepsilon}_y$ and $\dot{\varepsilon}_{xy} = \dot{\varepsilon}_{yx}$, Eq. 2.25 is reduced to

$$\dot{D} = 2c(\dot{\varepsilon}_x^2 + \dot{\varepsilon}_{xy}^2)^{1/2} \tag{2.26}$$

For undrained and general three dimensional conditions, the dissipation functions for continuously deforming regions are

von Mises condition:

$$\dot{D} = c(2\dot{\varepsilon}_{ij}\dot{\varepsilon}_{ij})^{1/2} \tag{2.27}$$

Tresca condition:

$$\dot{D} = 2c\left|\dot{\varepsilon}_{\substack{shear\\ \max}}\right| = |\dot{\gamma}|_{\max}\, c \tag{2.28}$$

For slip surfaces, consider the following (Murff, 1978)

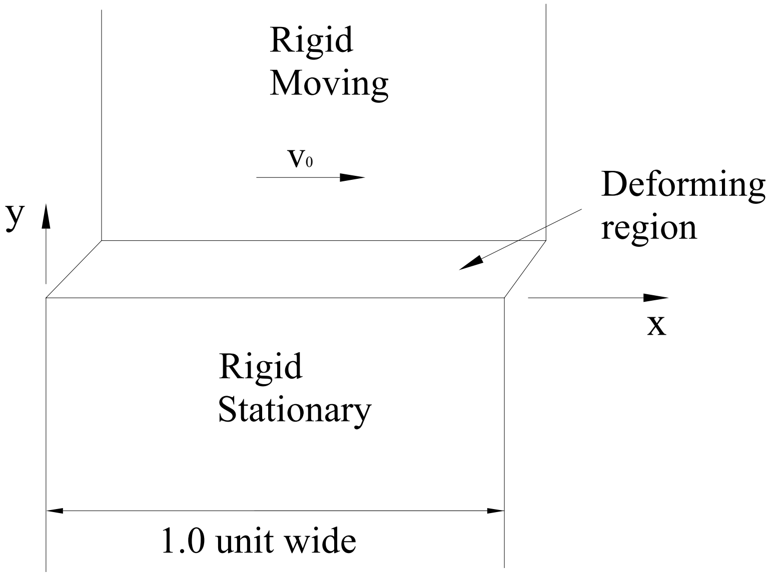

Figure 2.5 Calculation of the Dissipation Rate for Slip Surfaces (after Murff, 2002)

Assuming the thickness of the deforming region is *t*, from Figure 2.5 the velocities in the deforming region can be calculated as

$$v_x = \frac{v_0}{t} y \tag{2.29a}$$

$$v_y = v_z = 0 \tag{2.29b}$$

The strain rates are

$$\dot{\varepsilon}_x = \dot{\varepsilon}_y = 0 \tag{2.30a}$$

$$\dot{\varepsilon}_{xy} = \dot{\varepsilon}_{yx} = \frac{1}{2}\left(\frac{\partial v_x}{\partial y} + \frac{\partial v_y}{\partial x}\right) = \frac{1}{2}\frac{v_0}{t} \tag{2.30b}$$

Therefore, the dissipation is

$$\dot{D} = 2c[(\frac{1}{2}\frac{v_0}{t})^2]^{1/2} = \frac{cv_0}{t} \tag{2.31}$$

The total dissipation in the deforming region is then

$$\dot{D}_{TOT} = \int_V \dot{D} dV = \frac{cv_0}{t} \times 1 \times t = cv_0 \tag{2.32}$$

So as $t \to 0$ the dissipation on the slip surface is simply

$$\dot{D} = cv_0 \tag{2.33}$$

where v_0 is the relative velocity of slip along the slip surface.

To illustrate the application of the upper bound method we will consider the same strip footing problem as the lower bound method and a uniform strength condition. We can develop a failure mechanism (Figure 2.6) from the solution by the method of characteristics. The mechanism can be shown to be kinematically admissible so it constitutes a valid upper bound. Consider the right half of the footing, there are 3 regions: OAD, ABD and BCD. OAD and BCD are rigid regions so no energy is dissipated within them, hence, only the dissipation within region ABD and along slip planes OA, AB and BC need to be evaluated.

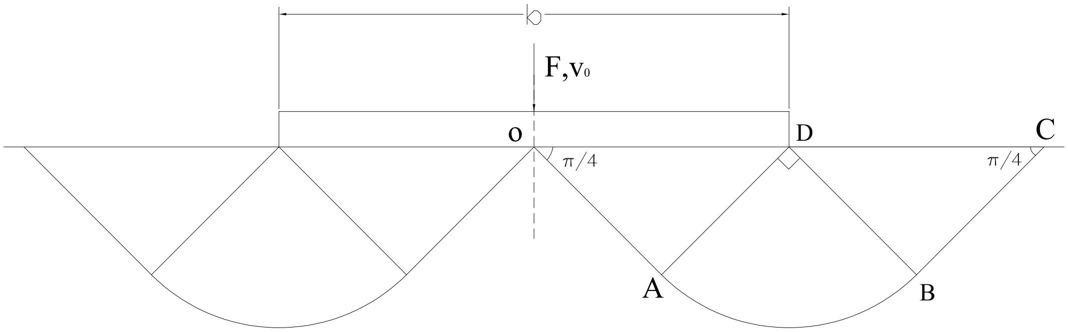

Figure 2.6 Failure Mechanism Developed from MOC

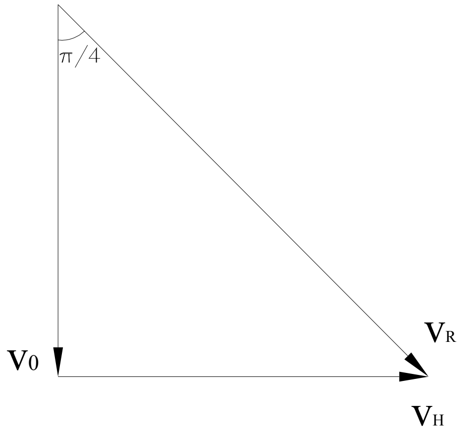

Figure 2.7 The Resultant Velocity along OA

From Figure 2.7 we can see that the resultant velocity along OA is $v_R = v_0 / \cos\frac{\pi}{4} = \sqrt{2}v_0$. The length of OA is $\frac{b}{2}\cos\frac{\pi}{4} = \frac{\sqrt{2}}{4}b$, where b is the width of the footing. Therefore the dissipation along OA is

$$\dot{D} = c \cdot \sqrt{2}v_0 \cdot \frac{\sqrt{2}}{4}b = \frac{cv_0 b}{2} \tag{2.34}$$

The tangential velocity along arc AB is the same as OA, and the length of arc AB is $\frac{\pi}{2} \cdot \frac{\sqrt{2}}{4}b = \frac{\sqrt{2}}{8}\pi b$, thus

$$\dot{D} = c \cdot \sqrt{2}v_0 \cdot \frac{\sqrt{2}\pi b}{8} = \frac{cv_0 \pi b}{4} \tag{2.35}$$

The dissipation rate along BC can be evaluated similarly, which is the same as OA.

The tangential velocity within the region ABD is constant, $v_t = \sqrt{2}v_0$, and the radial velocity is zero, so the shear strain rate is

$$\dot{\gamma} = -(\frac{\partial v_t}{\partial r} - \frac{v_t}{r}) = \frac{\sqrt{2}v_0}{r} \tag{2.36}$$

where r is radius of curvature within this region. Thus

$$\dot{D} = \int_0^{\pi/2} \int_0^{\sqrt{2}b/4} c\frac{\sqrt{2}v_0}{r} r dr d\theta = \frac{cv_0 \pi b}{4} \tag{2.37}$$

where θ is the cylindrical coordinate. Therefore, the total energy dissipation rate is the sum of the calculated dissipations above and multiply by two, which gives

$$\dot{D}_{TOT} = cv_0 b(\pi + 2) \tag{2.38}$$

Equate the external work rate to the internal dissipation rate, we have

$$Fv_0 = cv_0 b(\pi + 2) \tag{2.39}$$

Thus

$$F / b = c(\pi + 2) \tag{2.40}$$

which is the same as the lower bound solution. Therefore, it is the exact solution.

2.2.3 Plasticity Solutions for Fully Embedded Cylinder

Randolph and Houlsby (1984) applied classical plasticity theory to estimate the limiting pressure on a fully embedded, laterally translating, circular cylinder unaffected by any free surface. Their approach employed the method of characteristics (MOC) to estimate a lower bound limiting resistance, and they used the characteristic net found in the lower bound solution to derive the velocity field for a collapse mechanism in an upper bound solution. Figure 2.8 illustrates the characteristic nets for $\alpha = 0$ (smooth pile) and $\alpha = 1$ (rough pile), where α is the interface adhesion coefficient. For the case of full adhesion between the soil and cylinder boundary, α=1, their procedure produces identical lower and upper bound solutions for the normalized collapse load, F/cD = 11.94; i.e., an exact solution. Subsequent study by Murff et al. (1989) indicated some divergence between lower and upper bound solutions for α<1. The maximum discrepancy occurs for the case of a perfectly smooth cylinder, where the upper bound solution exceeds the lower bound (F/cD = 9.14) by about 9%. An optimized upper bound by Randolph et al. (2000) reduces the difference to 5.5% (Figure 2.9).

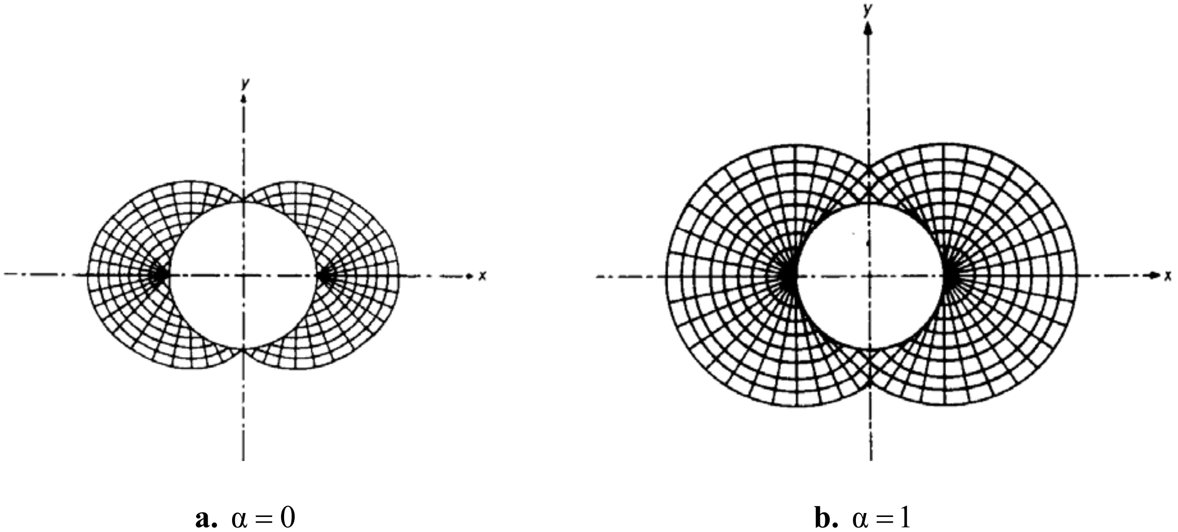

Figure 2.8 Examples of Characteristic Nets by Randolph and Houlsby (1984)

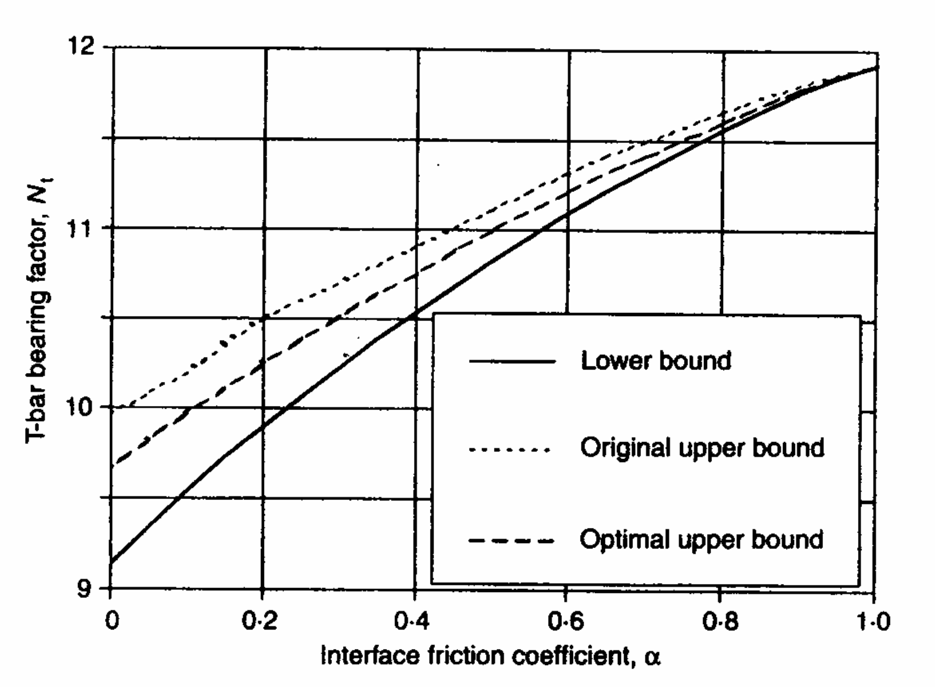

Figure 2.9 Solution for Cylindrical (T-bar) Penetrometer (Randolph et al., 2000)

2.2.4 Plasticity Solutions for Partially Embedded Cylinders

Murff et al. (1989) used the Randolph-Houlsby approach for computing collapse loads for partially embedded cylinders for embedments up to one-half diameter, h/D =0.5. Their characteristic net takes the following form (Figure 2.10):

(a) Rigid zones OAF and DEQ. For a perfectly smooth cylinder ($\alpha = 0$) the rigid zone OAF vanishes.

(b) A circular fan CDQ centered about Q.

(c) Zone ACQF containing curved characteristics comprised of involutes having centers of curvature located on an evolute of radius $r_0 \cos \psi$, where r_0 is the radius of the cylinder, $\psi = \frac{\pi}{4} - \frac{\Delta}{2}$, which is the angle the straight characteristics intersect with the cylinder and Δ =arcsin(adhesion/shear strength).

This net is similar to the Randolph-Houlsby net, except for the rigid wedge DEQ, which arises as a consequence of the free surface.

For uniform soil strength conditions, tractions on the cylinder can be derived analytically by integration along the characteristics. The tractions can further be integrated analytically to obtain the following expressions for collapse load F for embedment such that $\omega < \pi/2 - \Delta/2$ provided by Murff et al.:

$$F = 2r_0 c\left[\cos(\omega+\Delta) + 2\sin\frac{\Delta}{2} + (1+\Delta+2\omega)\cos\omega + 2\cos\frac{\Delta}{2} - 2\sin\omega\right] \tag{2.41}$$

where $\omega = \arcsin(1 - h/r_0)$

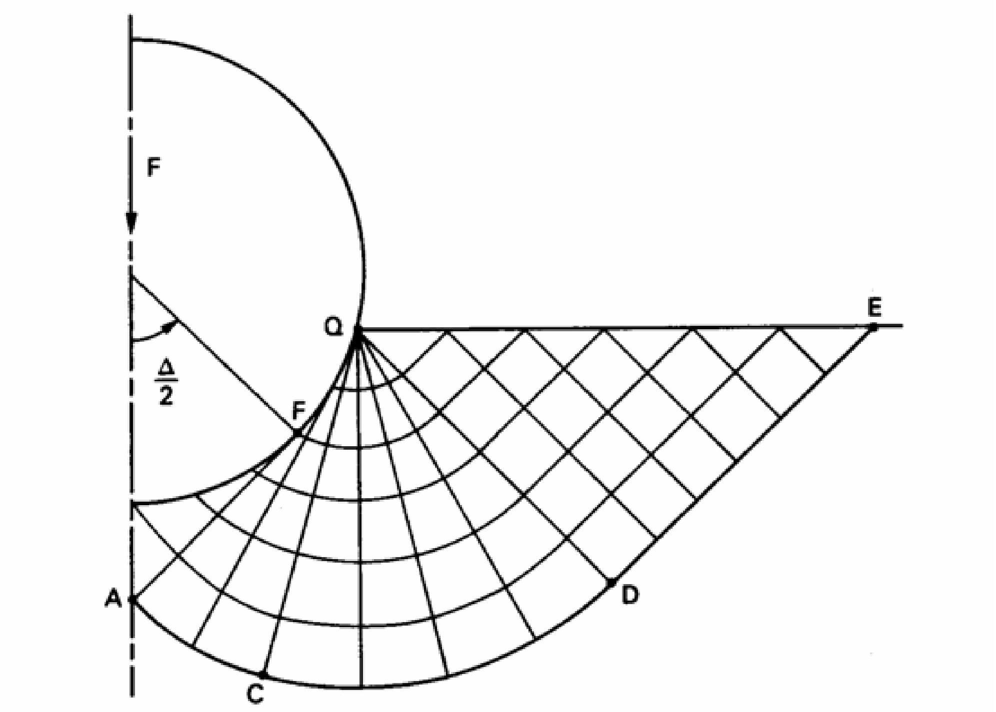

Figure 2.10 Characteristic Net for Uniform Strength (after Murff et al., 1989)

For shallow embedments $\omega > \pi/2 - \Delta/2$, this expression becomes:

$$F = 2r_0c(2 + \pi)\cos\omega \tag{2.42}$$

The Murff et al. solution (1989) can be extended beyond the slip line field to the rigid region. Hence, their solution constitutes a rigorous lower bound.

For upper bound estimates of a collapse load for a partially embedded cylinder, Murff et al. (1989) consider two velocity fields for estimation of collapse loading for a partially embedded cylinder. The first is the velocity field implied by the consistent stress characteristic net shown in Figure 2.11a. The second is the velocity field obtained by truncating at the ground surface the velocity field used in the Randolph-Houlsby analysis for a fully embedded cylinder far from a free surface (Figure 2.11b). Both of the above mechanisms contain velocity jumps across slip planes as well as continuously deforming regions. Both velocity fields considered above are kinematically admissible mechanisms; hence, collapse loads derived from them are valid upper bounds.

The energy dissipation rates across the slip planes and deforming regions were evaluated by Murff et al. (1989). Referring to Figure 2.11a, AFF ' is a rigid zone, interface AF is inclined at 45 degrees to the vertical direction. The tangential velocity along AF is $v_t = v_0 / \sqrt{2}$, therefore

$$\dot{D} = c v_0 r_0 \sin(\frac{\Delta}{2}) \tag{2.43}$$

Interface ABC is an involute, with the center moving anticlockwise along the evolute, which is a circle of radius $r_0 \cos\psi$ concentric with the cylinder. The tangential velocity along ABC is $v_t = v_0 / \sqrt{2}$, so the dissipation rate along the interface is

$$\dot{D} = \int_{\omega}^{\pi/2-\Delta/2} c \frac{v_0}{\sqrt{2}} r d\theta_2 \tag{2.44}$$

where *r* is the radius of curvature of ABC, and

$$r = r_0[\sqrt{2}\sin(\frac{\Delta}{2}) + \sin\psi + (\frac{\pi}{2} - \frac{\Delta}{2} - \theta_2)\cos\psi] \tag{2.45}$$

θ_2 locates specific straight characteristic.

Interface CD is a circular arc centered at Q. The tangential velocity along CD is $v_t = v_0 / \sqrt{2}$, therefore

$$\dot{D} = \int_{\pi/4}^{\pi/4+\Delta/2+\omega} c \frac{v_0}{\sqrt{2}} r d\theta_3 \tag{2.46}$$

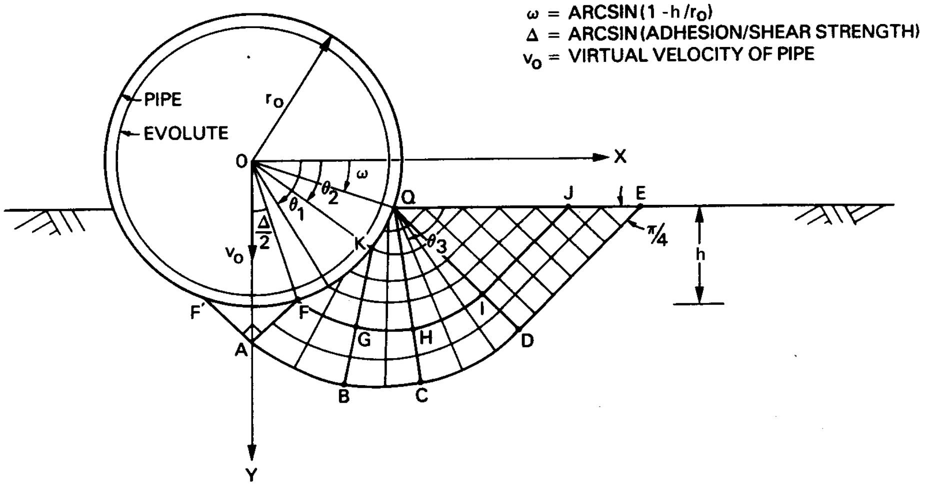

a. Consistent Upper Bound Model

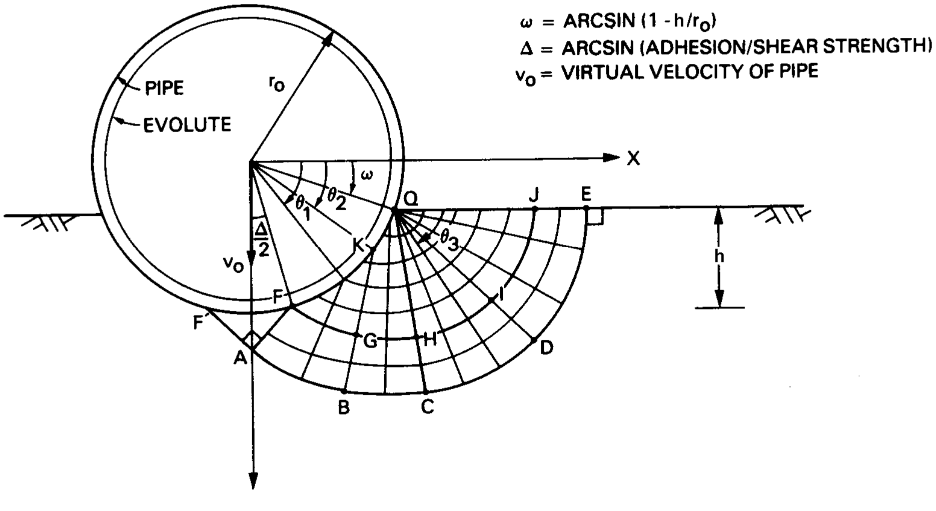

b. Randolph and Houlsby Upper Bound Model

Figure 2.11 Upper Bound Models (Murff et al., 1989) where r is the radius of curvature of CD, and

$$r = r_0[\sqrt{2}\sin(\frac{\Delta}{2}) + (\frac{\pi}{2} - \frac{\Delta}{2} - \omega)\cos\psi] \tag{2.47}$$

θ_3 locates specific straight characteristic.

Interface DE is inclined at 45 degrees to the free surface so its length is the same as QD, which is equal to $r_0[\sqrt{2}\sin(\frac{\Delta}{2}) + (\frac{\pi}{2} - \frac{\Delta}{2} - \omega)\cos\psi]$. The tangential velocity along CD is $v_t = v_0 / \sqrt{2}$**,** therefore

$$\dot{D} = v_0 c r_0[\sin(\frac{\Delta}{2}) + (\frac{\pi}{2} - \frac{\Delta}{2} - \omega)\cos\psi / \sqrt{2}] \tag{2.48}$$

Interface FGH is an involute similar to ABC. A tangential velocity discontinuity exists across FGH equal to

$$\vartriangle v_t = v_0[\cos(\Delta/2)\sec\psi - 1/\sqrt{2}] \tag{2.49}$$

Thus

$$\dot{D} = \int_{\omega}^{\pi/2-\Delta/2} c \vartriangle v_t r d\theta_2 \tag{2.50}$$

where *r* is the radius of curvature of FGH, and $r = r_0[\sin\psi + (\frac{\pi}{2} - \frac{\Delta}{2} - \theta_2)\cos\psi]$.

Interface HI is a circular arc similar to CD. A tangential velocity discontinuity same as FGH exists across HI, therefore

$$\dot{D} = \int_{\pi/4}^{\pi/4+\Delta/2+\omega} c \vartriangle v_t r d\theta_3 \tag{2.51}$$

where *r* is the radius of curvature of HI, and $r = r_0(\frac{\pi}{2} - \frac{\Delta}{2} - \omega)\cos\psi$.

Interface IJ is inclined at 45 degrees to the free surface, and its length is the same as QI, which is equal to $r_0(\frac{\pi}{2}-\frac{\Delta}{2}-\omega)\cos\psi$. The velocity discontinuity across IJ is identical to FGH and HI, therefore

$$\dot{D}=v_0 c r_0[\cos(\frac{\Delta}{2})-\frac{\cos\psi}{\sqrt{2}}](\frac{\pi}{2}-\frac{\Delta}{2}-\omega) \tag{2.52}$$

For Interface FKQ, the relative velocity between the cylinder and the soil is

$$\vartriangle v_t = v_0(\cos\theta_1+\sin\theta_1\tan\psi) \tag{2.53}$$

The limiting shear stress or adhesion at the soil cylinder interface is $c\sin\Delta$. Thus

$$\dot{D}=\int_{\omega}^{\pi/2-\Delta/2} c\sin\Delta \vartriangle v_t r_0 d\theta_1 \tag{2.54}$$

where θ_1 locates a specific curved characteristic.

The straight characteristics KGB, QHC and QID all terminate in the rigid region, therefore no relative velocity develop along them and the energy dissipations are zeros.

Within the deforming region ABCHGF, the tangential velocity is $v_0/\sqrt{2}$, and the radial velocity is zero, so the shear strain rate is

$$\dot{\gamma}=-(\left.\frac{\partial v_t}{\partial r}\right|_{\theta_2}-\frac{v_t}{r})=\frac{v_0}{r\sqrt{2}} \tag{2.55}$$

where r is the radius of curvature in each deforming region. Therefore

$$\dot{D}=\int_{\omega}^{\pi/2-\Delta/2}\int_{r_1}^{r_2}\frac{cv_0}{r\sqrt{2}}r dr d\theta_2 \tag{2.56}$$

where the radial integration limits r_1 and r_2 denote the radius of curvature along FGH and ABC, respectively.

For region CDIH, the tangential velocity and the shear strain rate are in the same form as within region ABCHGF, thus

$$\dot{D} = \int_{\pi/4}^{\pi/4+\Delta/2+\omega} \int_{r_1}^{r_2} \frac{cv_0}{r\sqrt{2}} r dr d\theta_3 \tag{2.57}$$

where r_1 and r_2 denote the radii of curvature along HI and CD, respectively.

Region DEJI is a rigid zone, so the dissipation within it is zero. For region FGHQK, the tangential velocity along the curved characteristics is $\triangle v_t = v_0 \sin\theta_1 / \cos\psi$, and the radius of curvature in the region is $r = r_0[\sin\psi + (\theta_1 - \theta_2)\cos\psi]$, so the shear strain rate is

$$\dot{\gamma} = -(\left.\frac{\partial \triangle v_t}{\partial r}\right|_{\theta_2} - \frac{\triangle v_t}{r}) = -(\frac{v_0 \cos\theta_1}{r_0 \cos^2\psi} - \frac{v_0 \sin\theta_1}{r\cos\psi}) \tag{2.58}$$

Thus

$$\dot{D} = \int_{\omega}^{\pi/2-\Delta/2} \int_{\omega}^{\theta_1} c\dot{\gamma} r r_0 \cos\psi d\theta_2 d\theta_1 \tag{2.59}$$

For region HIQ, the tangential velocity and the shear strain rate are in the same form as within region FGHQK, i.e., $\dot{\gamma} = -(\frac{v_0 \cos\theta_1}{r_0 \cos^2\psi} - \frac{v_0 \sin\theta_1}{r\cos\psi})$, but the radius of curvature is $r = r_0(\theta_1 - \omega)\cos\psi$. Similarly we have

$$\dot{D} = \int_{\omega}^{\pi/2-\Delta/2} \int_{\pi/4}^{\pi/4+\Delta/2+\omega} c\dot{\gamma} r r_0 \cos\psi d\theta_3 d\theta_1 \tag{2.60}$$

For region IJQ, a new set of axes is taken to facilitate the calculation. Q is the new origin and y ' runs along QID. The tangential velocity along the straight characteristics is

$$v_{x'} = v_0 \sin\theta_1 / \cos\psi \tag{2.61}$$

Recalling that $y' = r_0(\theta_1 - \omega)\cos\psi$, the shear strain rate becomes

$$\dot{\gamma} = \frac{\partial v_{x'}}{\partial y'} + \frac{\partial v_{y'}}{\partial x'} = \frac{v_0 \cos\theta_1}{r_0 \cos^2\psi} \tag{2.62}$$

Thus

$$\dot{D} = \int_{\omega}^{\frac{\pi}{2}-\frac{\Delta}{2}} \int_0^{y'} \frac{v_0 \cos\theta_1}{r_0 \cos^2\psi} c r_0 \cos\psi dx' d\theta_1 \tag{2.63}$$

For the Randolph-Houlsby upper bound model, the energy dissipation rates are the same except slip planes IJ, DE and deforming regions DEJI and IJQ (Figure 2.11b). Slip plane DE is a circular arc extended from CD, thus

$$\dot{D} = \int_0^{\pi/4} c \frac{v_0}{\sqrt{2}} r d\theta_3 \tag{2.64}$$

Slip plane is also a circular arc extended from HI, thus

$$\dot{D} = \int_0^{\pi/4} c \Delta v_t r d\theta_3 \tag{2.65}$$

The deforming region DEJI is an extension of region CDIH, thus

$$\dot{D} = \int_0^{\pi/4} \int_{r_1}^{r_2} \frac{c v_0}{r\sqrt{2}} r dr d\theta_3 \tag{2.66}$$

Region IJQ is an extension of the circular shear fan HIQ, thus

$$\dot{D} = \int_{\omega}^{\pi/2-\Delta/2} \int_0^{\pi/4} c \dot{\gamma} r r_0 \cos\psi d\theta_3 d\theta_1 \tag{2.67}$$

By evaluating the integrals and summing all the energy dissipation rates for slip planes and deforming regions together, we obtain the total internal dissipation $\dot{D}_{TOT}$. The external work rate is

$$\dot{W} = F_v v_0 = \dot{D}_{TOT} \tag{2.68}$$

From the equation above we can obtain F_v and the collapse load by multiplying F_v by 2 due to symmetry. Figure 2.12 illustrates the comparison of the upper bound and lower bound solutions by Murff et al.

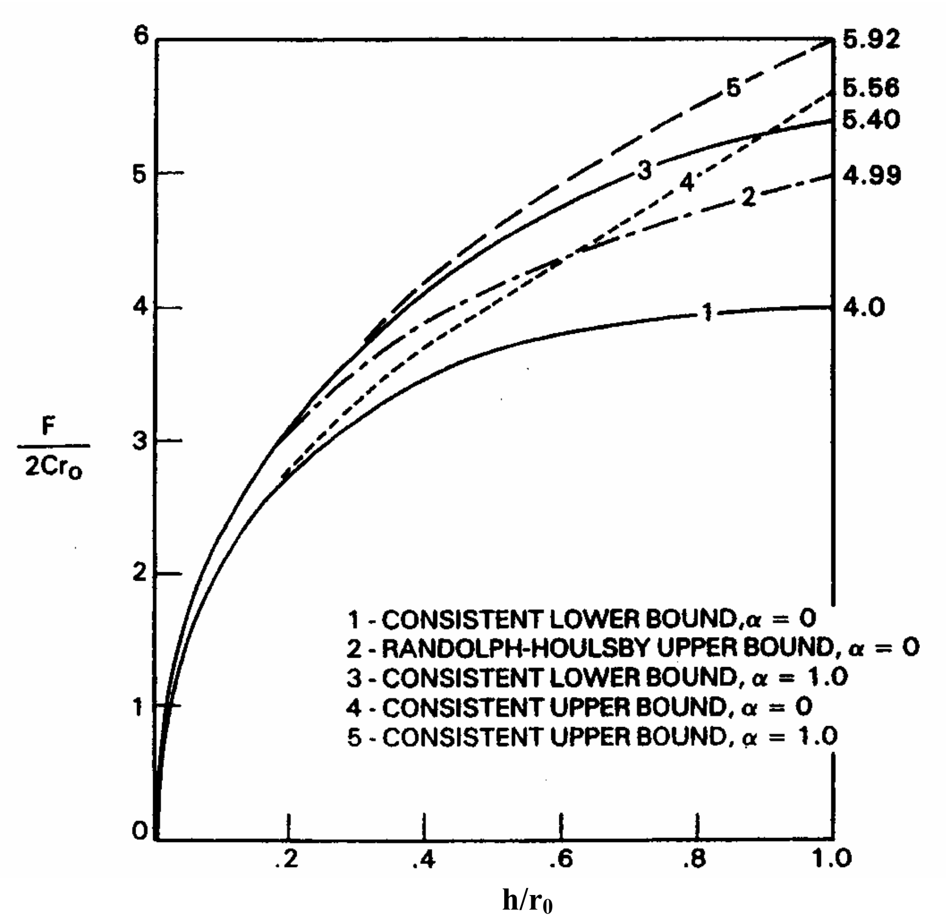

Figure 2.12 Comparison of Lower and Upper Bound Solutions (after Murff et al., 1989)

2.3 Finite Element Method

In essence, the finite element method (FEM) is an approximate method implemented by discretizing the solution domain into a number of “finite elements”. By doing so we can choose interpolation functions and construct approximate equations for each element. We can solve for the unknown variables by assembling all the element equations together and imposing the boundary conditions (Reddy, 1993).

2.3.1 FEM Theory

There are two main reasons to discretize the domain (Reddy, 1993). The first reason is to approximate the geometry, e.g., we can approximate a curve by a set of straight lines. The accuracy of the approximation will depend on the refinement of the mesh. If one keeps increasing the refinement of a mesh, the solution will tend to converge on the exact value. The second reason is to approximate the solution over each element instead of the whole domain, which is more difficult to do.

As an example we will consider a solid mechanics frame work (Aubeny, 2003). The basic solution variable is the displacement vector $[u]$, and the strain-displacement relationship is

$$[\varepsilon]=[B][u] \tag{2.69}$$

where $[B]$ is the strain-displacement operator. The stress-strain relationship can be established as

$$[\sigma]=[C][\varepsilon] \tag{2.70}$$

where [C] is the constitutive matrix. The governing differential equation in tensor form is

$$\nabla \bullet \sigma + f = 0 \tag{2.71}$$

which can also be written as

$$[B]^T[\sigma] = [f] \tag{2.72}$$

where $[f]$ is the externally applied force vector. Combine Eqs. 2.69, 2.70 and 2.72, we obtain the following:

$$[B]^T[C][B][u] - [f] = 0 \tag{2.73}$$

or

$$[K][u] = [f] \tag{2.74}$$

where [K] is the stiffness matrix and $[K] = [B]^T[C][B]$.

In each element, we approximate the displacement by interpolation functions as follows:

$$[u] = [H][\hat{u}] \tag{2.75}$$

where [H] is the interpolation matrix, and $[\hat{u}]$ is the nodal displacement vector. If we multiply the left hand side of Eq. (2.73) by a weighting function matrix $[w] = [H]^T$ we obtain the following:

$$[B]^T[C][B][\hat{u}] - [H]^T[f] = [R] \tag{2.76}$$

where [R] is the residual error term. By the method of weighed residuals (MWR) we integrate it over the element and let it equal zero, which can be written as

$$\int_V [B]^T [C][B][\hat{u}]dV - \int_V [H]^T [f]dV = 0 \tag{2.77}$$

For each element the element stiffness matrix $[K]_e = \int_V [B]^T [C][B]dV$, and the force vector $[F]_e = \int_V [H]^T [f]dV$. Therefore the element equation in matrix form is

$$[K]_e[u] = [F]_e \tag{2.78}$$

The element equations can be assembled together based on the satisfaction of inter-element continuity and equilibrium. The global stiffness matrix and force vector can be written as

$$[K]_G = \sum_{i=1}^{\#elements} [K]_e \tag{2.79}$$

$$[F]_G = \sum_{i=1}^{\#elements} [F]_e \tag{2.80}$$

To solve the assembly equations, the boundary conditions need to be applied for the specific problem, such as a prescribed displacement, an applied load etc. The equations can be solved by mathematical operations. If necessary, the solutions can be post-processed into graphical or tabular presentation.

2.3.2 FEM Studies for Cylinders of Flow-around Conditions

Finite element studies on undrained penetration of rough cylindrical mines in uniform soils were carried forward at Texas A&M University by Yao (2003), with the assumption that the soil will flow around the cylinder after the penetration depth exceeds one half diameter (Figure 2.13). He calculated the quasi-static collapse loads assuming the cylinder is pre-embedded at a series of embedment depths. The analyses used linear, quadrilateral elements for a linearly elastic, perfectly plastic material obeying a von Mises yield criterion and an associated flow rule. Figure 2.13 illustrates his solutions, where $N = \dfrac{F}{cd_c}$, and d_c is the actual projected contact area per unit length.

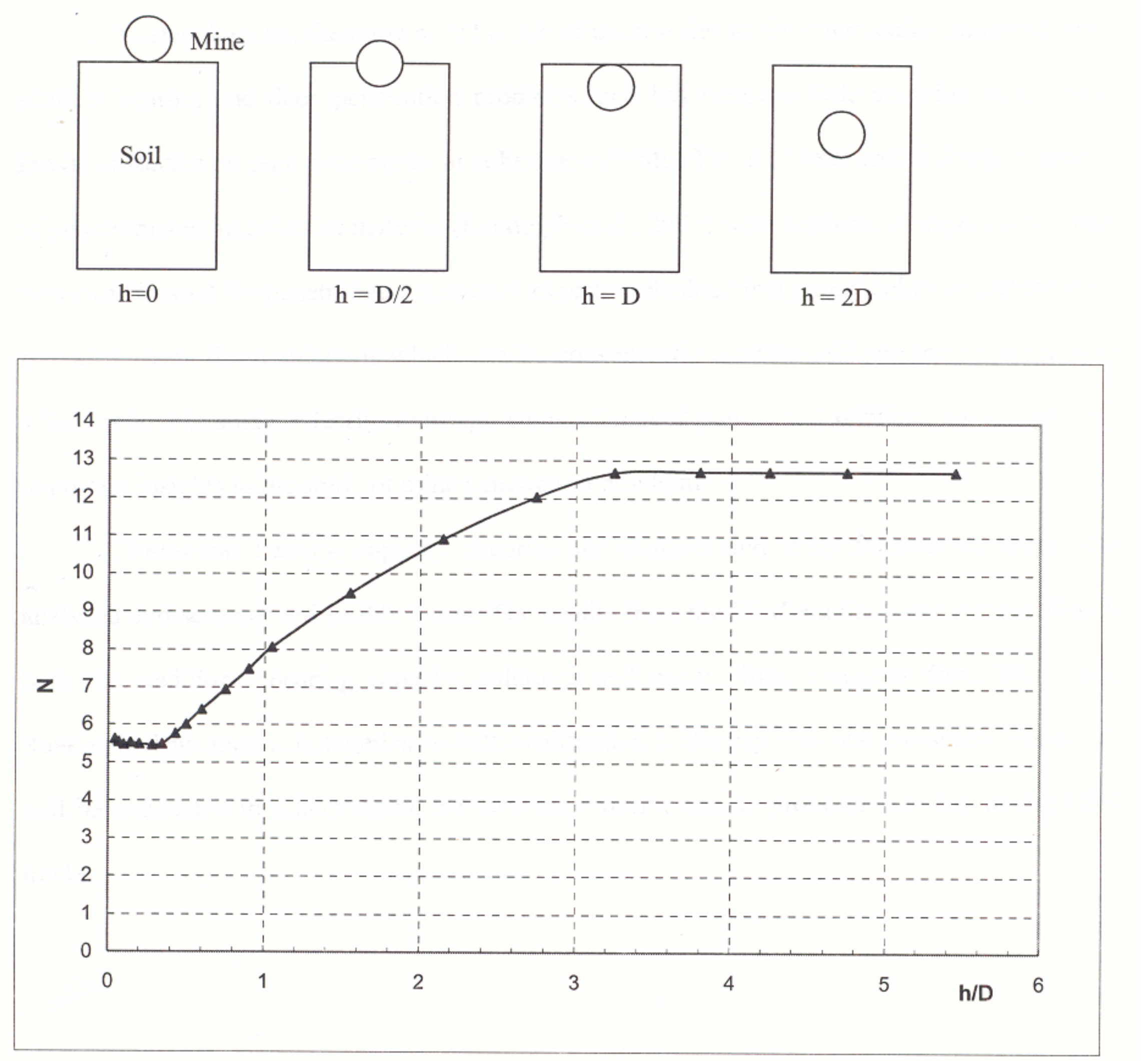

Figure 2.13 FEM Solutions for Cylinders of Flow around Conditions (Yao, 2003)

2.4 Rate Dependent Properties of Soil

The dependence of undrained shear strength of soil on applied rate of strain has long been recognized (Casagrande and Wilson, 1951). Rate dependency of soil on undrained shear strength has been studied extensively both in triaxial compression tests (e.g., Bjerrum et al., 1958; Richardson and Whitman; 1963; Richardson, 1963; Ladd et al., 1972; Alberro and Santoyo, 1973; Berre and Bjerrum, 1973; Vaid and Campanella, 1977; Hight, 1983; Lefebvre and LeBoeuf, 1987; Sheahan et al., 1996) and in vane shear tests (e.g., Skempton, 1948; Cadling & Odenstad, 1950; Aas, 1965; Halwachs, 1972; Wiesel, 1973; Torstensson, 1977; Smith & Richards, 1975; Perlow & Richards, 1977; Schapery & Dunlap, 1978; Sharifounnasab & Ulrich, 1985; Roy & LeBlanc, 1988; Biscontin and Pestana, 2001). The relationship between undrained shear strength and strain rate in triaxial tests is often expressed by a logarithmic relationship (Sheahan et al., 1996), while either a logarithmic or a power law can be formulated in terms of rotation rates in vane shear tests (Biscontin and Pestana, 2001). The Biscontin-Pestana data also suggest that substituting peripheral velocity for rotation rate provides a better basis for interpreting test data from different vane blade radius dimensions.

A possible predictive framework for strain rate dependence is that of a viscous fluid model (e.g., Whitney and Rodin, 2001). Viscous models have been used very effectively in practical applications such as pipeline embedment in soft seafloor soils (Schapery and Dunlap, 1984). This framework has the advantage that the material parameters describing strain rate effects can be estimated from variable strain rate shear tests in a relatively straight-forward manner. A chief disadvantage is that soil shearing resistance decays to negligible levels as penetration velocity approaches zero, which can lead to unrealistic results, depending on the problem.

A second alternative, which was adopted in this research, is a rate-dependent plasticity approach (Aubeny and Shi, 2005a). With this approach, at elevated strain rates soil shearing resistance has a rate-dependent form that is similar to that of a viscous fluid model, but the soil shearing resistance remains constant for strain rates below a certain threshold value. Evidence for this type of behavior is given by Sheahan et al. (1996) for lightly to moderately over-consolidated clay (Figure 2.14). Although no threshold value was established for normally consolidated clay in their study, the overall magnitude of strain rate effects clearly appears to be declining at very low strain rates.

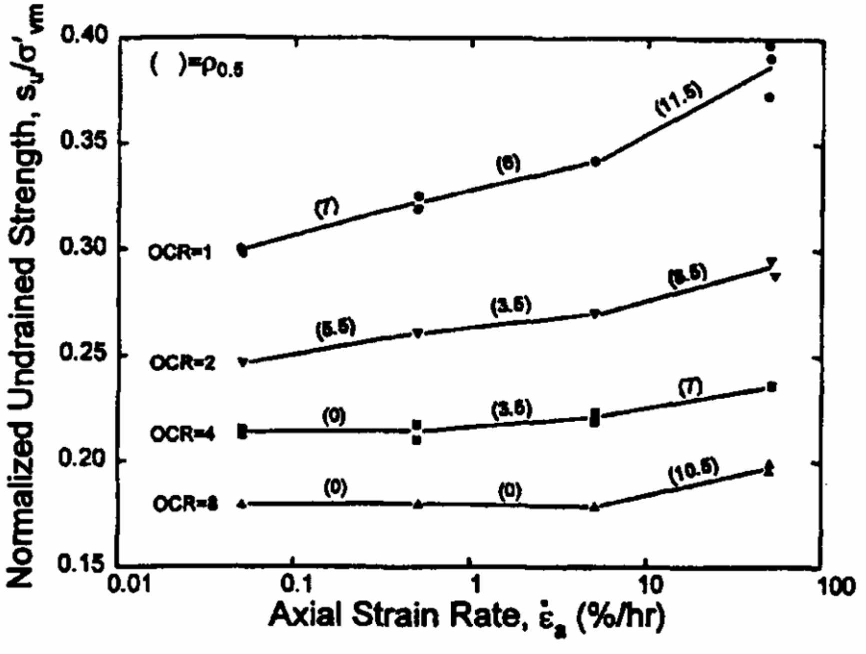

Figure 2.14 Normalized Shear Strength versus Strain Rate, CK_0UC Tests, Resedimented BBC (Sheahan et al., 1996)

An appealing feature of the rate-dependent plasticity approach is that the framework follows naturally from well-established methods for estimating collapse loads from rate-independent plasticity theory. Hence, rate-independent solutions can provide a useful frame of reference from which strain rate effects can be evaluated. A drawback of the approach is that the threshold strain rate is at present ill-defined, and the magnitude of the threshold may in fact be so low that the assumption of undrained shearing no longer becomes valid.

2.5 Experimental Studies

The experimental studies relevant to this research include the mini-vane shear tests, the penetration tests and the XBP tests. The details of these tests and their interpretations are discussed in the following section.

2.5.1 Miniature Vane Shear Tests

The miniature vane (MV) shear test consists of inserting a four-bladed vane into a soil sample and rotating it at a constant rate to determine the maximum torque to be developed (ASTM, 2001). For isotropic materials, the torque can be converted to undrained shear strength by the following equation (Murff, 1980):

$$k = T/(2\pi R^2 L + \frac{4}{3}\pi R^3/\cos \nu) \tag{2.81}$$

where k = undrained shear strength

T = torque

R = radius of the blade

L = height of the vane

ν = angle of vane taper

The MV shear test apparatus used in this study used a 12.6 mm diameter by 18.2 long vane with a 45º taper on top and bottom. The device is equipped with a small variable speed motor to drive the vane shaft, and the readings are taken from a transducer in volts and then converted to torque. Figure 2.15 shows the set-up of the vane shear testing machine.

Figure 2.15 The Vane Shear Testing Machine Set-Up (Munim, 2003)

2.5.2 Penetration Tests

The penetration tests (Aubeny and Dunlap, 2003) involve penetration measurements of a model cylinder for various conditions of cylinder weight and mudline velocity. The soils used in the tests were reconstituted marine clays collected from the Gulf of Mexico seafloor approximately 32 km south of Port Aransas, Texas. The soils were collected using a box core sampler and transported in 0.21-m^3 (55-gal) drums to the laboratory. The natural soils were processed to remove shells, mixed to achieve a uniform mixture, and dried from a water content of about 69% down to 52%. The reconstituted soil had a liquid limit of 44-45 and a plastic limit of 20-22. Given that the water content of the soils was well above the liquid limit, sampling and laboratory strength testing was not practical. Soil strength in the test basin was therefore estimated using a hand-held vane shear apparatus rotated at a rate of 0.02 rad/sec. Typical strengths were on the order of 1-1.5kPa. This test method can not be considered highly accurate, but given the limited options for measuring the strength of shallow, extremely soft soils, the above methods were adopted for characterizing soil strength.

The cylinder penetration tests were performed in a 1.83-m diameter by 1.22-m high basin (Figure 2.16). The tests were performed using a 0.168-m diameter aluminum cylinder. Both ends of the cylinder were rounded with hemispherical caps. The total length of the cylinder, including the rounded caps, was 0.505 m. The cylinder and the guide frame were constructed to permit variation of the weight of the cylinder. In the test program, cylinder weights were varied from 160-750 N. During each test the cylinder was released at the desired drop location and penetration depths versus time were measured by a data acquisition system which was set up with Magneto-restriction Linear Displacement Transducer (MLDT) and Labview hardware and software. Soil strengths were measured after each drop at six locations surrounding the cylinder; hence, the soil strength *c* varied somewhat throughout the test program. Both non-impact and impact tests were performed (Table 2.1). For non-impact tests the cylinder was released at the mudline so the impact velocity $v_0 = 0$. For impact tests involving non-zero mudline velocity v_0, the cylinder was attached to a displacement transducer from which velocity could be computed. The test apparatus permitted inclination of the cylinder to an angle β up to about 20° from horizontal.

Figure 2.16 Penetration Test Basin with Gulf of Mexico Sediments (Yao, 2003)

Table 2.1 Summary of Penetration Tests (after Aubeny and Dunlap, 2003; Munim, 2003)

a. Non-Impact Tests

Test No.	Mine Weight (kg)	Shear Strength (kPa)	Penetration (cm) 1 min	Penetration (cm) 64 min
1	16.61	1.36	1.40	1.75*
5	46.55	1.22	6.96	9.40
7	56.53	1.04	11.23	14.58
8	64.51	1.34	10.80	15.29
9	76.49	1.43	15.49	22.28

* Measurements taken after 60 min

b. Impact Tests

Test No.	Mine Weight (kg)	Shear Strength (kPa)	Impact Velocity (m/sec)	Penetration (cm) 1 sec	Penetration (cm) 24 hrs
22	28.59	1.86	1.82	11.86	12.29
23	46.55	1.20	2.07	21.41	22.02
24	76.49	1.98	1.79	23.60	25.45
25[1]	28.59	1.40	1.69	11.63	12.37
26[1]	46.55	1.39	1.74	20.90	21.54
27[1]	76.49	1.60	1.88	32.05	33.17
28[2]	28.59	1.20	1.91	22.00	22.40
29[2]	46.55	1.46	1.73	21.92	22.73
30[2]	76.49	1.48	1.58	34.85	36.63

1 – Cylinder oriented 10 degrees from horizontal.
2 – Cylinder oriented 20 degrees from horizontal.

For the non-impact tests, data in Table 2.1a indicates the penetration continues to increase significantly after the initial penetration over a long period of time. Figure 2.17 illustrates this behavior for test 9. Possible causes of this additional penetration may include soil consolidation and/or creep (Aubeny and Dunlap, 2003). On the other hand, data in Table 2.1b indicates that only very small additional penetration was developed after the initial impact for the impact tests. Apparently the inertial forces imposed by the dropped cylinders caused penetration near the long term static equilibrium depth.

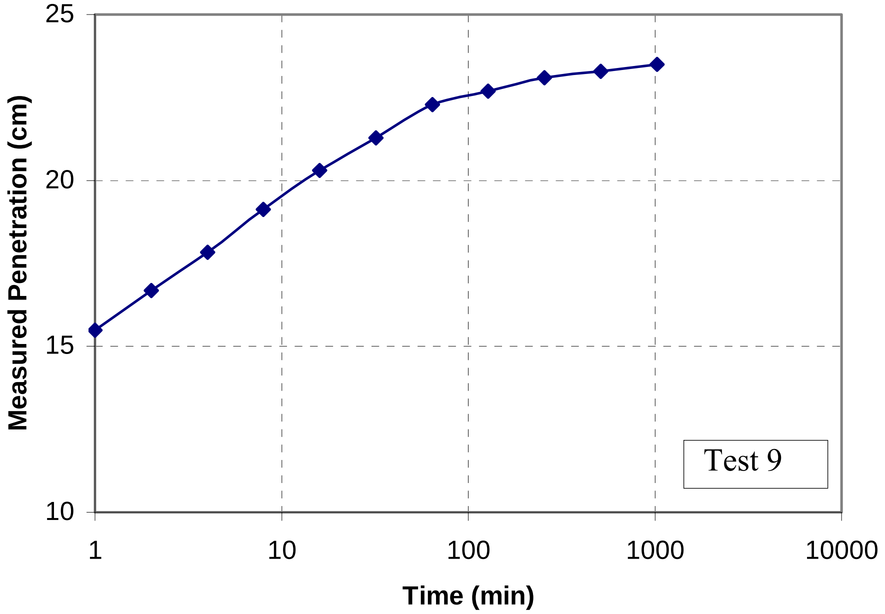

Figure 2.17 Typical Time-Dependent Penetration for Non-Impact Tests (after Aubeny and Dunlap, 2003; Munim, 2003)

2.5.3 XBP Tests

Figure 2.18 illustrates the XBP that is under consideration in this study. It is 21.55 cm long with a maximum diameter of 5.067 cm. Its total and buoyant weights are W = 6.91 N and W_b=5.34 N, respectively. After falling several meters through a water column, it reaches a terminal velocity of approximately 7 m/s (Stoll et al., 2004). The probe is equipped with an accelerometer; decelerations measured upon impact into the seafloor sediment provide a basis for estimating shear strength. Peak decelerations are typically well in excess of 10g, even in the very soft sediments considered in this study. Maximum penetration depths are typically on the order of 25 cm; i.e., about equal to the probe length. As its name implies, the XBP is not retrieved following deployment. A significant advantage of the device is that it can be launched from a moving vessel, making it well suited to expeditiously mapping seafloor sediment conditions over a large area.

The XBP tests were conducted as a part of ONR Mine Burial Program (Stoll et al., 2004) in the Gulf of Mexico near Corpus Christi, Texas. A typical example of an XBP test record is shown in Figure 2.19.

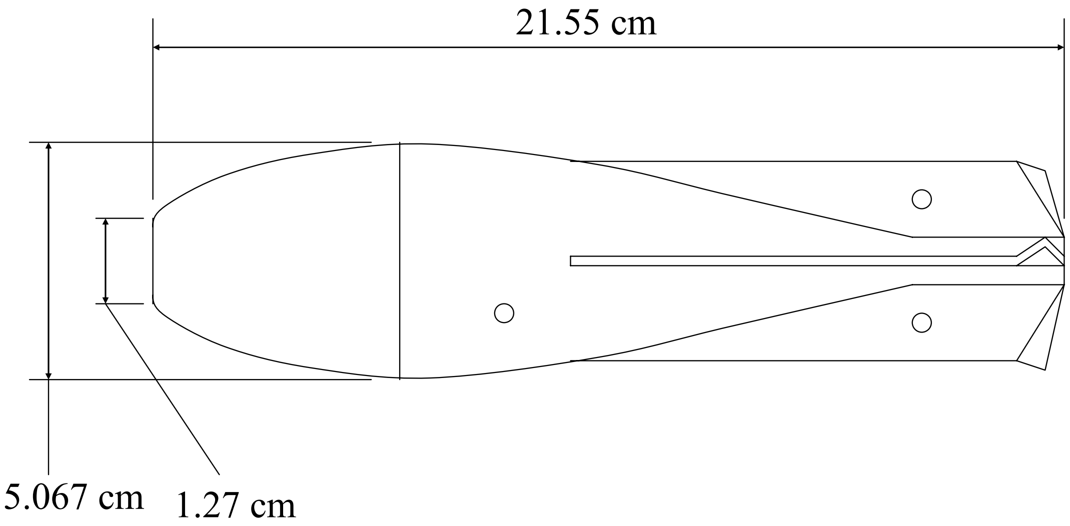

Figure 2.18 Expendable Bottom Penetrometer, XBP (Aubeny and Shi, 2005b)

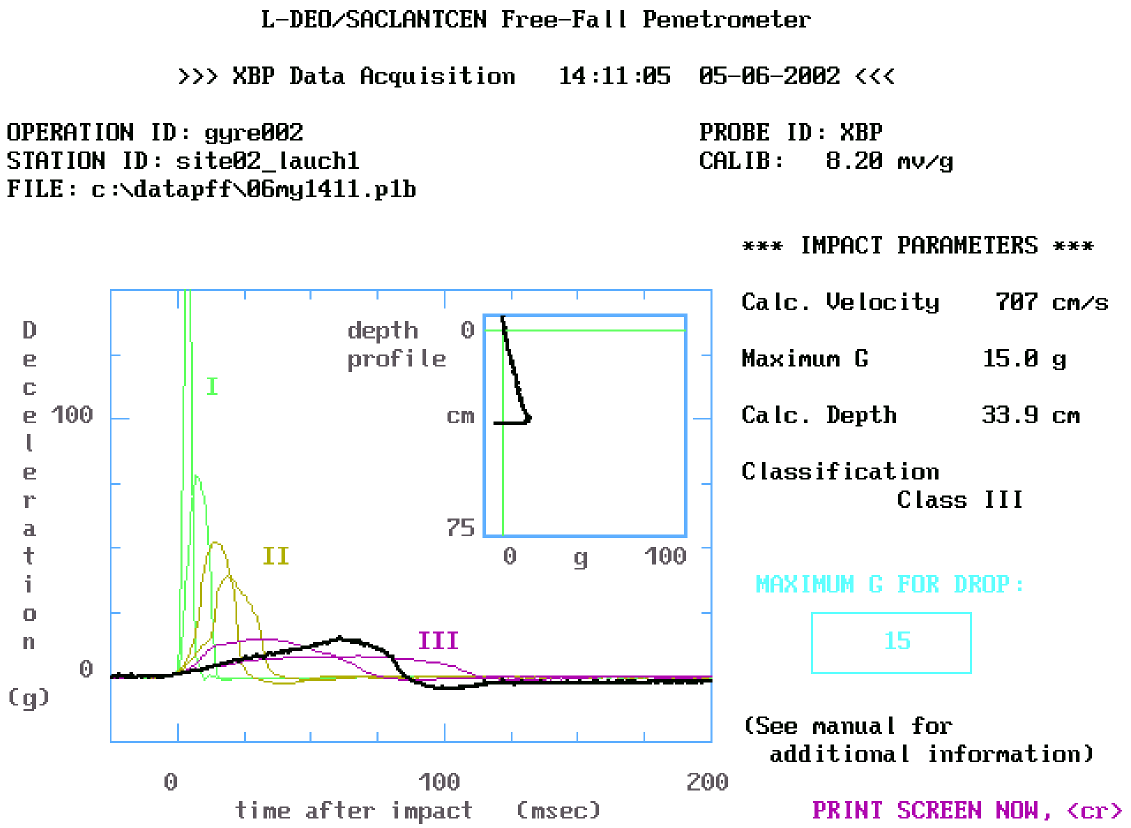

```
                L-DEO/SACLANTCEN Free-Fall Penetrometer

          >>> XBP Data Acquisition   14:11:05  05-06-2002 <<<

OPERATION ID: gyre002                           PROBE ID: XBP
STATION ID: site02_lauch1                       CALIB:   8.20 mv/g
FILE: c:\datapff\06my1411.p1b

                                                   *** IMPACT PARAMETERS ***

                                                   Calc. Velocity    707 cm/s

                                                   Maximum G        15.0 g

                                                   Calc. Depth      33.9 cm

                                                   Classification
                                                             Class III

                                                    MAXIMUM G FOR DROP:

                                                           15

                                                   (See manual for
                                                     additional information)

                                                        PRINT SCREEN NOW, <cr>
```

Figure 2.19 Typical XBP Field Record (Stoll et al., 2004)

CHAPTER III

RATE-INDEPENDENT STUDIES[*]

3.1 Plastic Limit Analysis

Plastic limit analyses were carried forward for collapse loads of horizontal cylinders embedded in open trenches. The analysis extends the study by Murff et al. (1989) to both non-uniform strength conditions and embedments exceeding one-half diameter. Following the precedent of previous studies (e.g., Davis and Booker, 1973) the analysis considers linearly varying strength profiles where the undrained shear strength c at a depth z can be characterized by the following expression:

$$c = c_m + c_1 z \tag{3.1}$$

where c_m is the strength at the ground surface (mudline) and c_1 is the rate of strength increase with depth. Such strength variation is conveniently characterized in terms of a dimensionless parameter η:

$$\eta = c_1 D / c_m \tag{3.2}$$

3.1.1 Lower Bound Analysis

MOC collapse load calculations for smooth cylinders and non-uniform strength conditions were calculated by the method illustrated in Chapter II, with the differences here being the change in θ across the shear fan and the boundary condition at the soil-

---

[*] Part of this chapter is reprinted with permission of ASCE from "Collapse loads for a cylinder embedded in trench in cohesive soil." by C. P. Aubeny, H. Shi and J. D. Murff, 2005, *International Journal of Geomechanics*, ASCE, scheduled to be published in the 2005.

cylinder interface. The angle across the singularity is $\pi\text{-}(\frac{\pi}{2}\text{-}\omega)\text{-}\frac{\pi}{4}\text{-}\frac{\pi}{4}=\omega$, where ω is defined in Figure 2.11. For the boundary point C^{IV} which is immediately under the cylinder in this case (Figure 3.1), the major principal stress σ_1 is the normal stress at the cylinder boundary. Therefore, from Figure 3.1 we have

$$x_{C^{IV}} = \sqrt{r_0^{\,2} - (y_{C^{IV}} + r_0 - h)^2} \tag{3.3}$$

$$\theta_{C^{IV}} = \tan^{-1}(\frac{y_{C^{IV}} + r_0 - h}{x_{C^{IV}}}) \tag{3.4}$$

Also, from the α-characteristic equation we have

$$y_{C^{IV}} = y_{C'''} + (x_{C^{IV}} - x_{C'''})\tan(\frac{\theta_{C^{IV}} + \theta_{C'''}}{2} - \frac{\pi}{4}) \tag{3.5}$$

By combining Eqs. 3.3, 3.4 and 3.5, we obtain the following equation:

$$y_{C^{IV}} = y_{C'''} + [\sqrt{r_0^{\,2} - (y_{C^{IV}} + r_0 - h)^2} - x_{C'''}]\tan\left\{\frac{\tan^{-1}[\dfrac{y_{C^{IV}} + r_0 - h}{\sqrt{r_0^{\,2} - (y_{C^{IV}} + r_0 - h)^2}}] + \theta_{C'''}}{2} - \frac{\pi}{4}\right\} \tag{3.6}$$

By solving this equation we can obtain $y_{C^{IV}}$, then we can calculate $x_{C^{IV}}$ and $\theta_{C^{IV}}$ by Eqs. 3.3 and 3.4, and we can calculate $\sigma_{mC^{IV}}$ by the following α-characteristic equation:

$$\sigma_{mC^{IV}} = \sigma_{mC'''} + 2(\frac{c_{C'''} + c_{C^{IV}}}{2})(\theta_{C^{IV}} - \theta_{C'''}) - c_1(x_{C^{IV}} - x_{C'''}) \tag{3.7}$$

The normal stress at the interface is then

$$\sigma = \sigma_{mC^{IV}} + c_{C^{IV}} \tag{3.8}$$

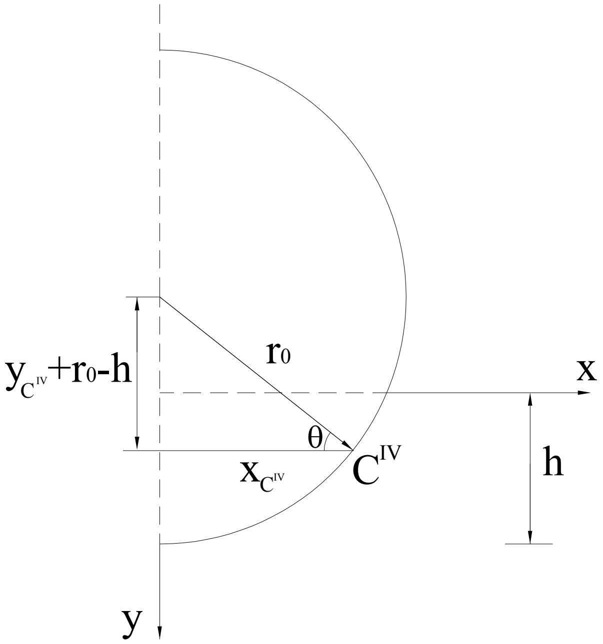

Figure 3.1 Boundary Condition for the Method of Characteristics

We can then progress to the next α characteristic until it reaches the bottom of the cylinder ($x_{C^{IV}} = 0, y_{C^{IV}} = h, \theta_{C^{IV}} = \frac{\pi}{2}$). Finally we can obtain the collapse load by integrating along the circular interface:

$$F = 2\int_{\omega}^{\frac{\pi}{2}} \sigma r_0 \sin\theta d\theta \tag{3.9}$$

A MATLAB program entitled MOC_CYLINDER has been developed for the MOC collapse load calculations for cylinders (Appendix A). Figure 3.2 illustrates the implementation of this approach for a condition of a perfectly smooth boundary (α=0) and a cylinder embedment of one-half diameter, (*h/D* = 0.5). Figure 3.2a shows the characteristic nets for the limiting cases of uniform (η=0) and triangular (η=infinity) strength profiles. With the introduction of a strength gradient, the size of the slip line field noticeably diminishes; that is, the failure zone is more localized. For example, at the free surface the lateral extent of the slip line field for η = infinity is nearly 25 percent less than that for $\eta = 0$, $0.61D$ versus $0.79D$. Slip line field boundaries for intermediate strength profiles are shown in Figure 3.2b. These again depict a continuous trend of decreasing depth and lateral extent as η increases. For the uniform strength case ($\eta = 0$), the stress field can be extended into the rigid region hence the MOC solution constitutes a valid lower bound (Murff et al., 1989). However, this task has not been undertaken in the present study for the non-homogeneous case; hence, some caution should be exercised in interpreting these solutions as the lower bounds.

Figure 3.3 illustrates normalized collapse loads computed from characteristics solutions for embedments h/D varying from 0 to 0.5. When the soil strength at depth h, c_h, is taken as the reference strength, the normalized load-embedment relationships fall into a relatively narrow band. This result may be viewed as somewhat surprising in view of rather significant effect that η had on the geometry of the slip line field. Apparently the effects of the altered slip line geometry are more or less offset by the variable strength profile so that the normalized collapse load remains essentially the same. In any event, the relative insensitivity of normalized collapse loads to variations in η shown in Figure 3.2 point to c_h as a convenient reference strength measure in the case of general values of η (Aubeny et al., 2005).

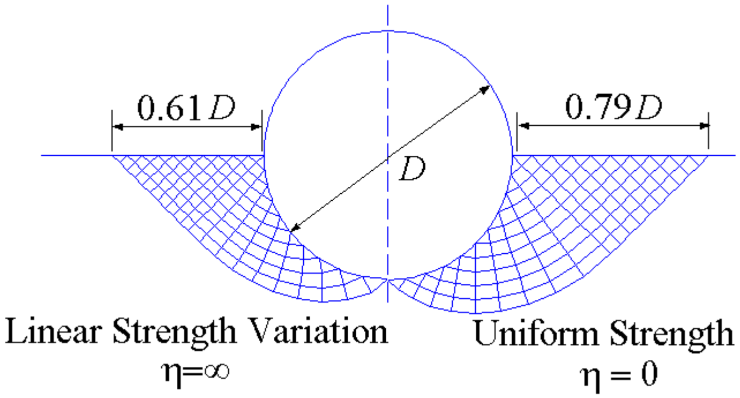

a. Characteristic Nets

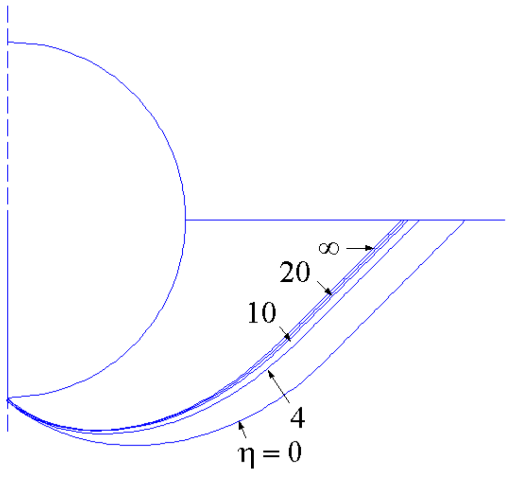

b. Slip Surfaces for Various η

Figure 3.2 Effect of Strength Gradient on Characteristics Solution (Aubeny et al., 2005)

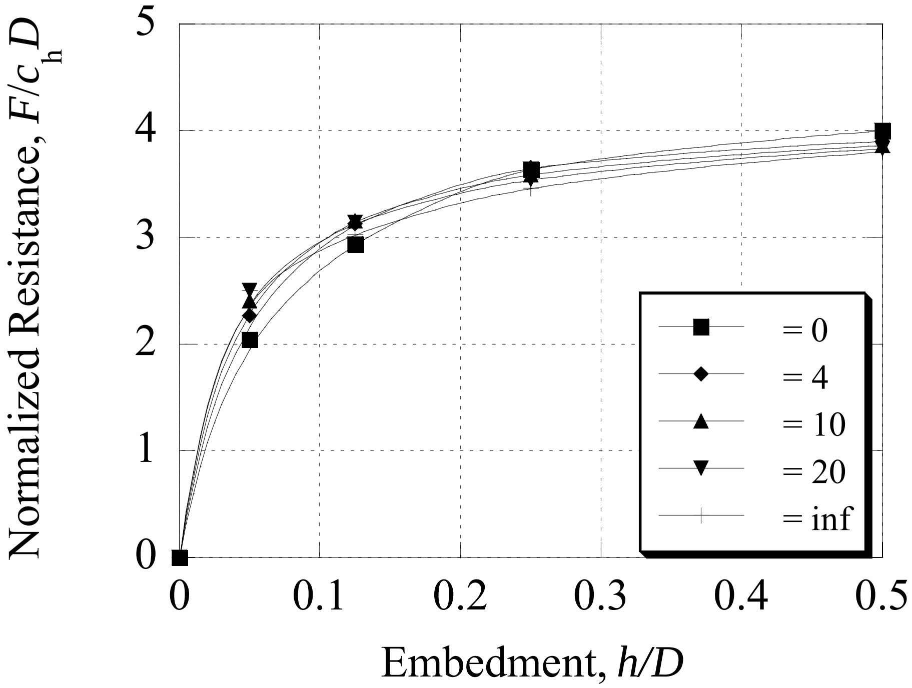

Figure 3.3 Normalized Load Capacity from MOC Solutions (Aubeny et al., 2005)

3.1.2 Upper Bound Analysis for Variable Strength Profiles

Upper bound solutions for non-uniform strength profiles are possible using either of the velocity fields shown in Figure 2.11; i.e. the consistent solution by Murff et al. in Figure 2.11a or the truncated Randolph-Houlsby in Figure 2.11b. This approach applies the velocity fields from characteristic nets in a uniform soil profile to non-uniform soil strength conditions. The mechanism is kinematically admissible so it is a valid upper bound. While the use of characteristic nets from non-uniform strength profiles (e.g., Figure 3.2) may be more appropriate in principle, such a refinement would involve numerical rather than analytical evaluation for velocities and strain rates. The computational complexity and numerical accuracy issues associated with this approach would seem to offset much of the advantage and motivation for performing the upper bound approximation; hence, this study did not adopt the more rigorous approach.

The energy dissipation rates for the deforming regions and slip planes can be evaluated in a manner similar to that of the uniform strength case, except that c is a variable changing with depth (Eq. 3.1) instead of being a constant. Therefore, the strength needs to be integrated with depth when evaluating the energy dissipation rates. For example, the dissipation rate for interface AF (Figure 2.11) is

$$\dot{D} = \int_{r_0 \cos\frac{\Delta}{2} - r_0 \sin\omega}^{r_0 \cos\frac{\Delta}{2} - r_0 \sin\omega + r_0 \sin\frac{\Delta}{2}} (c_m + c_1 z) v_0 \, dz \tag{3.10}$$

Also, for interface DE of the consistent upper bound model (Figure 2.11a), the dissipation rate is

$$\dot{D} = \int_{0}^{r_0 [\sin(\frac{\Delta}{2}) + (\frac{\pi}{2} - \frac{\Delta}{2} - \omega)\cos\psi/\sqrt{2}]} (c_m + c_1 z) v_0 \, dz \tag{3.11}$$

For interface IJ of consistent upper bound model (Figure 2.11a), the dissipation rate is

$$\dot{D} = \int_{0}^{r_0 (\frac{\pi}{2} - \frac{\Delta}{2} - \omega)\cos\psi/\sqrt{2}} (c_m + c_1 z) \Delta v_t \sqrt{2} \, dz \tag{3.12}$$

For all other slip planes and deforming regions, the dissipations can be evaluated by substitution of Eq. 3.1 into the integrals for the uniform case. Tables 3.1 and 3.2 present the integrals for the consistent upper bound model and the Randolph-Houlsby upper bound model, respectively.

Table 3.1 Dissipation Rates for the Consistent Upper Bound Model of Non-Uniform Condition (Regions Defined in Figure 2.11a)

	Region	Velocity or Strain Rate, v or $\dot{\gamma}$	Energy Dissipation Rate, $\dot{D}$
Slip Planes	AF	$v_0 / \sqrt{2}$	$\int_{r_0 \cos\frac{\Delta}{2} - r_0 \sin\omega}^{r_0 \cos\frac{\Delta}{2} - r_0 \sin\omega + r_0 \sin\frac{\Delta}{2}} (c_m + c_1 z) v_0 dz$
	ABC	$v_0 / \sqrt{2}$	$\int_{\omega}^{\pi/2-\Delta/2} (c_m + c_1 z) \frac{v_0}{\sqrt{2}} r d\theta_2$
	CD	$v_0 / \sqrt{2}$	$\int_{\pi/4}^{\pi/4+\Delta/2+\omega} (c_m + c_1 z) \frac{v_0}{\sqrt{2}} r d\theta_3$
	DE	$v_0 / \sqrt{2}$	$\int_{0}^{r_0 [\sin(\frac{\Delta}{2}) + (\frac{\pi}{2} - \frac{\Delta}{2} - \omega) \cos\psi / \sqrt{2}]} (c_m + c_1 z) v_0 dz$
	FGH	$\triangle v_t = v_0 [\cos(\Delta/2) * \sec\psi - 1/\sqrt{2}]$	$\int_{\omega}^{\pi/2-\Delta/2} (c_m + c_1 z) \triangle v_t r d\theta_2$
	HI	$\triangle v_t = v_0 [\cos(\Delta/2) * \sec\psi - 1/\sqrt{2}]$	$\int_{\pi/4}^{\pi/4+\Delta/2+\omega} (c_m + c_1 z) \triangle v_t r d\theta_3$
	IJ	$\triangle v_t = v_0 [\cos(\Delta/2) * \sec\psi - 1/\sqrt{2}]$	$\int_{0}^{r_0 (\frac{\pi}{2} - \frac{\Delta}{2} - \omega) \cos\psi / \sqrt{2}} (c_m + c_1 z) \triangle v_t \sqrt{2} dz$
	FKQ	$\triangle v_t = v_0 (\cos\theta_1 + \sin\theta_1 \tan\psi)$	$\int_{\omega}^{\pi/2-\Delta/2} (c_m + c_1 z) \sin\Delta \triangle v_t r_0 d\theta_1$
Deforming Regions	ABCHGF	$\frac{v_0}{r\sqrt{2}}$	$\int_{\omega}^{\pi/2-\Delta/2} \int_{r_1}^{r_2} \frac{(c_m + c_1 z) v_0}{r\sqrt{2}} r dr d\theta_2$
	CDIH	$\frac{v_0}{r\sqrt{2}}$	$\int_{\pi/4}^{\pi/4+\Delta/2+\omega} \int_{r_1}^{r_2} \frac{(c_m + c_1 z) v_0}{r\sqrt{2}} r dr d\theta_3$
	DEJI	0	0
	FGHQK	$\dot{\gamma} = -(\frac{v_0 \cos\theta_1}{r_0 \cos^2\psi} - \frac{v_0 \sin\theta_1}{r \cos\psi})$	$\int_{\omega}^{\pi/2-\Delta/2} \int_{\omega}^{\theta_1} (c_m + c_1 z) \dot{\gamma} r r_0 \cos\psi d\theta_2 d\theta_1$
	HIQ	$\dot{\gamma} = -(\frac{v_0 \cos\theta_1}{r_0 \cos^2\psi} - \frac{v_0 \sin\theta_1}{r \cos\psi})$	$\int_{\omega}^{\pi/2-\Delta/2} \int_{\pi/4}^{\pi/4+\Delta/2+\omega} (c_m + c_1 z) \dot{\gamma} r r_0 \cos\psi d\theta_3 d\theta_1$
	IJQ	$\frac{v_0 \cos\theta_1}{r_0 \cos^2\psi}$	$\int_{\omega}^{\frac{\pi}{2}-\frac{\Delta}{2}} \int_{0}^{y'} \frac{v_0 \cos\theta_1}{r_0 \cos^2\psi} (c_m + c_1 z) r_0 \cos\psi dx' d\theta_1$

Table 3.2 Dissipation Rates for the Randolph-Houlsby Upper Bound Model of Non-Uniform Condition (Regions Defined in Figure 2.11b)

	Region	Velocity or Strain Rate, v or $\dot{\gamma}$	Energy Dissipation Rate, $\dot{D}$
Slip Planes	AF	$v_0/\sqrt{2}$	$\int_{r_0\cos\frac{\Delta}{2}-r_0\sin\omega}^{r_0\cos\frac{\Delta}{2}-r_0\sin\omega+r_0\sin\frac{\Delta}{2}}(c_m+c_1z)v_0dz$
	ABC	$v_0/\sqrt{2}$	$\int_{\omega}^{\pi/2-\Delta/2}(c_m+c_1z)\frac{v_0}{\sqrt{2}}rd\theta_2$
	CDE	$v_0/\sqrt{2}$	$\int_{0}^{\pi/4+\Delta/2+\omega}(c_m+c_1z)\frac{v_0}{\sqrt{2}}rd\theta_3$
	FGH	$\Delta v_t=v_0[\cos(\Delta/2)*\sec\psi-1/\sqrt{2}]$	$\int_{\omega}^{\pi/2-\Delta/2}(c_m+c_1z)\Delta v_t rd\theta_2$
	HIJ	$\Delta v_t=v_0[\cos(\Delta/2)*\sec\psi-1/\sqrt{2}]$	$\int_{0}^{\pi/4+\Delta/2+\omega}(c_m+c_1z)\Delta v_t rd\theta_3$
	FKQ	$\Delta v_t=v_0(\cos\theta_1+\sin\theta_1\tan\psi)$	$\int_{\omega}^{\pi/2-\Delta/2}(c_m+c_1z)\sin\Delta\Delta v_t r_0 d\theta_1$
Deforming Regions	ABCHGF	$\frac{v_0}{r\sqrt{2}}$	$\int_{\omega}^{\pi/2-\Delta/2}\int_{r_1}^{r_2}\frac{(c_m+c_1z)v_0}{r\sqrt{2}}rdrd\theta_2$
	CDEJIH	$\frac{v_0}{r\sqrt{2}}$	$\int_{0}^{\pi/4+\Delta/2+\omega}\int_{r_1}^{r_2}\frac{(c_m+c_1z)v_0}{r\sqrt{2}}rdrd\theta_3$
	FGHQK	$\dot{\gamma}=-(\frac{v_0\cos\theta_1}{r_0\cos^2\psi}-\frac{v_0\sin\theta_1}{r\cos\psi})$	$\int_{\omega}^{\pi/2-\Delta/2}\int_{\omega}^{\theta_1}(c_m+c_1z)\dot{\gamma}rr_0\cos\psi d\theta_2 d\theta_1$
	HIJQ	$\dot{\gamma}=-(\frac{v_0\cos\theta_1}{r_0\cos^2\psi}-\frac{v_0\sin\theta_1}{r\cos\psi})$	$\int_{\omega}^{\pi/2-\Delta/2}\int_{0}^{\pi/4+\Delta/2+\omega}(c_m+c_1z)\dot{\gamma}rr_0\cos\psi d\theta_3 d\theta_1$

The vertical coordinate *z* to characterize the strength profile must be transformed so that it is expressed in terms of the same variables as the energy dissipation relationships. Table 3.3 and 3.4 contain the appropriate expressions. Substitution of these expressions into the integrals in Table 3.1 and 3.2 will result in modified integrals, some of which must be evaluated numerically. MATLAB programs entitled RH_CYLINDER and CU_CYLINDER have been developed for the upper bound models above (Appendix B and C).

Table 3.3 Vertical Coordinates for Consistent Characteristic Net (Regions Defined in Figure 2.11a)

	Region	Vertical Coordinate, z
Slip Planes	ABC	$z = r_0 \sin\theta_2 - r_0 \sin\omega + (r - r_0 \sin\psi)\cos(\theta_2 - \psi)$
	CD	$z = r\sin\theta_3$
	FGH	$z = r_0 \sin\theta_2 - r_0 \sin\omega + (r - r_0 \sin\psi)\cos(\theta_2 - \psi)$
	HI	$z = r\sin\theta_3$
	FKQ	$z = r_0 \sin\theta_1 - r_0 \sin\omega$
Deforming Regions	ABCHGF	$z = r_0 \sin\theta_2 - r_0 \sin\omega + (r - r_0 \sin\psi)\cos(\theta_2 - \psi)$
	CDIH	$z = r\sin\theta_3$
	FGHQK	$z = r_0 \sin\theta_2 - r_0 \sin\omega + (r - r_0 \sin\psi)\cos(\theta_2 - \psi)$
	HIQ	$z = r\sin\theta_3$
	IJQ	$z = \frac{\sqrt{2}}{2}(y' - x')$

Table 3.4 Vertical Coordinates for Randolph-Houlsby Characteristic Net (Regions Defined in Figure 2.11b)

	Region	Vertical Coordinate, z
Slip Planes	ABC	$z = r_0 \sin\theta_2 - r_0 \sin\omega + (r - r_0 \sin\psi)\cos(\theta_2 - \psi)$
	CDE	$z = r\sin\theta_3$
	FGH	$z = r_0 \sin\theta_2 - r_0 \sin\omega + (r - r_0 \sin\psi)\cos(\theta_2 - \psi)$
	HIJ	$z = r\sin\theta_3$
	FKQ	$z = r_0 \sin\theta_1 - r_0 \sin\omega$
Deforming Regions	ABCHGF	$z = r_0 \sin\theta_2 - r_0 \sin\omega + (r - r_0 \sin\psi)\cos(\theta_2 - \psi)$
	CDEJIH	$z = r\sin\theta_3$
	FGHQK	$z = r_0 \sin\theta_2 - r_0 \sin\omega + (r - r_0 \sin\psi)\cos(\theta_2 - \psi)$
	HIJQ	$z = r\sin\theta_3$

3.1.3 Upper Bound Analysis for Penetration Exceeding One Radius

The truncated Randolph-Houlsby solution is extended to penetrations exceeding one radius $h/r_0 > 1$, simply by extending the circular fan QEOP upward as shown in Figure 3.4. The mechanism is kinematically admissible so it is a rigorous upper bound. To evaluate the total energy dissipation in this extended region integration proceeds along the characteristics until a characteristic intersects either the horizontal free surface or the vertical surface of the open trench.

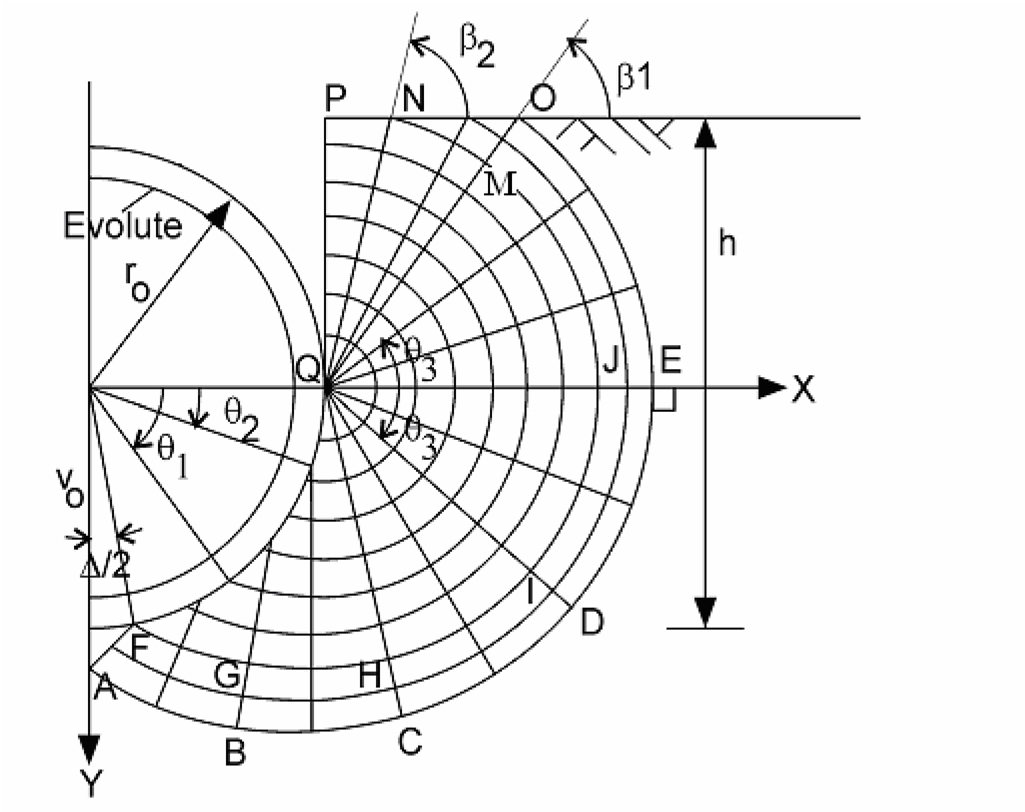

Figure 3.4 Extension of Randolph-Houlsby Solution (Aubeny et al., 2005)

Interface EO is a circular arc centered at Q (extension of CDE), the tangential velocity along EO is $v_t = v_0/\sqrt{2}$, thus

$$\dot{D} = \int_0^{\beta_1} cv_0/\sqrt{2}rd\theta_3 \tag{3.13}$$

where $r = r_0[\sqrt{2}\sin(\frac{\Delta}{2}) + (\frac{\pi}{2} - \frac{\Delta}{2})\cos\psi]$, and $\beta_1 = \sin^{-1}((h-r_0)/r)$ when $h < r_0 + r$ and $\beta_1 = \pi/2$ when $h \geq r_0 + r$.

Interface JMN is a circular arc extended from HIJ. A tangential velocity discontinuity same as that of HIJ exists across JMN, i.e., $\triangle v_t = v_0[\cos(\Delta/2)\sec\psi - 1/\sqrt{2}]$. Thus

$$\dot{D} = \int_0^{\beta_2} c\triangle v_t r d\theta_3 \tag{3.14}$$

where $r = r_0(\frac{\pi}{2} - \frac{\Delta}{2} - \omega)\cos\psi$, and $\beta_2 = \sin^{-1}((h-r_0)/r)$ when $h < r_0 + r$ and $\beta_2 = \pi/2$ when $h \geq r_0 + r$.

Area EOMJ is a deforming region extended from CDEJIH. The tangential velocity and the shear strain rate is in the same form as within region CDEJIH, i.e. $\dot{\gamma} = \frac{v_0}{r\sqrt{2}}$. Thus

$$\dot{D} = \int_0^{\beta_1}\int_{r_1}^{r_2} \frac{cv_0}{r\sqrt{2}} r dr d\theta_3 \tag{3.15}$$

where $r_1 = r_0(\frac{\pi}{2} - \frac{\Delta}{2})\cos\psi$

$r_2 = r_0[\sqrt{2}\sin(\frac{\Delta}{2}) + (\frac{\pi}{2} - \frac{\Delta}{2})\cos\psi]$

Region JNQ is a shear fan extended from HIJQ. The tangential velocity and shear strain rate is in the same form as within HIJQ, i.e., $\dot{\gamma} = -(\frac{v_0 \cos\theta_1}{r_0 \cos^2\psi} - \frac{v_0 \sin\theta_1}{r \cos\psi})$, and the radius of curvature $r = r_0\theta_1 \cos\psi$. Thus

$$\dot{D} = \int_0^{\pi/2-\Delta/2} \int_0^{\beta_2} c\dot{\gamma} r r_0 \cos\psi d\theta_3 d\theta_1 \tag{3.16}$$

For region OMN, The tangential velocity and the shear strain rate is in the same form as within region EOMJ, i.e., $\dot{\gamma} = \frac{v_0}{r\sqrt{2}}$. Thus

$$\dot{D} = \int_{\beta_1}^{\beta_2} \int_{r_1}^{r_2} \frac{c v_0}{r\sqrt{2}} r dr d\theta_3 \tag{3.17}$$

where the radial integration limits $r_1 = r_0(\frac{\pi}{2} - \frac{\Delta}{2})\cos\psi$; $r_2 = \frac{h - r_0}{\sin\theta_3}$.

For region NQP, the tangential velocity and shear strain rate is in the same form as within HIJQ, i.e., $\dot{\gamma} = -(\frac{v_0 \cos\theta_1}{r_0 \cos^2\psi} - \frac{v_0 \sin\theta_1}{r \cos\psi}), \theta_1 = r / r_0 \cos\psi$. Thus

$$\dot{D} = \int_{\beta_2}^{\pi/2} \int_0^{\frac{h-r_0}{\sin\theta_3}} c\dot{\gamma} r dr d\theta_3 \tag{3.18}$$

For non-uniform conditions and penetrations exceeding one radius, the dissipation rates for the extended slip planes and deforming regions were evaluated using the same velocity field as the uniform case. The integrals for the dissipation relationships are listed in Table 3.5, and the corresponding expressions of the vertical coordinates are listed in Table 3.6. Appendix B contains the MATLAB program for the extended Randolph-Houlsby upper bound model.

Table 3.5 Dissipation Rates for the Extended Randolph-Houlsby Mechanism of Non-Uniform Condition (Regions Defined in Figure 3.5)

	Region	Velocity or Strain Rate, v or $\dot{\gamma}$	Energy Dissipation Rate, $\dot{D}$
Slip Planes	EO	$v_0 / \sqrt{2}$	$\int_0^{\beta_1} (c_m + c_1 z) v_0 / \sqrt{2} r d\theta_3$
	JMN	$\Delta v_t = v_0 [\cos(\Delta / 2) * \sec\psi - 1/\sqrt{2}]$	$\int_0^{\beta_2} (c_m + c_1 z) \Delta v_t r d\theta_3$
Deforming Regions	EOMJ	$\frac{v_0}{r\sqrt{2}}$	$\int_0^{\beta_1} \int_{r_1}^{r_2} \frac{(c_m + c_1 z) v_0}{r\sqrt{2}} r dr d\theta_3$
	JNQ	$\dot{\gamma} = -(\frac{v_0 \cos\theta_1}{r_0 \cos^2\psi} - \frac{v_0 \sin\theta_1}{r\cos\psi})$	$\int_0^{\pi/2-\Delta/2} \int_0^{\beta_2} (c_m + c_1 z) \dot{\gamma} r r_0 \cos\psi d\theta_3 d\theta_1$
	OMN	$\frac{v_0}{r\sqrt{2}}$	$\int_{\beta_1}^{\beta_2} \int_{r_1}^{r_2} \frac{(c_m + c_1 z) v_0}{r\sqrt{2}} r dr d\theta_3$
	NQP	$\dot{\gamma} = -(\frac{v_0 \cos\theta_1}{r_0 \cos^2\psi} - \frac{v_0 \sin\theta_1}{r\cos\psi})$	$\int_{\beta_2}^{\pi/2} \int_0^{\frac{h-r_0}{\sin\theta_3}} (c_m + c_1 z) \dot{\gamma} r dr d\theta_3$

Table 3.6 Vertical Coordinates for the Extended Randolph-Houlsby Mechanism (Regions Defined in Figure 3.5)

	Region	Vertical coordinate, *z*
Slip Planes	ABC	$z = r_0 \sin\theta_2 + (r - r_0 \sin\psi)\cos(\theta_2 - \psi) + h - r_0$
	CDE	$z = r\sin\theta_3 + h - r_0$
	FGH	$z = r_0 \sin\theta_2 + (r - r_0 \sin\psi)\cos(\theta_2 - \psi) + h - r_0$
	HIJ	$z = r\sin\theta_3 + h - r_0$
	FKQ	$z = r_0 \sin\theta_1 + h - r_0$
	EO	$z = h - r_0 - r\sin\theta_3$
	JMN	$z = h - r_0 - r\sin\theta_3$
Deforming Regions	ABCHGF	$z = r_0 \sin\theta_2 + (r - r_0 \sin\psi)\cos(\theta_2 - \psi) + h - r_0$
	CDEJIH	$z = r\sin\theta_3 + h - r_0$
	FGHQK	$z = r_0 \sin\theta_2 + (r - r_0 \sin\psi)\cos(\theta_2 - \psi) + h - r_0$
	HIJQ	$z = r\sin\theta_3 + h - r_0$
	EOMJ	$z = h - r_0 - r\sin\theta_3$
	JNQ	$z = h - r_0 - r\sin\theta_3$
	OMN	$z = h - r_0 - r\sin\theta_3$
	NQP	$z = h - r_0 - r\sin\theta_3$

3.2 Finite Element Analysis

The finite element analysis was conducted for both the cylinder studies and the XBP studies using the commercial code ABAQUS 6.4 (2003). To establish the accuracy of the finite element model, an analysis was first conducted for the case of a fully embedded cylinder (full flow-around condition) and the collapse load was compared to the analytical solution of Randolph and Houlsby (1984). After that, finite element simulations at a series of embedment depths were conducted for both the cylinders and the XBPs. The case of full flow-around cylinder is considered initially as an example to illustrate the method of the finite element analysis.

3.2.1 Geometry Model

Following the previous study by Yao (2003), the analysis used the geometry model illustrated in Figure 3.5. Due to symmetry only the right half was modeled in the finite element study. The far-field boundary is located 4.5D from the cylinder boundary in both horizontal and vertical directions.

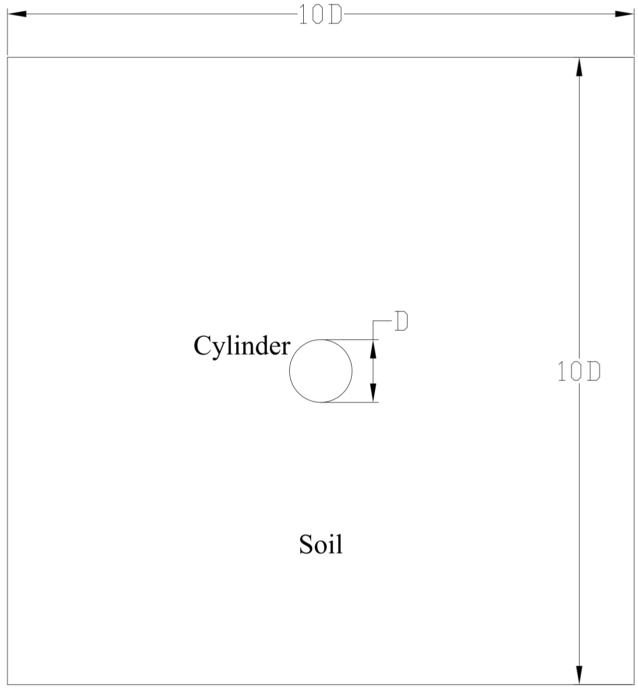

Figure 3.5 Geometry Model for Full Flow-around Cylinder

3.2.2 Material Model

The plastic limit methods discussed above employed a rigid plastic material model, and the material was assumed to obey the von Mises yield criterion and an associated flow rule. Similarly, the finite element model employed an elastic-plastic model, i.e., the soil is linearly elastic for stress states beneath the yield surface and perfectly plastic at yield with a von Mises yield criterion and an associated flow rule. The analysis introduced elastic behavior to permit implementation of the finite element formulation, however, as demonstrated by Chen (1975), the computed collapse loads should be independent of elastic behavior.

For undrained analysis the soil is incompressible, that is, the poisson ratio $\upsilon = 0.5$. To avoid an infinite bulk modulus, a value of 0.499 was used instead of 0.5. ABAQUS defines material strength in terms of the yield stress in uniaxial loading; i.e.; a stress state with $\sigma_1 = \sigma_y, \sigma_2 = \sigma_3 = 0$, where σ_y is the yield stress. According to Eqs. 2.2a and 2.2b, σ_y is related to the strength in simple shear by the relation:

$$\sigma_y = \sqrt{3}k \tag{3.19}$$

3.2.3 Boundary Conditions

Two kinds of soil-cylinder boundary condition were considered in this study: no slippage and full slippage (Figure 3.7), corresponding to the rough and smooth cases in the study by Randolph and Houlsby (1984). For the no slippage case, the displacement of a point on the cylinder δ is identical to the displacement of the soil u_s at the boundary (Figure 3.6a), that is, no relative displacement occurs between the soil and the cylinder along the interface. This boundary condition can be formulated as

$$u_x = 0 \tag{3.20a}$$

$$u_y = \delta \tag{3.20b}$$

For the full slippage case, the displacements in the normal direction of the boundary of a point on the cylinder at the interface and the adjacent soil must be equal, whereas the motion of the soil in the tangential direction of the boundary is unconstrained (Figure 3.6b). This boundary condition can be formulated as

$$u_x \cos\theta + u_y \sin\theta = \delta \sin\theta \tag{3.21}$$

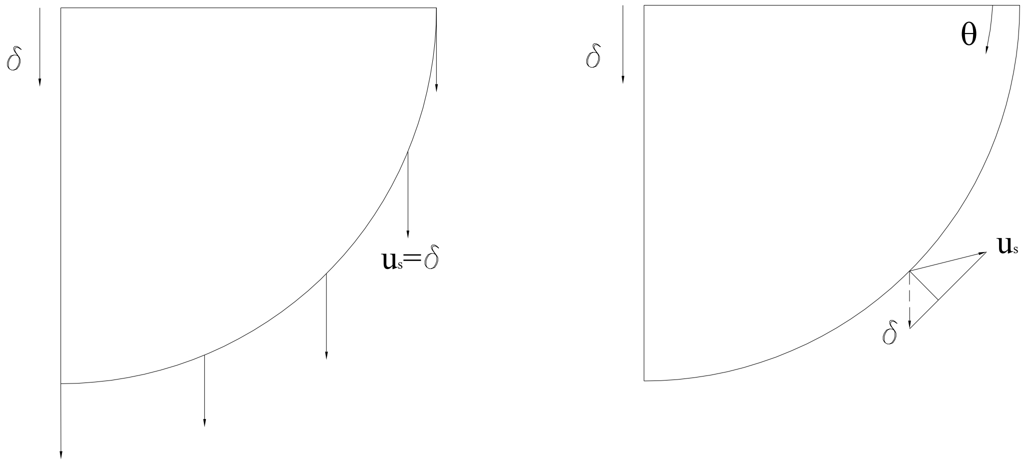

a. No Slippage **b. Full Slippage**

Figure 3.6 Boundary Conditions at the Soil-Cylinder Interface

In this case, the soil displacements at the boundary can not be directly prescribed like the no slippage case, however, it can be imposed using the linear constraint equation option of ABAQUS (2003).

Figure 3.7 illustrates the boundary conditions for a fully embedded rough cylinder. The cylinder was modeled as a cavity translating downwards, and the soil displacements were prescribed by Eq. 3.20a and 3.20b. The mudline was an unconstrained free surface. The centerline was constrained horizontally due to symmetry (roller condition). The right far-field boundary was also constrained horizontally (roller condition), and the bottom boundary was constrained in all directions (fixed condition).

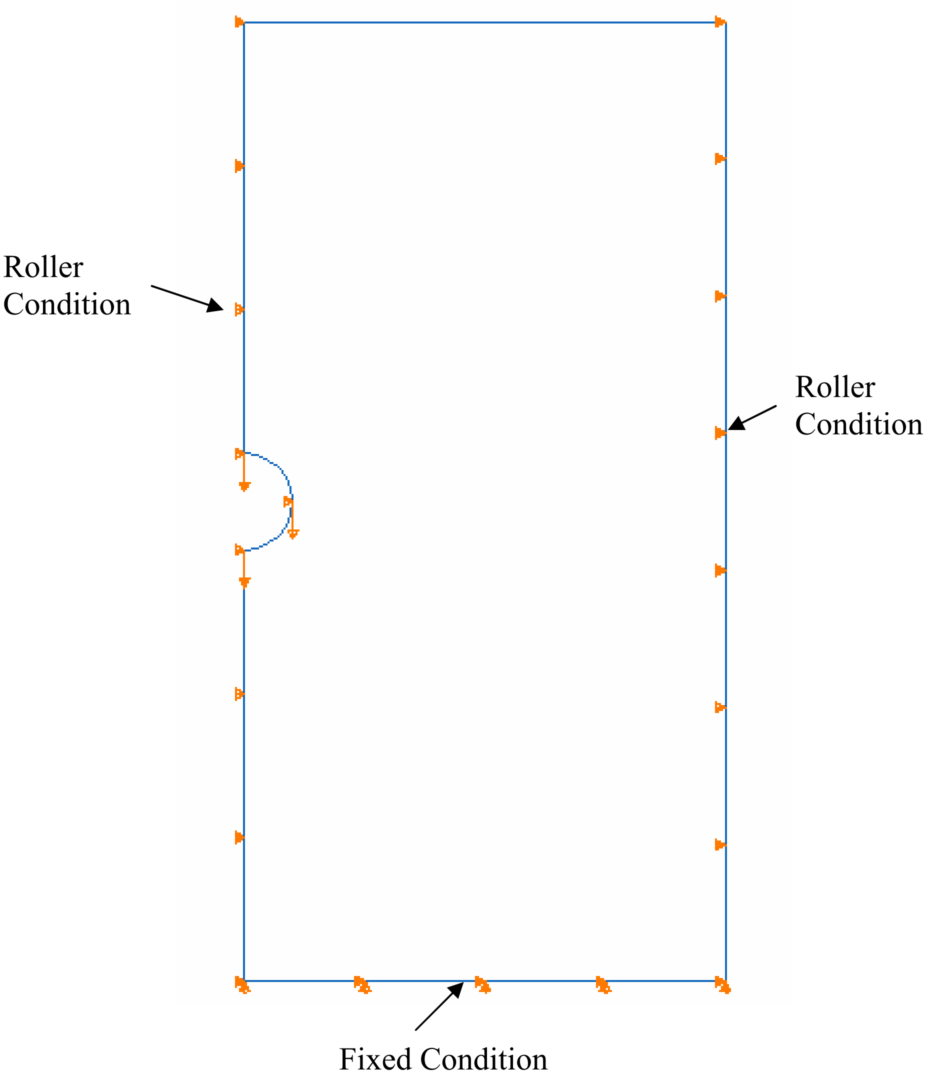

Figure 3.7 Boundary Conditions of a Fully Embedded Cylinder (No Slippage)

3.2.4 Mesh Construction

Figure 3.8 illustrates the mesh used for the full flow-around cylinder case, in which the element dimensions (*s*) are on the order of 0.005*D* near the cylinder boundary. For efficiency a non-uniform mesh is more reasonable, i.e., a finer mesh in the zone of interest near the cylinder boundary, and a coarser mesh near the far-field boundary. The computed normalized collapse load for conditions of full slippage was $F/cD = 9.23$, exceeding the Randolph-Houlsby lower bound estimate, $F/cD = 9.14$, by 1%. For conditions of no slippage the computed collapse load, $F/cD = 12.03$, similarly exceeded the Randolph-Houlsby exact solution by 1%. The mesh was established by a trial and error method. Finite element meshes at different levels of refinement were used and the results were compared to the analytical solutions by Randolph and Houlsby (1984), as illustrated in Figure 3.9.

Following the previous study by Yao (2003), the analysis used linear, 4-node quadrilateral, plane strain elements.

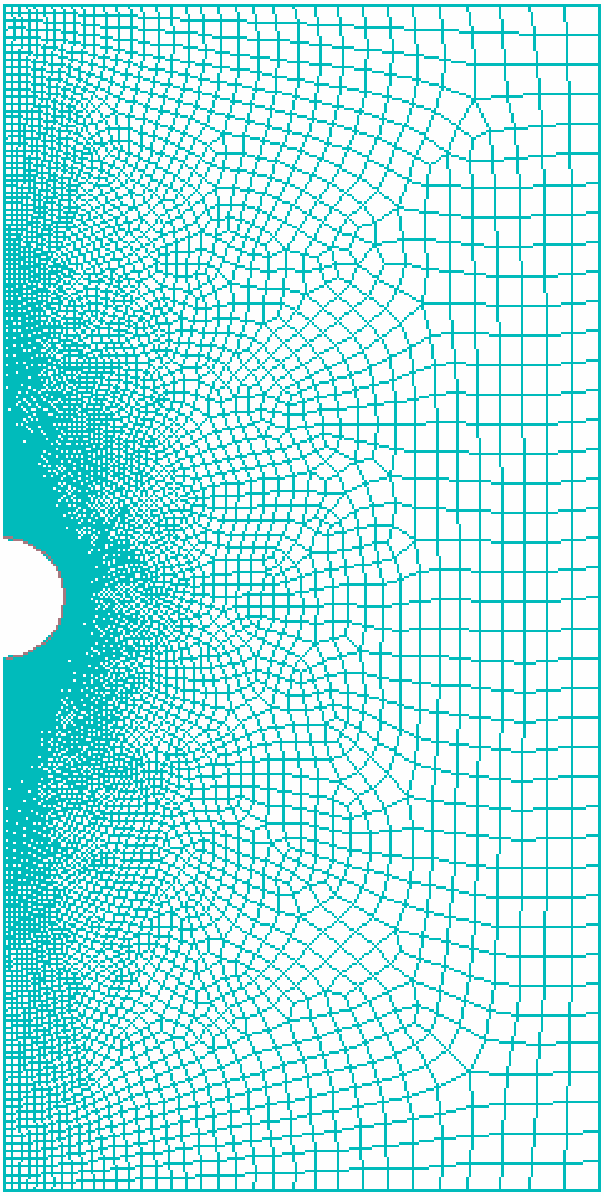

Figure 3.8 Finite Element Mesh for Full Flow-around Cylinder

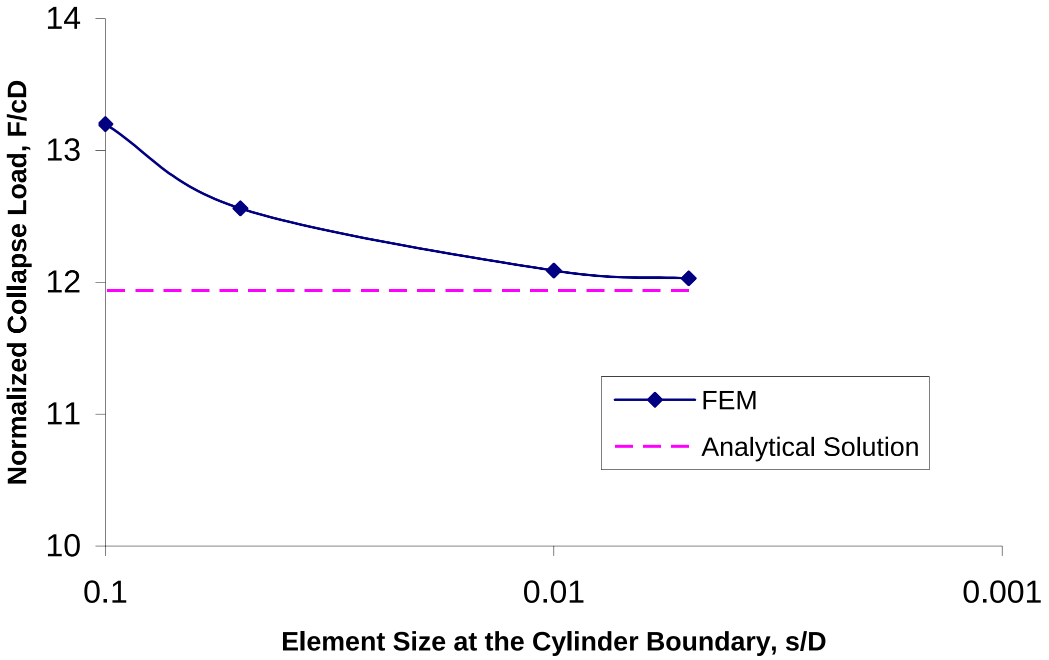

Figure 3.9 Effect of Mesh Refinement on the Collapse Loads of a Full Flow-around Cylinder

3.2.5 Loading Step

The loading step in this analysis was achieved by imposing a vertical downward displacement incrementally on the cylinder until the soil reaches failure state. The total reaction force is obtained by summing up the vertical reaction forces of the soil at the soil-cylinder interface. As the displacement increases, the total reaction force will tend toward a limit, which is the collapse load of the soil. Figure 3.10 illustrates the relationship between the normalized total reaction force and the vertical displacement of the cylinder for a fully embedded rough cylinder.

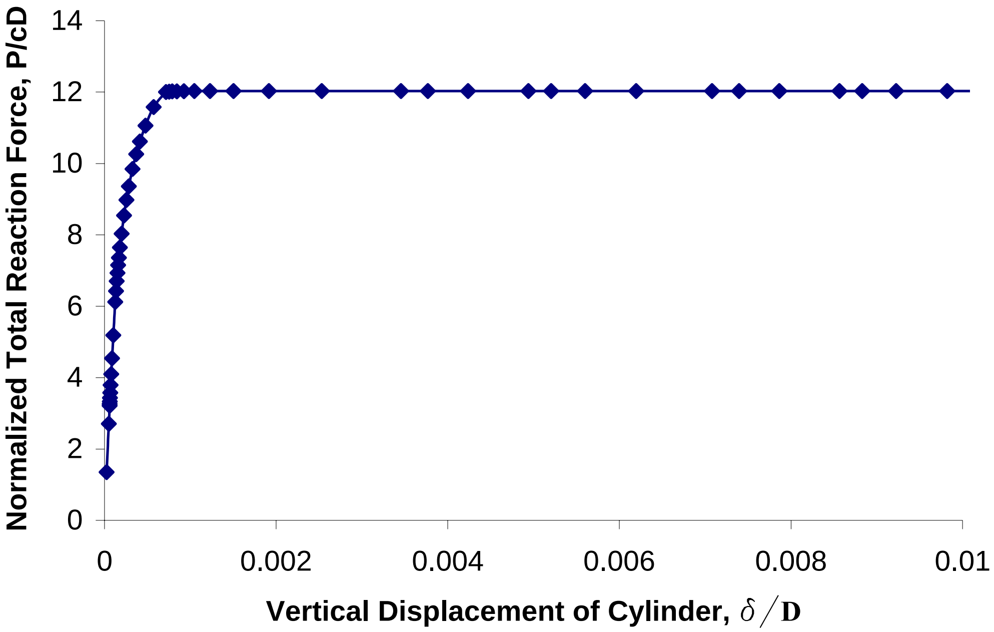

Figure 3.10 Loading Step for a Fully Embedded Rough Cylinder

3.2.6 Cylinder Penetration Studies

Cylinder penetration studies were conducted at a series of embedment depths with a similar finite element model and level of mesh refinement as described above. Figures 3.11 and 3.12 illustrate an example of the models used for a cylinder embedded at a depth of $h/D \leq 0.5$ and a cylinder embedded at a depth of $h/D > 0.5$, respectively. The analysis was performed for both no slippage and full slippage boundary conditions. Also, two limiting strength profiles were considered: $\eta = 0$ (uniform) and $\eta = \infty$ (triangular). Based on experimental data from the penetration tests, the FEM studies consider embedments *h/D* ranging from 0 to 4. A typical ABAQUS input file for finite element computation of a collapse load for a horizontal cylinder is shown in Appendix F.

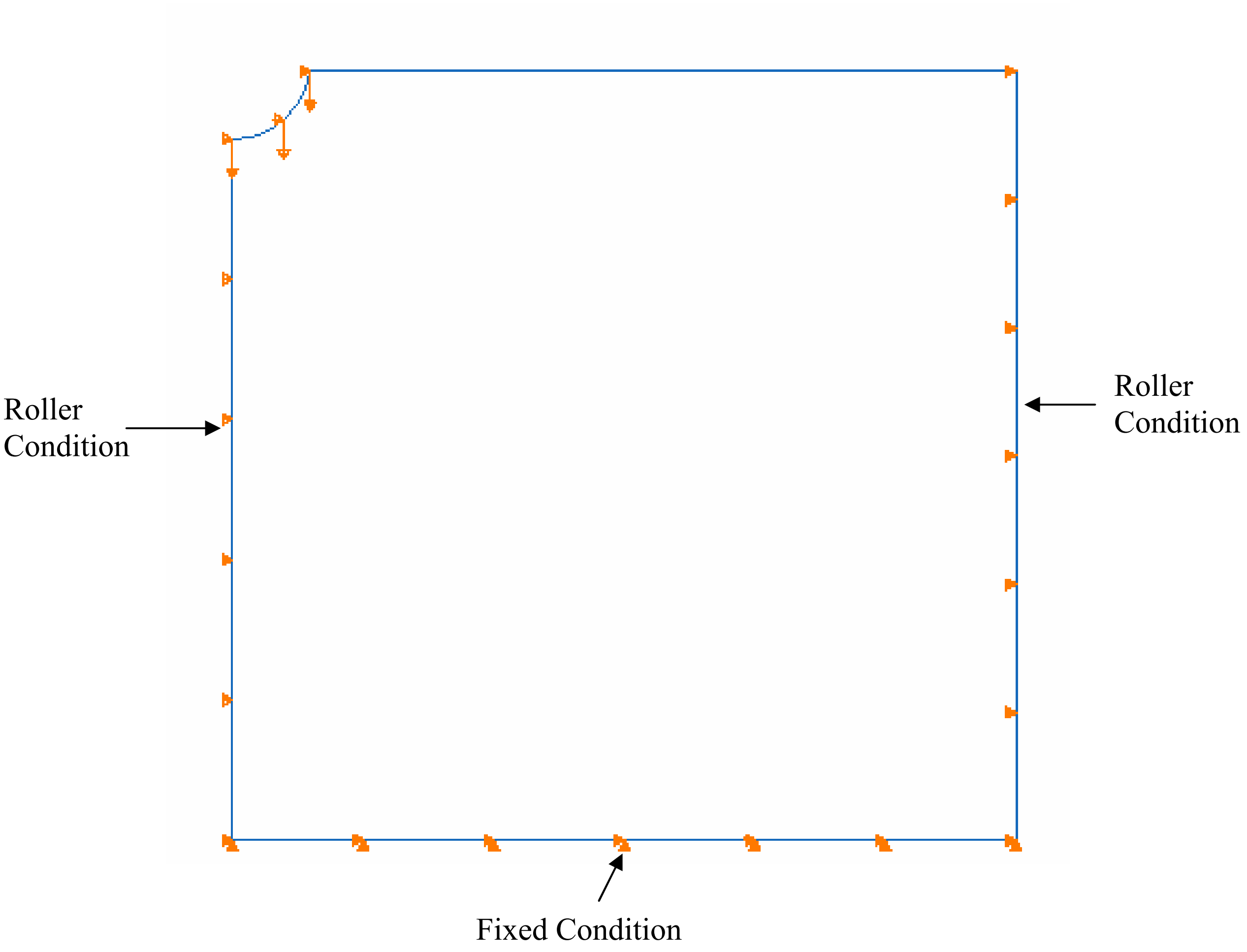

Figure 3.11 Finite Element Model for Cylinder Penetration Studies, *h/D*≤0.5

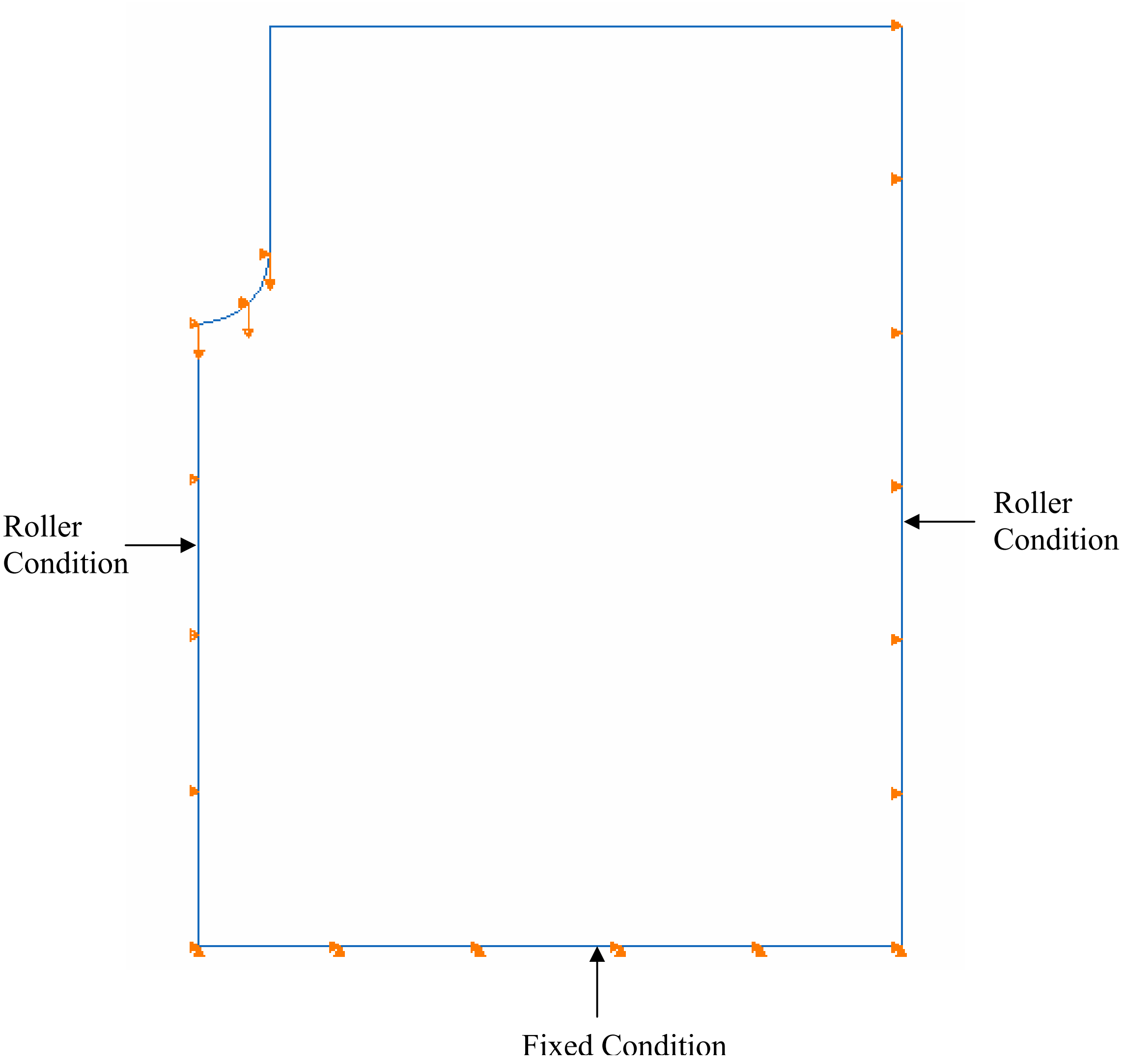

Figure 3.12 Finite Element Model for Cylinder Penetration Studies, *h/D*>0.5

3.2.7 XBP Penetration Studies

The finite element studies on XBP penetration were conducted within a similar framework of the cylinder penetration studies, with the major difference being that the XBP is axisymmetric instead of a plane strain condition. The finite element analysis for the XBP studies was performed with a finite element model and level of mesh refinement similar to the cylinder studies. The study employed linear, 4-node quadrilateral, axisymmetric elements. The analysis considered a uniform strength profile and a rough boundary between the soil and the penetrometer. Figure 3.13 illustrates an example of the finite element models. Based on the depth of penetration of the XBP tests, a range of embedments *h/d* from 0 to 7 was considered.

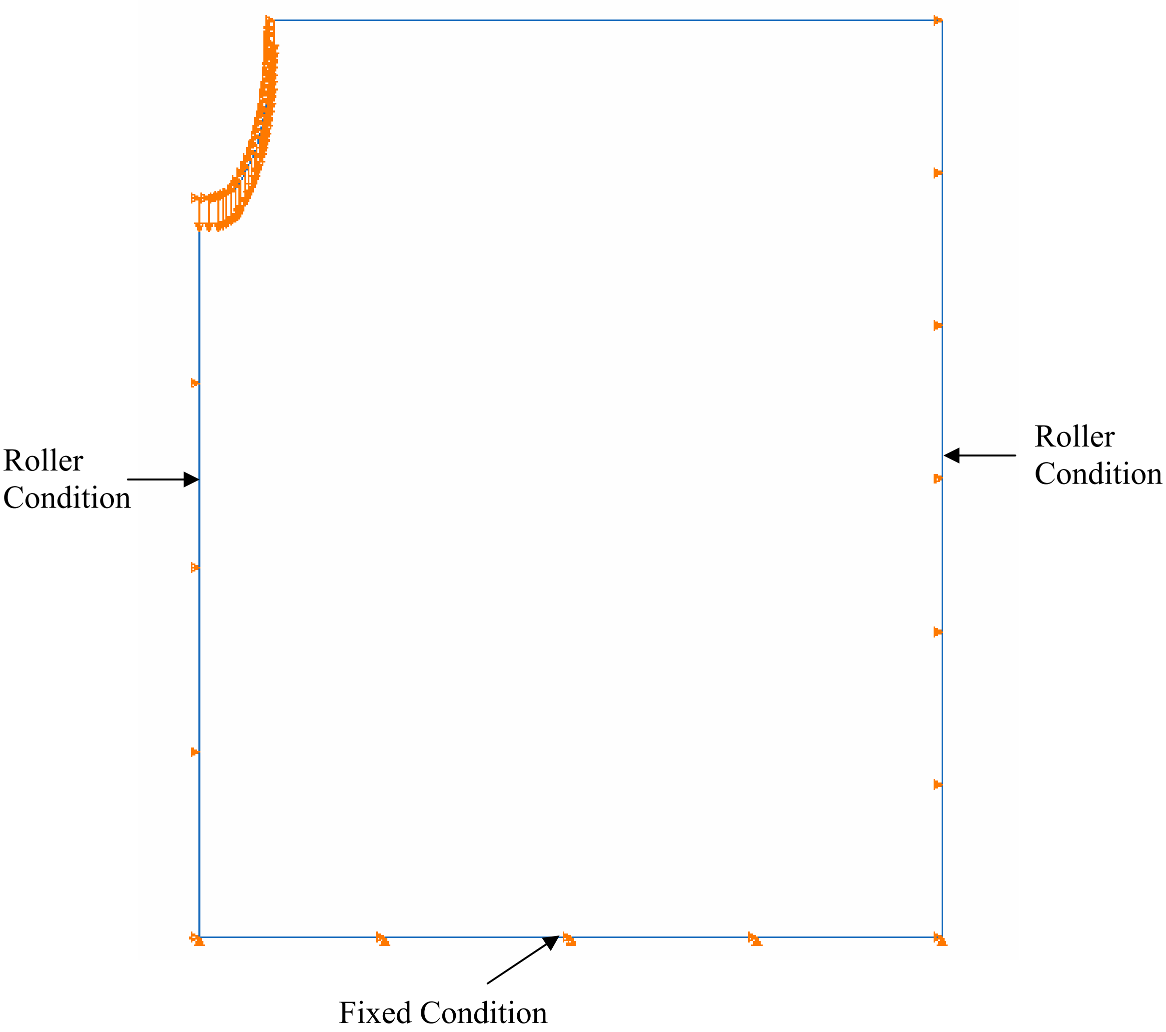

Figure 3.13 Finite Element Model for the XBP Penetration Studies

Special cases of a thin hard layer embedded in a relative soft layer were also considered as a preliminary study of the inter-bed effect, which will be described in Chapter V. Aside from the embedment depth *h*, other influencing factors for the collapse load include the thickness of the inter-bed, *t*; the distance from the tip of the penetrometer to the centerline of the inter-bed, z_s; and the ratio of the strength of the inter-bed to that of the soft soil, c_i / c_s (Figure 3.14).

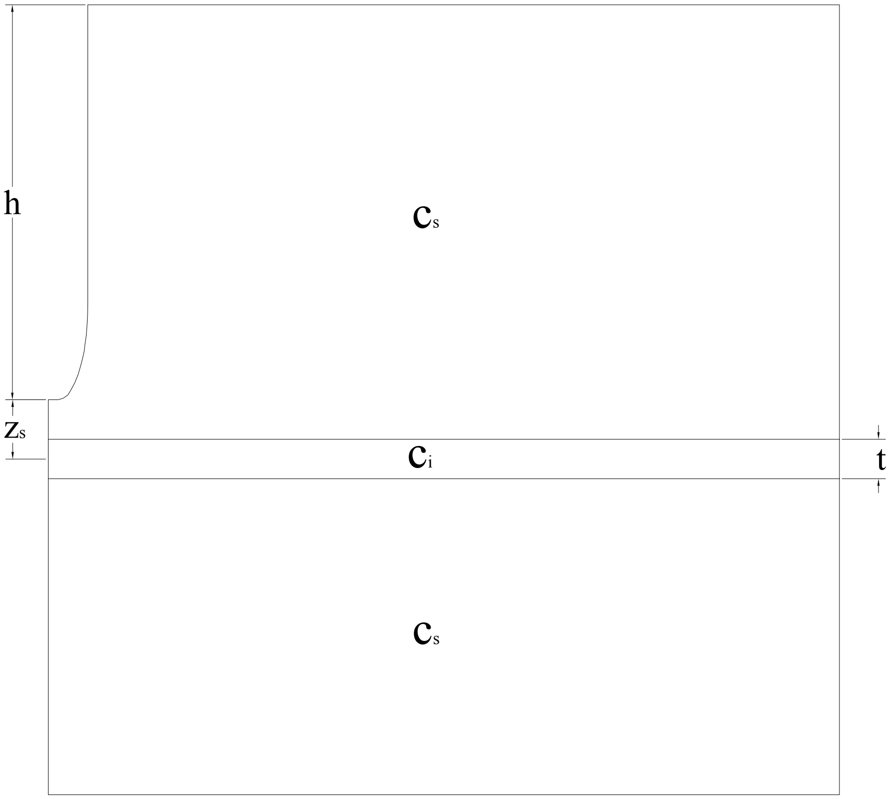

Figure 3.14 Influencing Factors of the Collapse Load for the Hard Layer Study

3.3 Comparison of Solutions

Figures 3.15 and 3.16 compare finite element estimates of collapse loads of a cylinder at shallow embedments ($h/D \leq 0.5$) for various conditions of cylinder boundary roughness and soil strength profiles to the plasticity solutions.

For a smooth cylinder with uniform soil strength conditions (Figure 3.15a), the lower bound MOC solution is in close agreement with the finite element solution for embedments h/D up to about 0.3. Beyond this depth the two solutions diverge somewhat until at h/D=0.5 the finite element solution exceeds the lower bound estimate by about 10%. The consistent upper bound solution agrees with the finite element solution only for very shallow embedments, h/D<0.1. At greater embedments, the consistent upper bound solution increasingly diverges from the finite element solution, until at h/D=0.5 it exceeds the finite element solution by about 25%. For embedments greater than h/D>0.3, the upperbound derived from truncated Randolph-Houlsby velocity field is actually in better agreement with the finite element solution than the consistent upperbound solution.

Figure 3.15b presents the case of a rough boundary and a uniform strength profile. The consistent upperbound solution is in virtual perfect agreement with the finite element solution for embedment depths up to h/D<0.3, diverging from the finite element solution at greater embedments by up to 5%. The Randolph-Houlsby solution exceeds the finite element solution by over 10% at shallow embedments, h/D<0.3. At greater embedments the differences decline, until at one radius embedment, h/D=0.5, the two solutions are in agreement.

Considering a linearly varying strength profile, $\eta=\infty$, and a smooth cylinder, the finite element solutions in Figure 3.16a closely match the MOC solutions to embedments $h/D<0.4$; beyond this depth the finite element solutions exceed the MOC estimates by up to 5%. Upper bound collapse load estimates derived from the truncated Randolph-Houlsby and consistent upper bound velocity fields are nearly identical, and both significantly exceed finite element estimates (by up to 40%) at shallow embedments, $h/D<0.3$. Such discrepancy is not unexpected in view of the earlier comment that these velocity fields strictly correspond to conditions of uniform strength. Nevertheless, at greater embedment, the upper bound solutions come into closer agreement with the finite element solutions, with the upper bound collapse load estimate at $h/D=0.5$ exceeding the finite element value by only 5%.

For the case shown in Figure 3.16b of a rough cylinder boundary with a linearly varying strength profile, $\eta=\infty$, little difference exists between the consistent and truncated Randolph-Houlsby upper bound solutions, with the consistent upper bound solution being in slightly closer agreement with the finite element solutions. The differences between the upper bound and finite element solutions are greatest at intermediate penetrations.

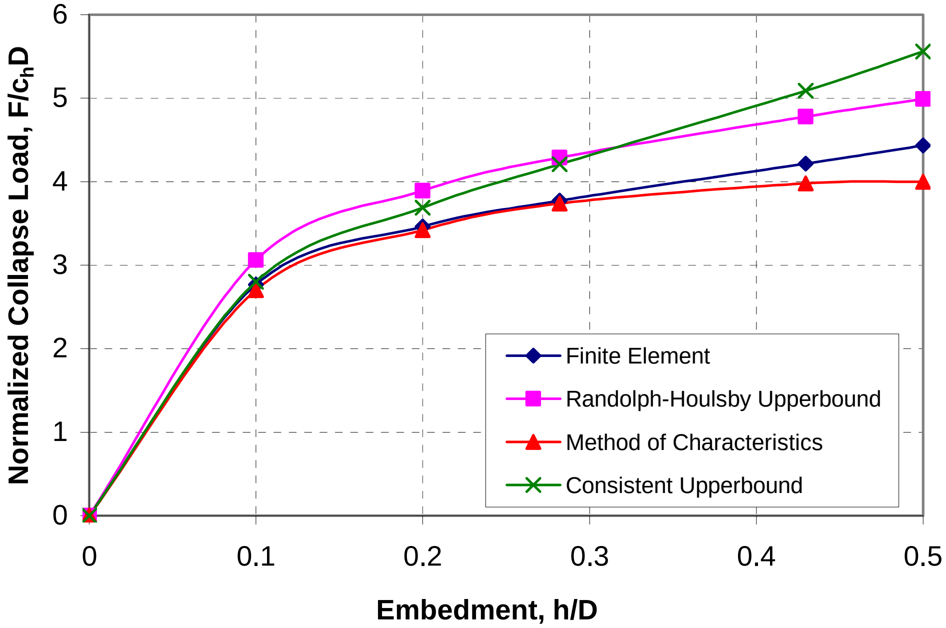

a. Smooth

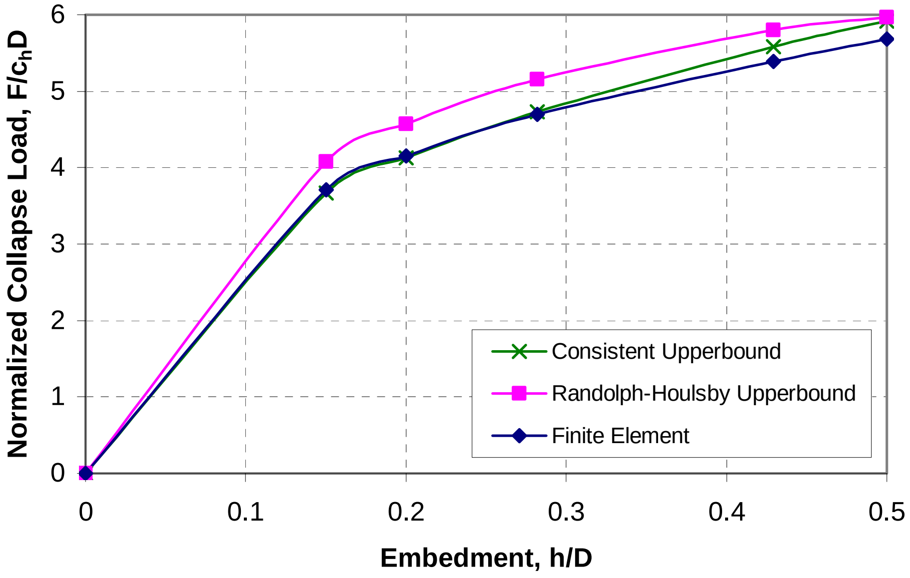

b. Rough

Figure 3.15 Collapse Loads for Cylinders of *h/D*≤0.5, η=0

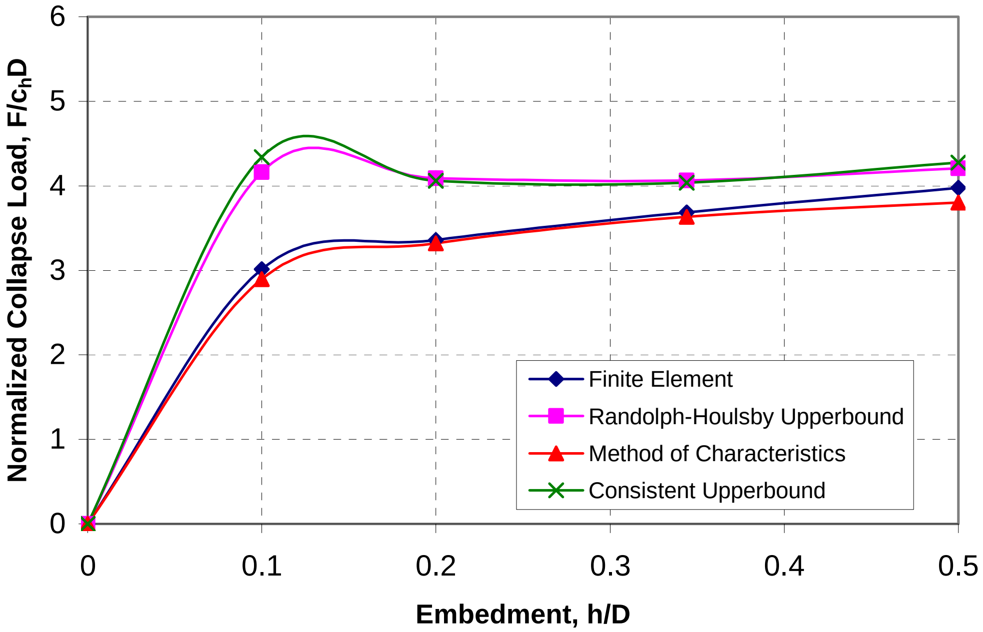

a. Smooth

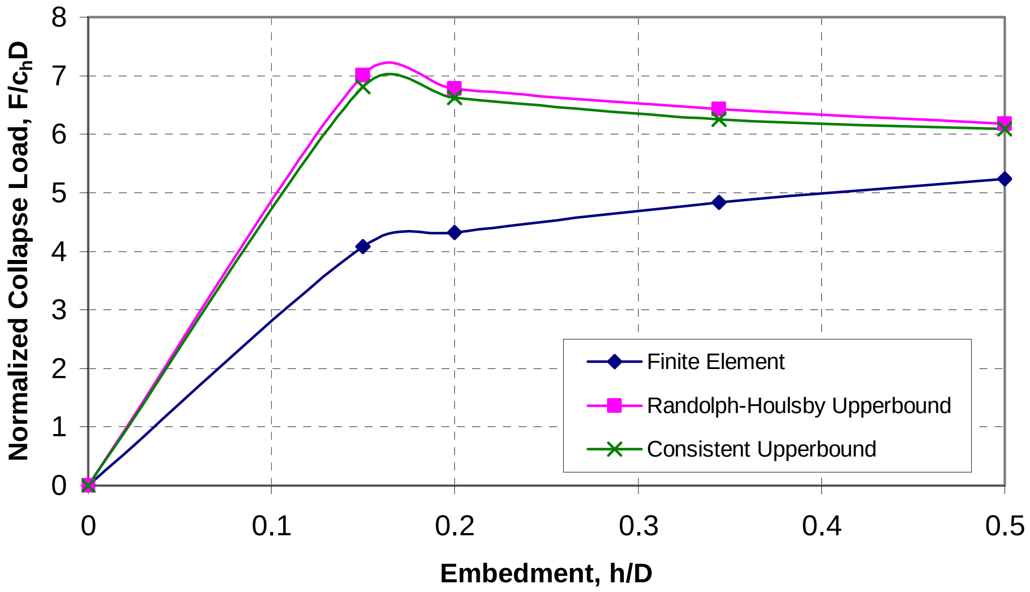

b. Rough

Figure 3.16 Collapse Loads for Cylinders of *h/D*≤0.5, η=∞

Figures 3.17 and 3.18 compare finite element and upper bound solutions at embedments of $h/D>0.5$. Figure 3.17a compares solutions for uniform soil strength profile and smooth cylinder boundary condition. The collapse loads predicted from the upper bound solution increase rather abruptly between cylinder embedments $0.5<h/D<1$, beyond which they becomes constant. Such a trend is predictable for this presumed failure mechanism, since no additional soil resistance can be mobilized once the horizontal free surface lies above the slip line field boundary (Figure 3.4). The finite element solution indicates the abrupt break in the upper bound solution (Figures 3.17a) to be unrealistic. Refinement of the upper bound solution to allow the passive wedge to exit at an optimized angle (Martin, 2001) could likely smooth these abrupt transitions. The upper bound solution overestimates the finite element solution most severely - by about 50%- at relatively low embedments in the range $1<h/D<2$. At greater embedment depths, the finite element predictions gradually trend toward the upper bound solution. The upper bound solution for a smooth boundary and linearly varying strength profile, $\eta=\infty$, in Figure 3.18a begins to significantly diverge from the finite element solution at embedments $h/D>1$. Beyond $h/D>1.5$, it roughly parallels the finite element solutions, exceeding it by about 20%. The comparison of the upper bound solutions for a rough boundary in Figures 3.17b and Figure 3.18b to the finite element solutions is similar to that of the smooth case.

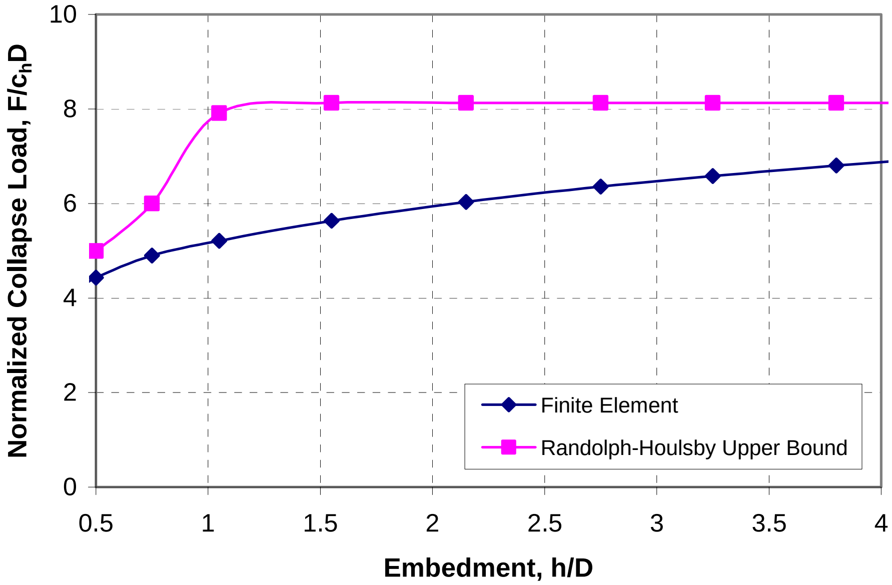

a. Smooth

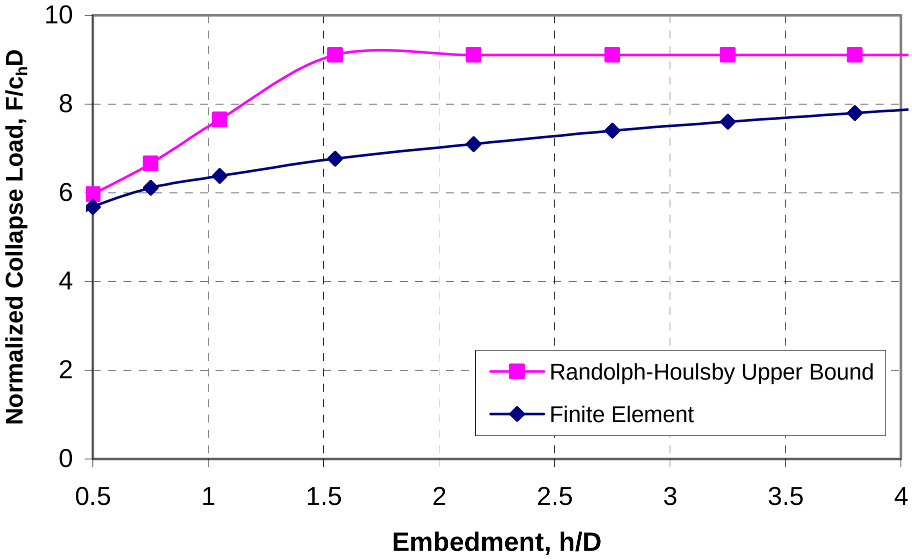

b. Rough

Figure 3.17 Collapse Loads for Cylinders of *h/D*>0.5, η=0

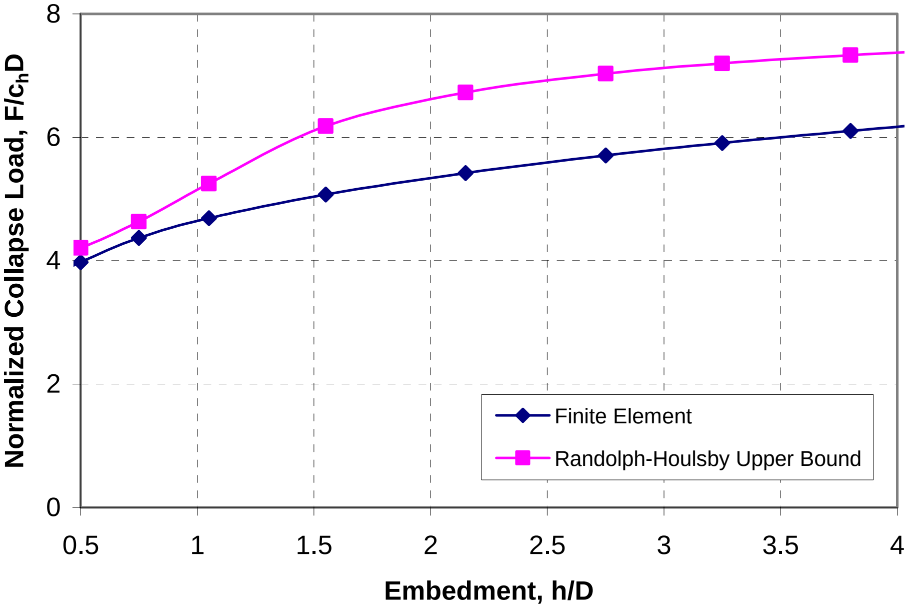

a. Smooth

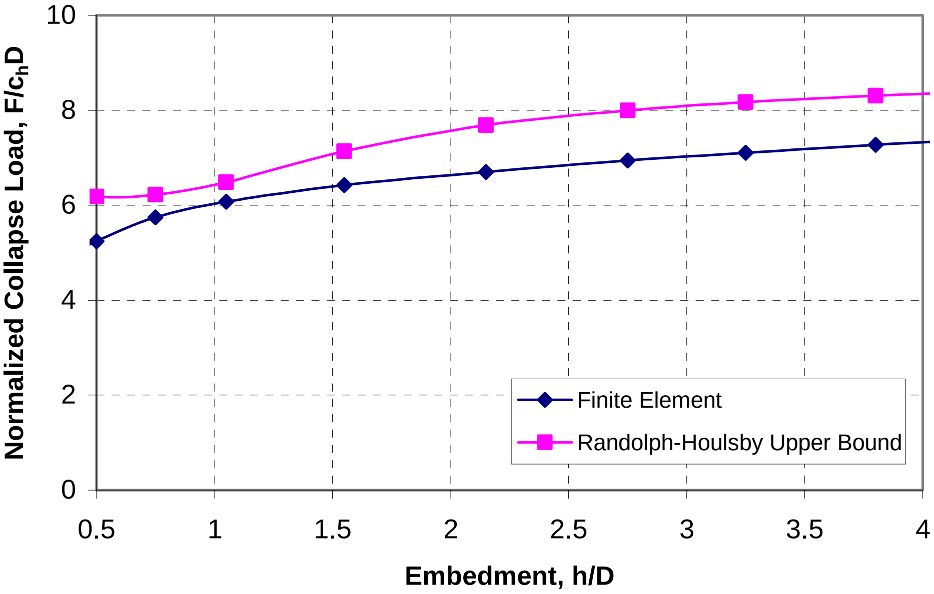

b. Rough

Figure 3.18 Collapse Loads for Cylinders of *h/D*>0.5, η=∞

For simplified calculations, the finite element predictions presented above may be fitted to an empirical power law expression of the form:

$$F/c_hD = a\,(h/D)^b \tag{3.22}$$

The fitting coefficients a and b for limiting conditions of roughness (perfectly smooth and rough) and limiting soil strength profiles, $\eta = 0$ and ∞, are tabulated in Table 3.7. Figure 3.20 shows that the curve fits match excellently with the finite element solutions.

Application of Eq. 3.22 to general conditions of η is desirable for practical applications. The MOC analyses summarized in Figure 3.3 indicate that collapse loads normalized by soil strength at the bottom of the cylinder, c_h, fall into a relatively narrow band for various η. Comparisons of the finite element predictions for the limiting cases $\eta = 0$ and ∞ (Figure 3.19) similarly suggest that collapse loads normalized by c_h are relatively insensitive to η. For general conditions of η, Table 3.7 presents fitting coefficients a and b that reflect the average of the limiting conditions. Figure 3.19 shows predicted collapse loads for limiting values of η to deviate from the best fit to vary by a maximum of 10% at very low embedments ($h/D = 0.1$) and less than 5% at greater embedments.

Table 3.7 Fitting Coefficients between Collapse Load and Cylinder Embedment (Aubeny et al., 2005)

Strength Gradient η	Boundary Roughness	Coefficients a, b	
		$h/D<0.5$	$h/D>0.5$
0	Smooth	$a = 5.42$ $b = 0.29$	$a = 5.16$ $b = 0.21$
	Rough	$a = 7.41$ $b = 0.37$	$a = 6.35$ $b = 0.15$
∞	Smooth	$a = 4.44$ $b = 0.17$	$a = 4.62$ $b = 0.21$
	Rough	$a = 6.02$ $b = 0.20$	$a = 5.95$ $b = 0.15$
Entire Range $0 \le \eta \le \infty$	Smooth	$a = 4.97$ $b = 0.23$	$a = 4.88$ $b = 0.21$
	Rough	$a = 6.73$ $b = 0.29$	$a = 6.15$ $b = 0.15$

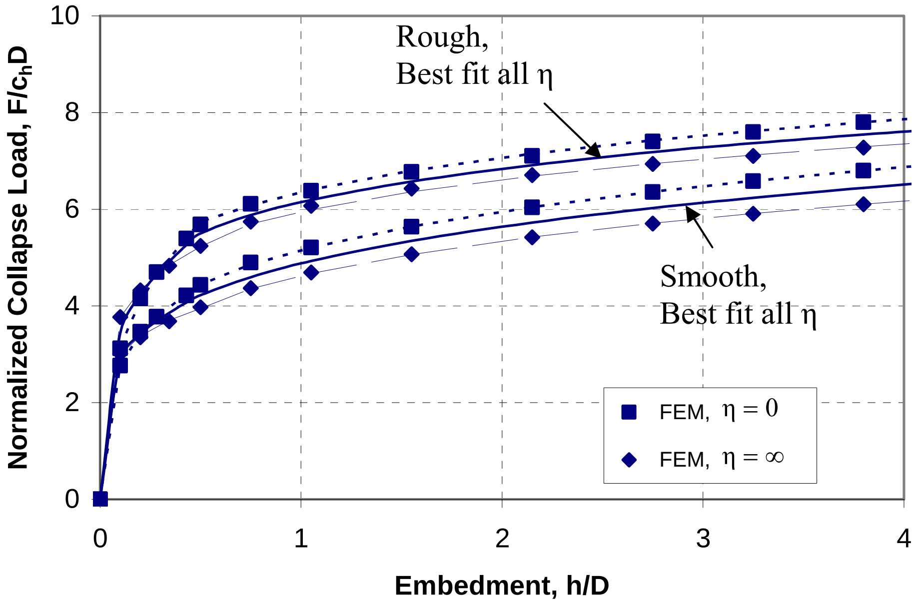

Figure 3.19 Empirical Curve Fits

Figure 3.20 illustrates the finite element solution for the XBP studies. A sharp break occurs in the collapse load – embedment depth curve at about $h/d = 1.2$, which is about at the depth where an open trench begins to form in the wake of the advancing penetrometer. The result also shows that the collapse load tends to reach a limit at deep penetrations. As with the cylinder studies, the finite element predictions were fitted to a simplified empirical form. Eqs. 3.23a and 3.23b fit the finite element predictions to power law functions as follows:

If $h/d \le 1.2$

$$F/cA = 8.55\ (h/d)^{0.756} \tag{3.23a}$$

If $h/d > 1.2$

$$F/cA = 9.60\ (h/d)^{0.21} \tag{3.23b}$$

where A is the maximum cross sectional area, and d is the diameter at the maximum section. The curve fits, shown by dashed lines in Figure 3.20, satisfactorily match the finite element predictions.

Preliminary studies on hard layer effects were conducted for cases of $t/d = 0.5$, $c_i/c_s = 5$ and 10. To minimize the free surface effect, finite element simulations were performed starting from embedments of $h/d = 5$. Figure 3.21 shows that the collapse load is almost constant for the uniform case ($c_i/c_s = 1$) as the embedment increases. For the non-uniform cases, the collapse loads change little before the tip gets close to the hard layer. The collapse loads increase significantly as the tip comes into contact with the hard layer and continue to increase as more area comes into contact. As the tip penetrates through the hard layer the collapse loads decline. The results also show that the increment of the collapse load for $c_i / c_s = 10$ compared to the uniform case is about twice that of $c_i / c_s = 5$.

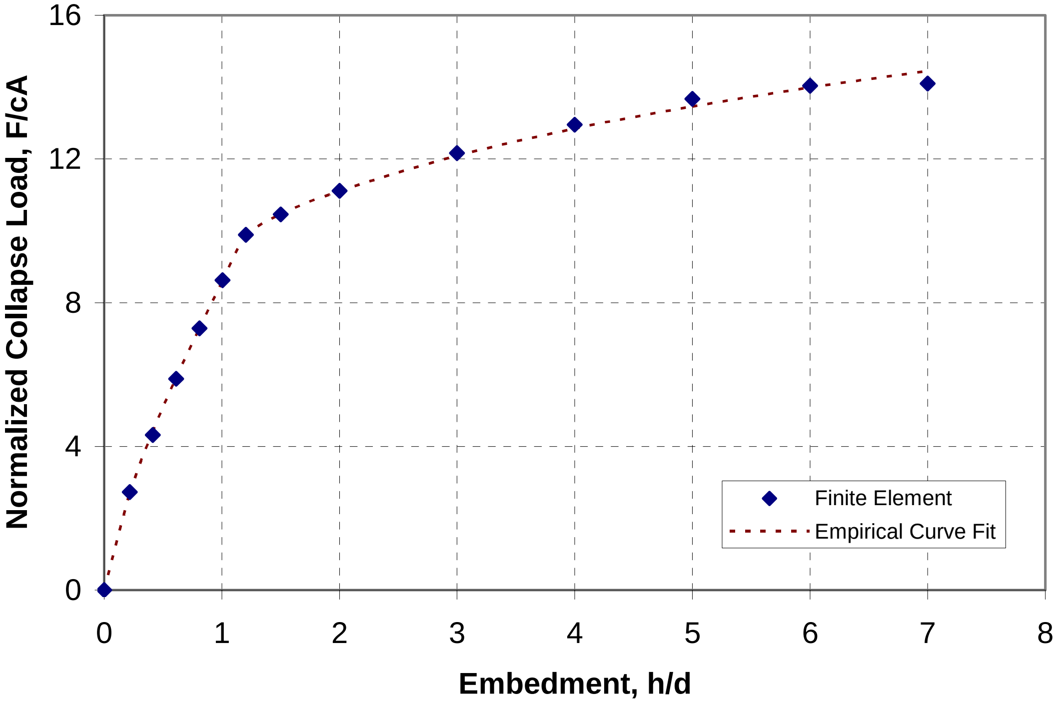

Figure 3.20 Collapse Loads for the XBP Penetration

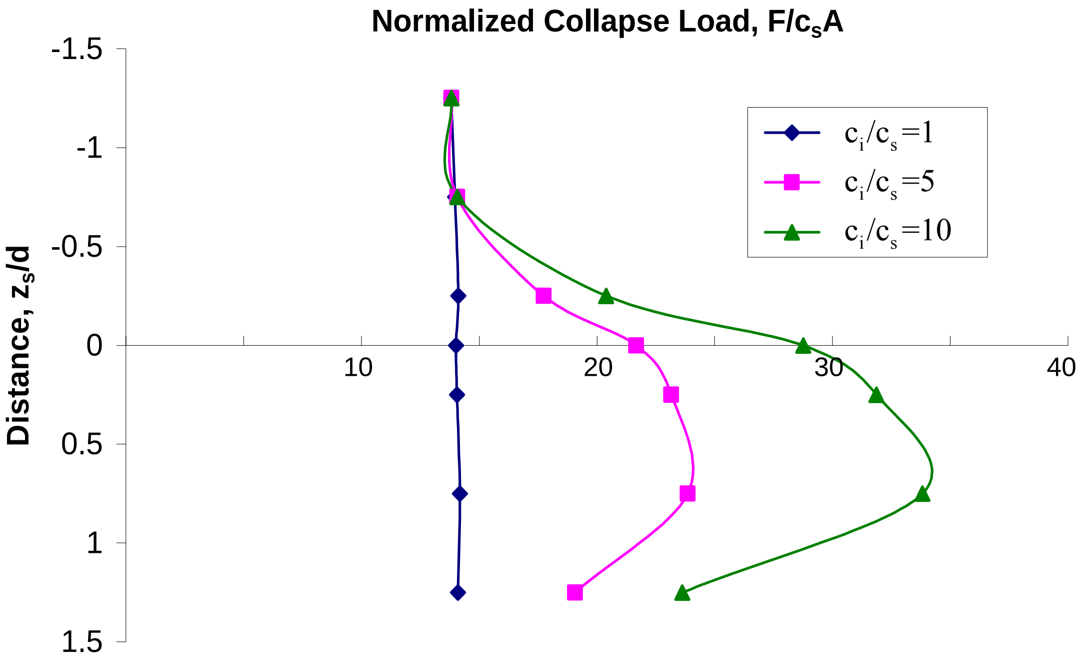

Figure 3.21 Preliminary Hard Layer Study Results

CHAPTER IV

RATE-DEPENDENT STUDIES

4.1 Rate-Dependent Strength Model

The dependence of undrained shear strength on strain rate may be characterized in terms of a semi-logarithmic relation:

$$c = c_{ref}\left[1+\rho_{ref}\log_{10}\left(\dot{\varepsilon}/\dot{\varepsilon}_{ref}\right)\right] \tag{4.1}$$

where $c =$ undrained shear strength at strain rate $\dot{\varepsilon}$

$c_{ref} =$ undrained shear strength at reference strain rate $\dot{\varepsilon}_{ref}$

$\rho_{ref} =$ strain rate parameter associated with the reference strain rate $\dot{\varepsilon}_{ref}$

Data by Sheahan et al. (1996) suggest the existence of a threshold strain rate, $\dot{\varepsilon}_0$, below which strain rate effects are negligible. In re-sedimented Boston Blue Clay, reported threshold strain rates were 0.5 and 5%/hr for over-consolidation ratios (OCR) of 4 and 8, respectively. For lower OCR, thresholds were not encountered for strain rates down to 0.05%/hr. Hence, for normally and lightly over-consolidated soils, the lower limit of strain rate, or threshold strain rate for which Eq. 4.1 is valid, is a matter of some uncertainty. The maximum strain rates investigated in previously reported investigations are typically on the order of 50%/hr (Sheahan et al., 1996), with a single study considering strain rates up to 670%/hr (Vaid and Campanella, 1977).

Having noted the considerable uncertainty in the range of strain rates for which Eq. 4.1 is valid for normally consolidated clays, the following assumptions were made for the present study (Aubeny and Shi, 2005a): (1) a threshold strain rate of 0.05%/hr, and (2) no upper bound of strain rate. Since the selection of a reference strain rate is arbitrary, in this study the reference strain rate will be taken as the threshold value unless otherwise noted. Figure 4.1 illustrates the rate-dependent strength model employed in this study, which can be formulated as follows:

If $\dot{\varepsilon} \le \dot{\varepsilon}_0$

$$c = c_0 \tag{4.2a}$$

If $\dot{\varepsilon} > \dot{\varepsilon}_0$

$$c = c_0[1 + \rho_0 \log(\dot{\varepsilon} / \dot{\varepsilon}_0)] \tag{4.2b}$$

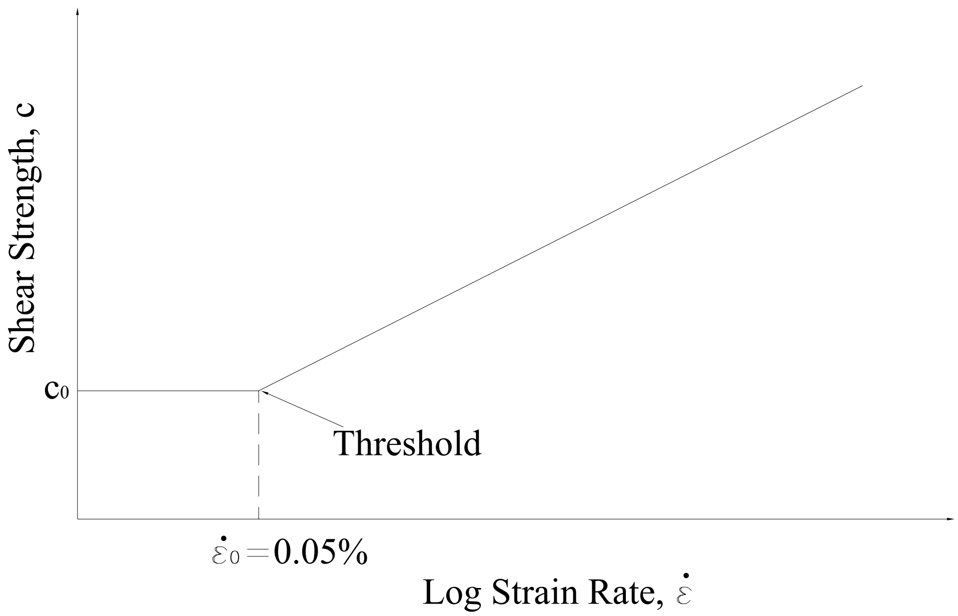

Figure 4.1 Rate-Dependent Strength Model

The data by Sheahan (1996) also show that ρ_{ref} is not in general constant, but tends to increase with increasing strain rate; i.e., soil shearing resistance actually increases at a rate greater than that predicted from the simple semi-logarithmic law in Eq. 4.1. Data from miniature vane shear tests conducted at variable vane peripheral velocities (Biscontin and Pestana, 2001) indicate a similar trend.

4.2 Finite Element Studies for Cylinders

Eq. 4.1 describes rate dependent soil resistance at a point. To characterize the total soil shearing resistance F_{s} of a cylinder of diameter D at an instantaneous velocity v, an analogous equation may be considered (Aubeny and Shi, 2005a):

$$F_{\text{s}} = F_{\text{s}0}\left[1+\lambda_0 \log_{10}\left(v/D\dot{\varepsilon}_0\right)\right] \tag{4.3}$$

The threshold soil resistance F_{s0} in Eq. 4.3 is the quasi-static soil shearing resisting force computed using a soil strength corresponding to the threshold strain rate $\dot{\varepsilon}_0$, and λ_0 is the strain rate multiplier for a cylinder embedded in a trench. The strain rate parameter λ_0 is analogous to the parameter ρ_0 in Eq. 4.2b; however, the existence of a threshold strain rate below which strength remains constant precludes the possibility that λ_0 may be identically equal to ρ_0. The first objective of the finite element studies is, therefore, to evaluate λ_0 in relation to ρ_0 for various conditions of (1) dimensionless velocity $v/D\dot{\varepsilon}_0$, (2) dimensionless penetration h/D. The second objective is to evaluate the accuracy of applying Eq. 3.22 to Eq. 4.3 in obtaining estimates of the soil resisting force F_{s} corresponding to penetration velocity v. For the purposes of the mine impact penetration investigations that motivated this research, a range of dimensionless velocities $v/D\dot{\varepsilon}_0$ up to 10^9 are taken as the range of interest.

4.2.1 Finite Element Model

The rate-dependent finite element analysis used the same geometry model, finite element mesh and element type as the rate-independent studies. The boundary conditions are also the same, except that the cylinder was modeled as a circular cavity translating downward at a constant velocity v instead of a prescribed displacement.

The soil was modeled as a rate-dependent, isotropic hardening material with a von Mises yield criterion and associated flow rule. This is possible by using the "RATE DEPENDENT, TYPE=YIELD RATIO" option together with the "PLASTIC, HARDENING=ISOTROPIC" option in ABAQUS. The yield ratio is defined as

$$\sigma_y = \sigma_{y0} R(\dot{\varepsilon}) \tag{4.4}$$

where σ_y is the yield stress at strain rate $\dot{\varepsilon}$, σ_{y0} is the static yield stress, and R is the yield ratio at strain rate $\dot{\varepsilon}$. For a von Mises yield criterion, the yield stress is $\sqrt{3}$ times the strength in simple shear. Combining with Eq. 4.2a and Eq. 4.2b we have

If $\dot{\varepsilon} \le \dot{\varepsilon}_0$

$$R(\dot{\varepsilon}) = 1 \tag{4.5a}$$

If $\dot{\varepsilon} > \dot{\varepsilon}_0$

$$R(\dot{\varepsilon}) = 1 + \rho_0 \log(\dot{\varepsilon}/\dot{\varepsilon}_0) \tag{4.5b}$$

The loading step is similar with that of the rate-independent study, i.e., the collapse load is achieved when the cylinder moves at a certain displacement. However, since we prescribe velocity instead of displacement in this case, ABAQUS calculates a displacement increment by multiplying the velocity of the cylinder by the time increment.

4.2.2 Finite Element Results

Figure 4.2 illustrates the effects of rate-dependent shear strength for velocities $v/D\dot{\varepsilon}_0$ of 0 through 10^9 for a cylinder embedded at a depth h/D =2.15 with a strain rate multiplier $\rho_0 = 0.15$. This figure shows the magnitude of $\sqrt{J_2}$ (where J_2 is the second invariant of the deviatoric stress tensor) along the centerline beneath the cylinder for collapse loading conditions. Recalling that the von Mises yield condition is $J_2^{1/2} - k = 0$, the calculated $\sqrt{J_2}$ is normalized by the static soil strength k_0 to evaluate the strain rate effects.

The predictions show that for quasi-static conditions, $v/D\dot{\varepsilon}_0$ = 0, the elasto-plastic boundary occurs at a depth of about z/d = 3.1 below the bottom of the cylinder and the mobilized shearing resistance is essentially constant within the plastic region. In contrast, for “high” penetration velocities, say $v/D\dot{\varepsilon}_0 > 10^3$, the yielded region is slightly expanded, with the elasto-plastic boundary occurring at about z/D = 3.6-3.8. Further, the mobilized shearing resistance increases substantially within the yielded region in the vicinity of the cylinder boundary due to the variable strain rates that occur within this region. It may be noted that in all cases stress levels decline toward zero in the immediate vicinity of the cylinder boundary. This is a consequence of the rough boundary condition that leads to the formation of a "rigid" wedge of soil ahead of the cylinder ($z/D < 0.2$). As strains tend toward zero in this zone, deviatoric stress levels correspondingly decline (Aubeny and Shi, 2005a).

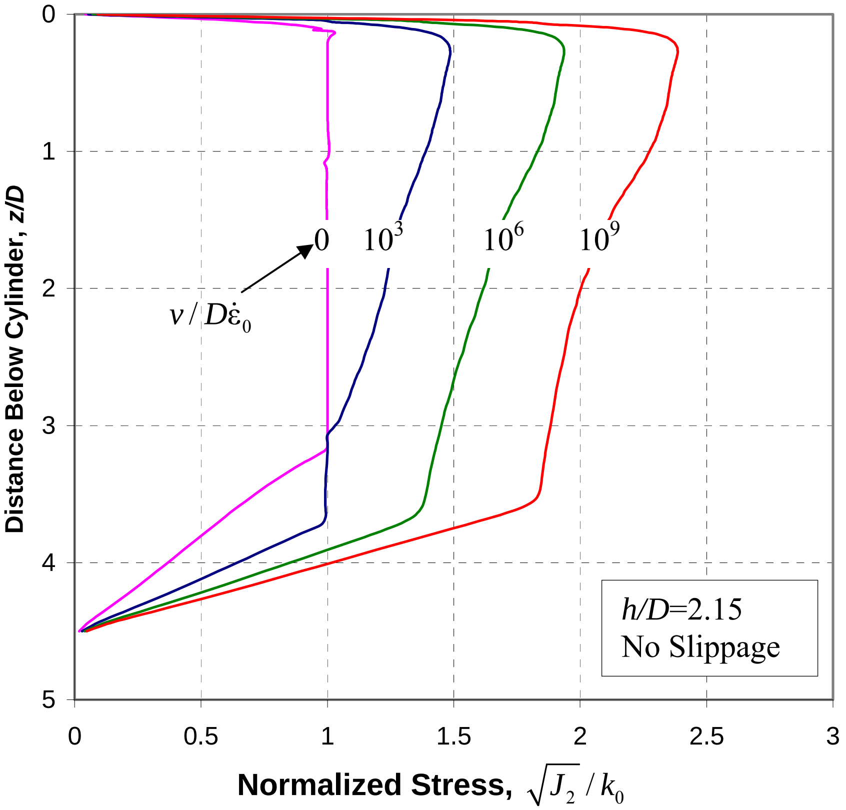

Figure 4.2 Stress Profile ahead of Cylinder at Various Penetration Velocities

The differences in the patterns of the stress distributions between the quasi-static and rate-dependent cases suggest that rate-dependent collapse loads will not be exact simple multiples of quasi-static loads; i.e., a simple normalization using Eq. 4.3 will not be valid in an exact sense. Nevertheless, an approximate normalization is possible as demonstrated in the following paragraph.

Fig. 4.3 shows typical finite element predictions of collapse load F_s versus penetration h/D for a uniform strength and no slippage condition. Such predictions together with Eq. 4.3 may be used to compute the relation between λ_0 and ρ_0 shown in Fig. 4.4. The predictions indicate that for high velocities, in the range $v/D\dot{\varepsilon}_0=10^6$ to 10^9, λ_0 deviates from ρ_0 by less than 6%. At lower velocities, the differences become more significant. At first glance, one might be tempted to conclude that Eq. 4.3 is inaccurate for low velocities. However, since the magnitude of the strain rate correction is relatively small at low velocities, the overall effect of the error in λ_0 on the total force computation is also relatively small as shown Fig. 4.5. Threshold collapse loads (computed from FEM) were applied to Eq. 4.3 with $\lambda_0 = \rho_0$ to estimate the increased resistance due to strain rate effects. Figure 4.5 shows that the collapse loads estimated from Eq. 4.3 are in reasonable agreement with finite element predictions at all velocity levels considered.

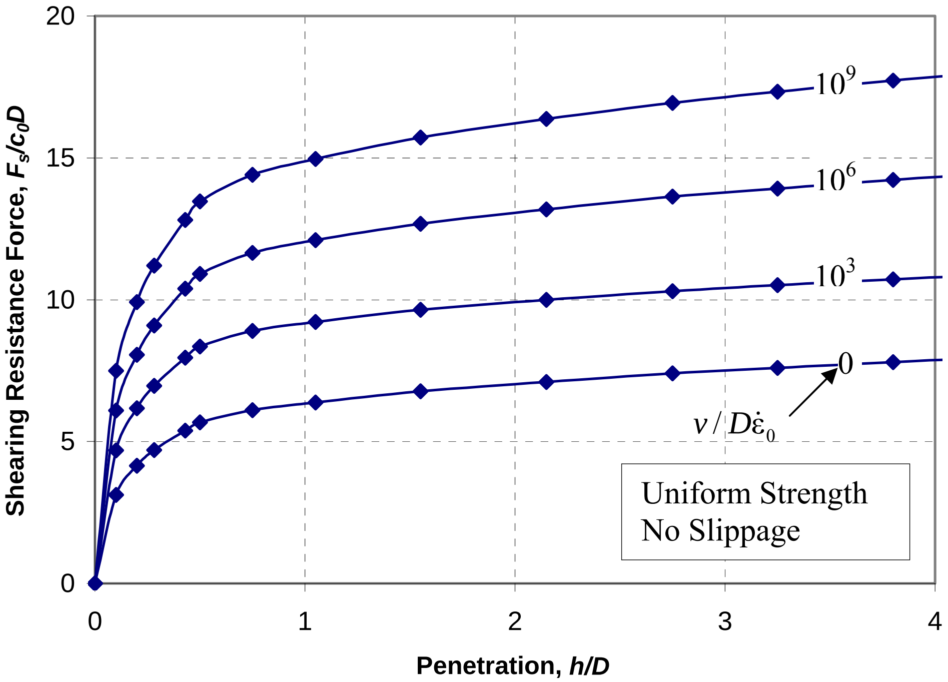

Figure 4.3 Finite Element Predictions of Collapse Loads at Various Velocities

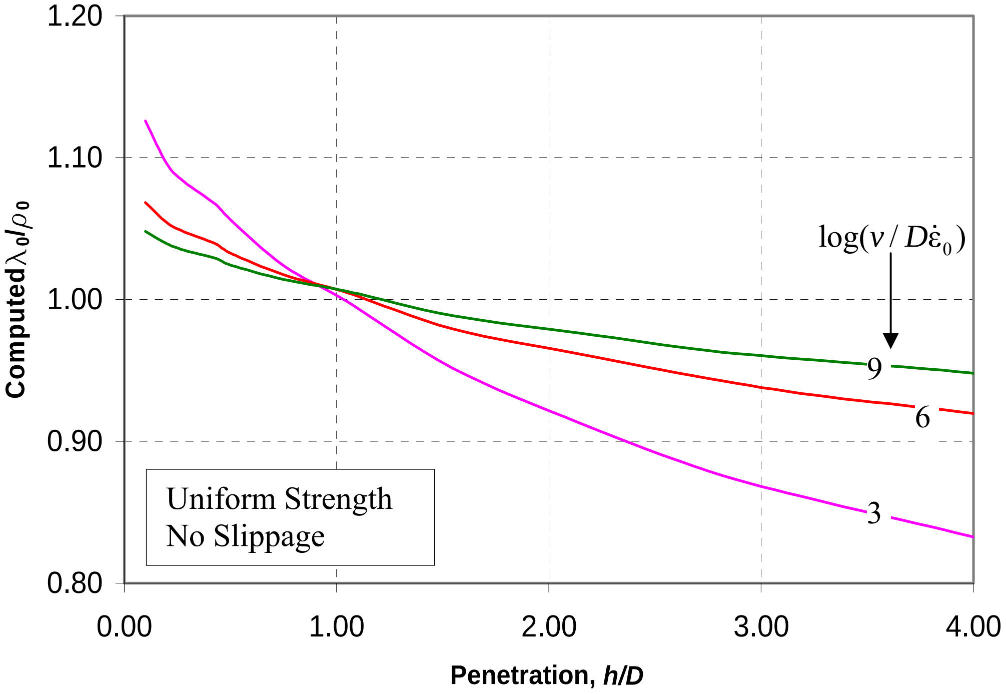

Figure 4.4 Comparison of Strain Rate Multipliers λ_0 and ρ_0

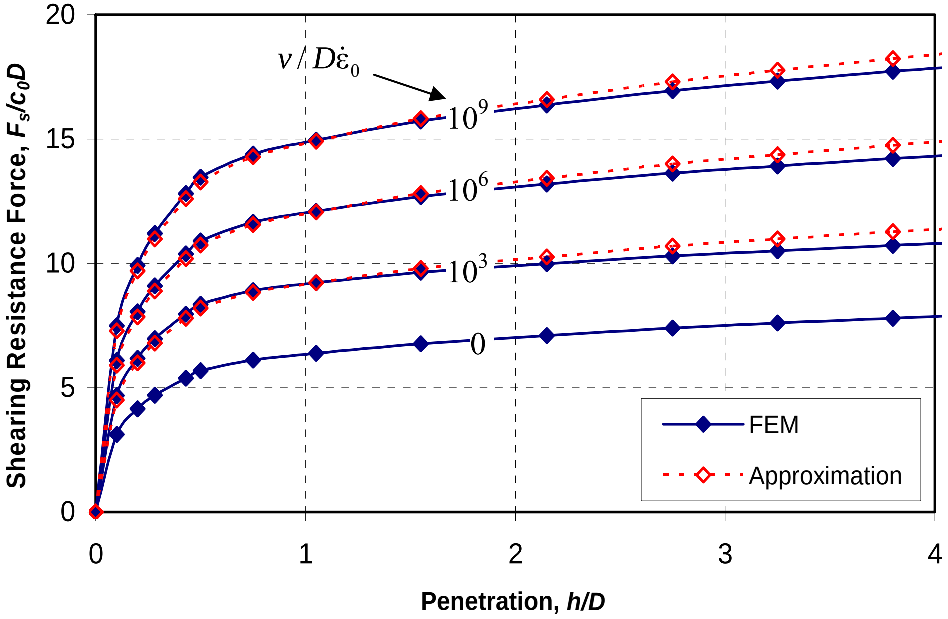

Figure 4.5 Simplified Prediction of Strain Rate Effects (Rough, η=0)

For smooth boundary or non-uniform strength conditions, the finite element results were also checked against the approximations by Eq. 4.3. For the smooth and uniform case (Figure 4.6), the approximations are in good agreement with the finite element results overall. For non-uniform cases with $\eta = \infty$, the collapse loads are normalized by c_{h0}, the threshold shear strength at the bottom of the penetrating cylinder. The approximations are about 10% lower than the finite element results at shallow penetrations and low velocities for both rough and smooth boundaries (Figures 4.7 and 4.8, respectively). Therefore, the approximations should be used with caution at shallow embedments. Nevertheless, when the penetration depth increases the approximations tend to match very well with the finite element results.

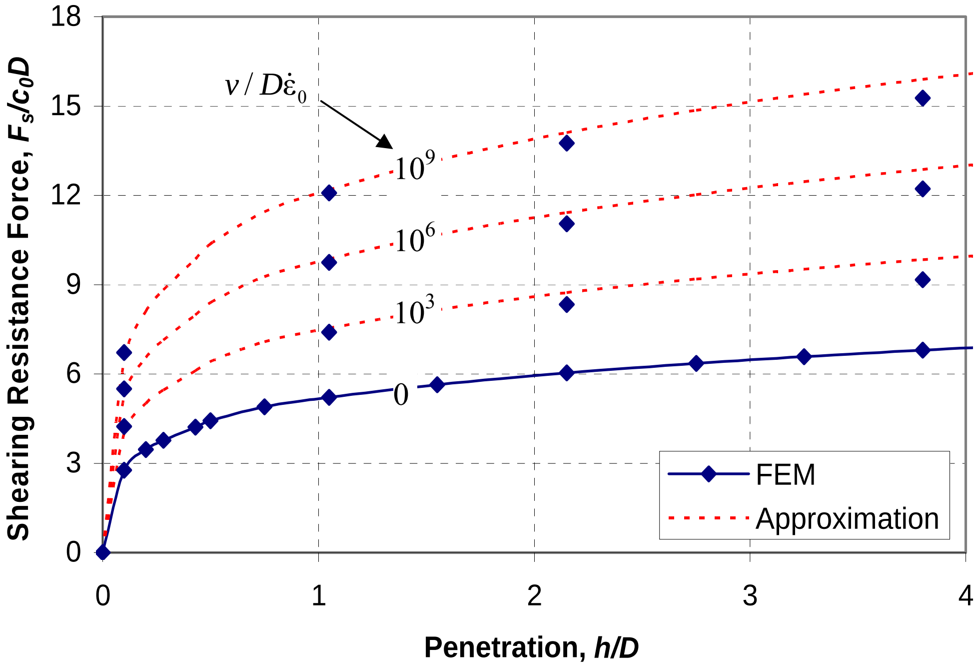

Figure 4.6 Simplified Prediction of Strain Rate Effects (Smooth, η=0)

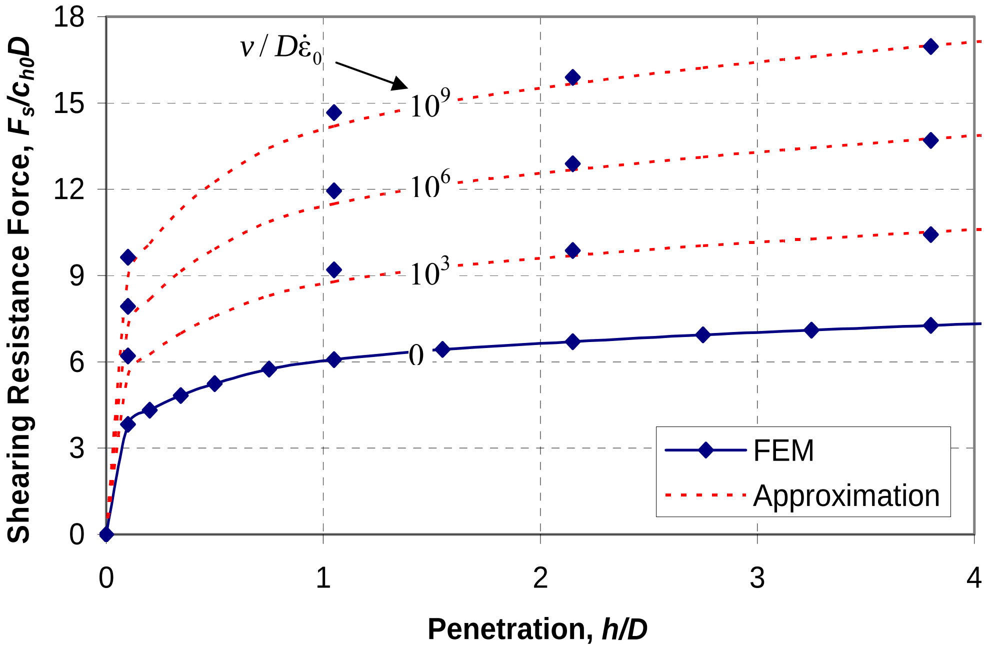

Figure 4.7 Simplified Prediction of Strain Rate Effects (Rough, η=∞)

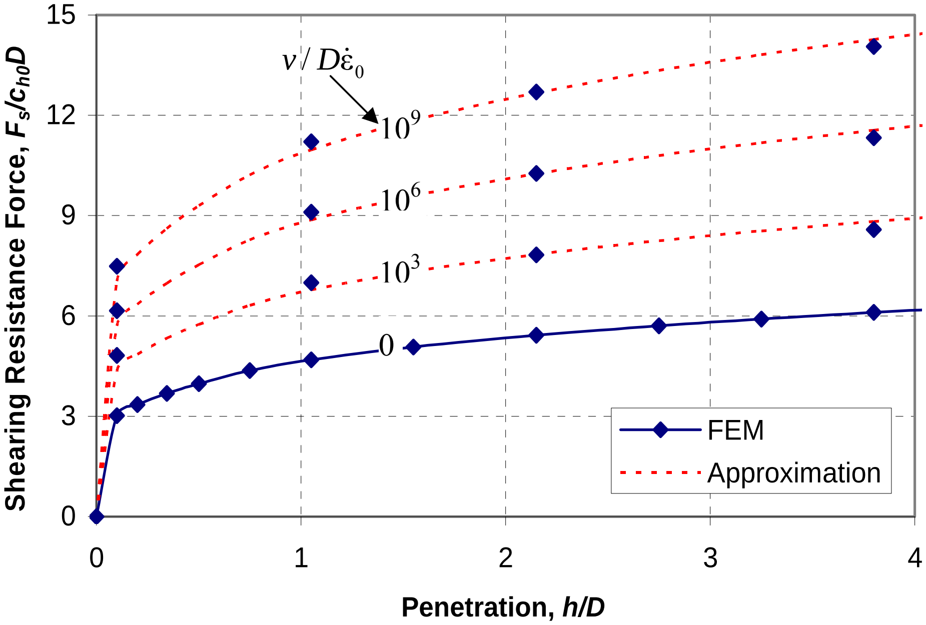

Figure 4.8 Simplified Prediction of Strain Rate Effects (Smooth, η=∞))

4.2.3 Empirical Resisting Force Relations

In the above section, finite element estimates of the threshold collapse loads were used in Eq. 4.3 to estimate collapse loads at elevated velocities accounting for strain rate effects. This section considers a further simplification in which (1) threshold collapse loads are estimated from Eq. 3.22, and (2) the effect of strain rate on total soil shearing resistance is estimated from Eq. 4.3.

Figure 4.9 presents the results of this procedure for uniform strength and no slippage condition, and the empirical fits show an overall excellent agreement with the finite element predictions of collapse loads. The empirical fits for other cases are also presented in Figures 4.10, 4.11 and 4.12, which are very close to the approximations in Figures 4.6, 4.7 and 4.8.

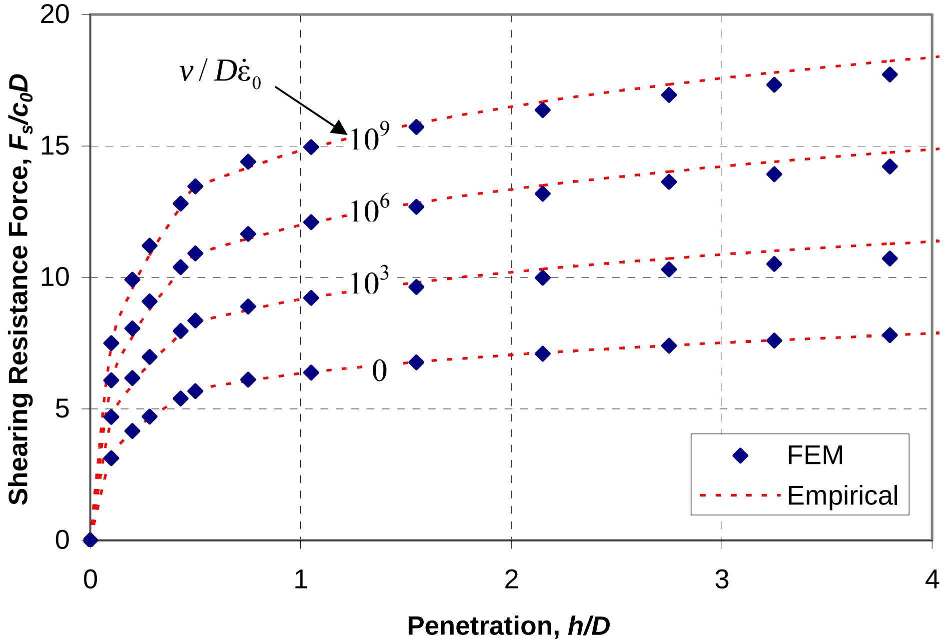

Figure 4.9 Evaluation of Empirical Estimates of Collapse Loads (Rough, η=0)

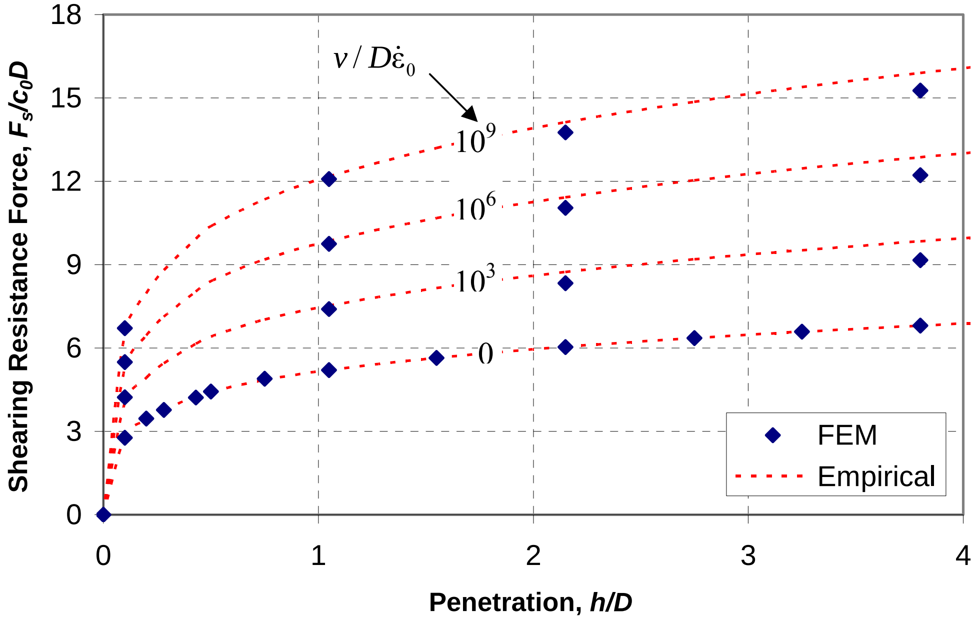

Figure 4.10 Evaluation of Empirical Estimates of Collapse Loads (Smooth, η=0)

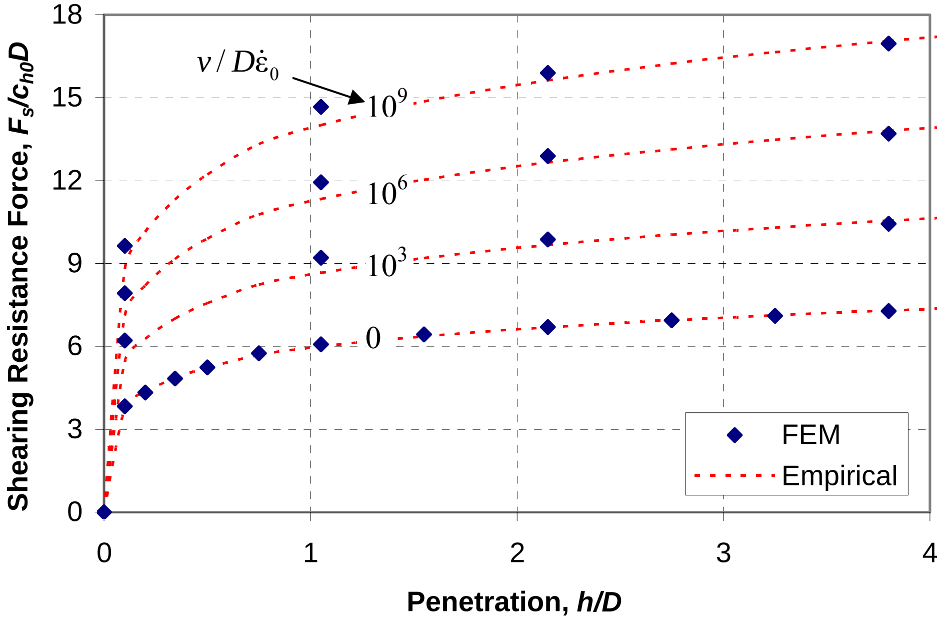

Figure 4.11 Evaluation of Empirical Estimates of Collapse Loads (Rough, η=∞)

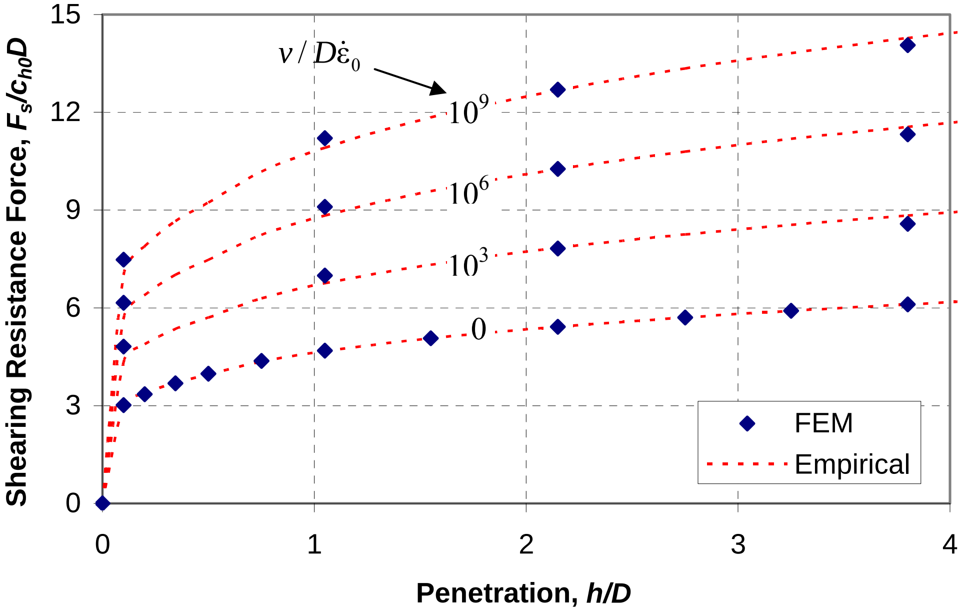

Figure 4.12 Evaluation of Empirical Estimates of Collapse Loads (Smooth, η=∞)

4.3 Finite Element Studies for XBPs

Rate-dependent studies for the XBP were conducted in the same manner as the cylinder studies. Velocities up to 3500 cm/sec were taken as the range of interest in this study. Similar approximation relationship as Eq. 4.3 was applied to the XBP studies, with *D* in Eq. 4.3 replaced by the diameter at the maximum section of the XBP in this case. Figure 4.13 presents the comparison between the approximations and the finite element results for a rough boundary and uniform strength condition. It can be seen that the approximations fit excellently with the finite element results. As with the cylinder studies, the empirical fits for the quasi-static case (Eqs. 3.23a and 3.23b) were used together with the approximations to produce empirical estimates at elevated velocities. The results shown in Figure 4.14 match with the finite element results satisfactorily.

4.4 Summary and Discussions

Based on the above studies, the soil shearing resistance force for penetrating cylinders may be empirically described by a logarithmic function:

$$N_c = N_{c0}[1+\lambda_0 \log_{10}(v/D\dot{\varepsilon}_0)] \tag{4.6}$$

where $N_{c0} = F_{s0}/c_{h0}D$; quasi-static bearing factor defined by Eq. 3.22

$N_c = F_s/c_{h0}D$; rate-dependent bearing factor

A similar equation may be used to approximate the soil shearing resistance force for the XBP:

$$N = N_0[1+\lambda_0 \log_{10}(v/d\dot{\varepsilon}_0)] \tag{4.7}$$

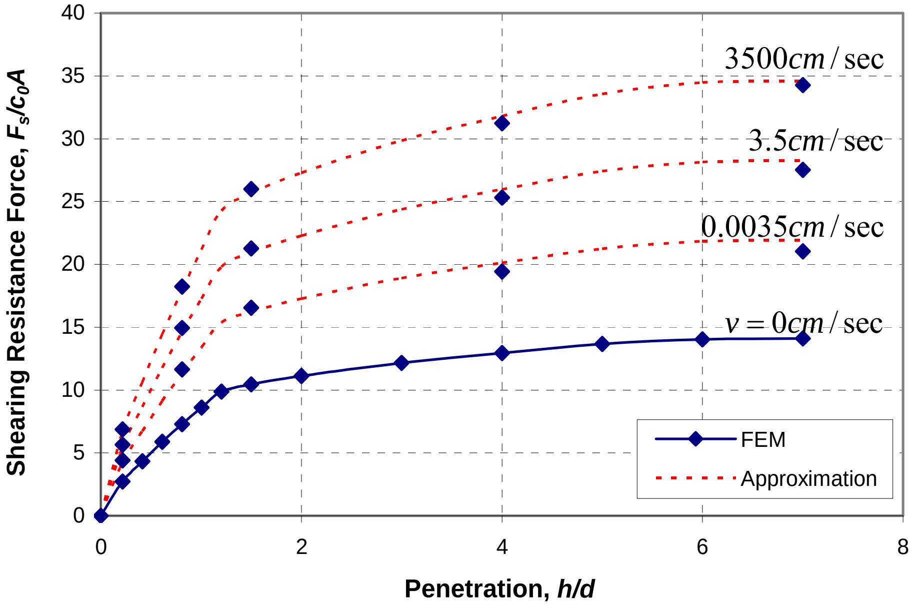

Figure 4.13 Approximation of the Strain Rate Effects for the XBP

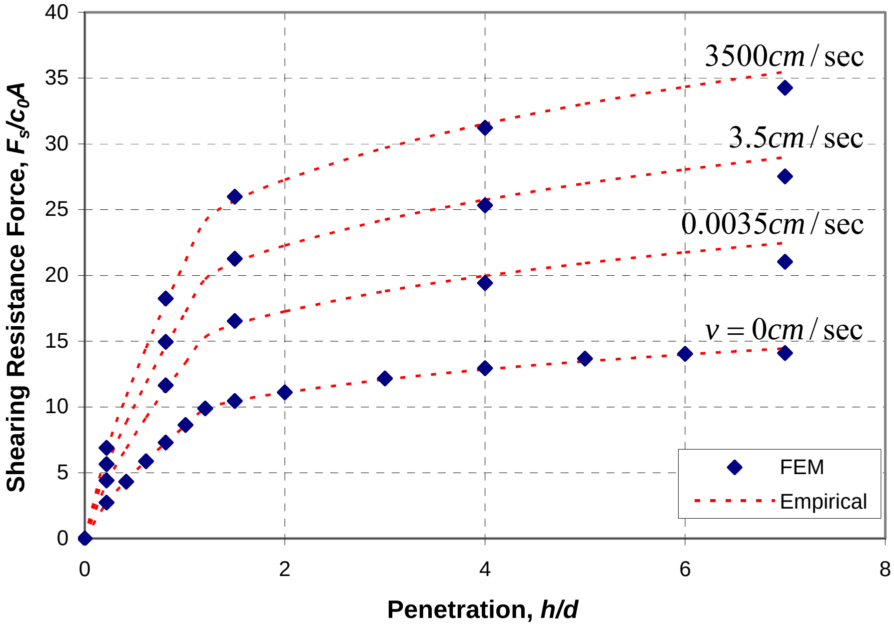

Figure 4.14 Empirical Estimates of the Collapse Loads for the XBP

where $N_0 = F_{s0} / c_0 A$; quasi-static bearing factor defined by Eqs. 3.23

$N = F_s / c_0 A$; rate-dependent bearing factor

For rate-dependent studies, direct use of the plastic limit analysis methods can not be made. A rate-dependent model can not include slip surfaces because strain rates are effectively infinite. However, the rate-independent solutions are still useful as reference cases.

In this analysis the inertial resistance of the soil is ignored because the range of impact velocities of interest is very low. Care should be taken to investigate these effects for significantly higher penetration rates.

CHAPTER V

PREDICTIVE MODELS

5.1 Penetration Studies

Based on the previously described studies and a rigid body projectile model, a predictive model for the depth of penetration of cylinders has been developed. Model predictions were compared to the results of the experimental penetration tests.

5.1.1 Penetration Model

If the penetrating cylinder is modeled as a rigid body, the forces acting on the cylinder during penetration include the weight W, soil shearing resistance force F_s, and the buoyancy force F_b (Figure 5.1). Thus, the acceleration of the cylinder can be defined by the following equation (Aubeny and Dunlap, 2003):

$$a / g = 1 - F_s / W - F_b / W \tag{5.1}$$

where a = acceleration of the cylinder

g = gravitational acceleration

The buoyant force F_b comprises the soil buoyant force and the buoyant force of water (if the cylinder is submerged). The buoyant force of water is simply the unit weight of water multiplied by the volume of cylinder being submerged. It was not considered in this analysis for the purpose of calibration with the penetration tests by Aubeny and Dunlap (2003), but it can be easily added.

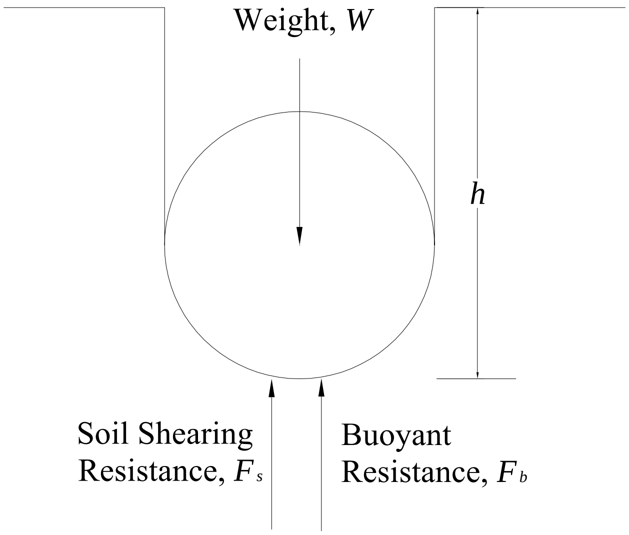

Figure 5.1 Acting Forces on a Penetrating Cylinder

The velocity and penetration depth of the cylinder can be obtained through direct integration:

$$v = v_0 + \int a dt \tag{5.2}$$

$$h = \int v dt \tag{5.3}$$

where v = velocity of the cylinder

v_0 = Impact velocity of the cylinder at the mudline

t = time

h = penetration depth

For generalization the following dimensionless parameters for acceleration, velocity, penetration depth and time are defined (Aubeny and Dunlap, 2003):

$$A = a / g \tag{5.4a}$$

$$V = v / \sqrt{gD} \tag{5.4b}$$

$$V_0 = v_0 / \sqrt{gD} \tag{5.4c}$$

$$H = h / D \tag{5.4d}$$

$$T = t\sqrt{D / g} \tag{5.4e}$$

By combining the above equations with Eqs. 5.2 and 5.3 we have

$$V = V_0 + \int A dT \tag{5.5}$$

$$H = \int V dT \tag{5.6}$$

The soil shear resistance force F_s can be calculated by combining Eqs. 3.22 and 4.3 together. Expressed by dimensionless parameters it gives

$$F_s / W = aH^b C_0 [1 + \lambda_0 \log_{10}(V / E_0)] \tag{5.7}$$

where $C_0 = \dfrac{c_{h0} LD}{W}$

c_{h0} = threshold strength at the bottom of the cylinder

L = length of the cylinder

$E_0 = \dfrac{\dot{\varepsilon}_0}{\sqrt{g / D}}$

For intermediate boundary roughness ($0 < \alpha < 1$) F_s may be approximated by linearly interpolating between the two limiting cases: smooth ($\alpha = 0$) and rough ($\alpha = 1$).

The soil buoyancy force is simply the soil unit weight times the volume displaced by the cylinder, which was given by Aubeny and Dunlap (2003). If h/D<0.5 (Figure 5.2a), the volume of the soil displaced by the cylinder is $2LA_{ABC}$, where A_{ABC} is the area of ABC in Figure 5.2a. Apparently

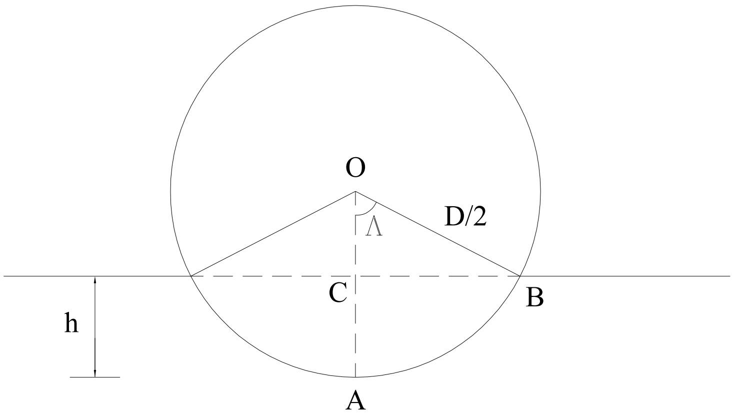

a. $h/D<0.5$

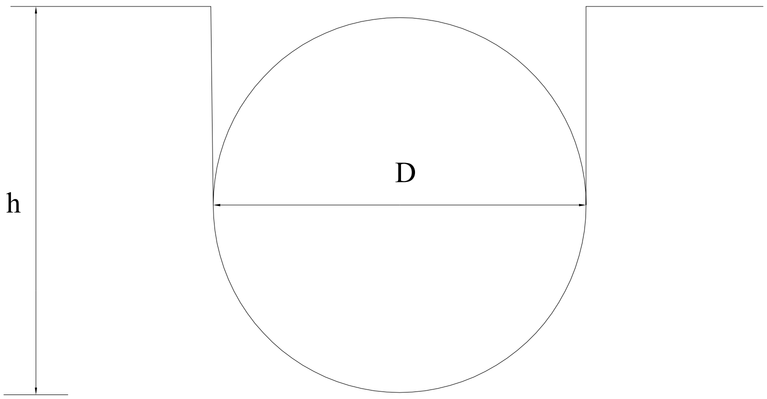

b. $h/D>0.5$

Figure 5.2 Calculation of Volume of Soil Displaced by the Cylinder

$$A_{ABC} = A_{OAB} - A_{OBC} \tag{5.8}$$

and

$$A_{OAB} = \frac{1}{2}\Lambda(\frac{D}{2})^2 = \frac{\Lambda D^2}{8} \tag{5.9a}$$

$$\cos\Lambda = OC/OB = \frac{D/2-h}{D/2} = 1-2\frac{h}{D} \tag{5.9b}$$

$$A_{OCB} = \frac{1}{2}OC \times CB = \frac{1}{2}(\frac{D}{2}-h)\sqrt{(\frac{D}{2})^2-(\frac{D}{2}-h)^2} = \frac{1}{2}(\frac{D}{2}-h)\sqrt{hD-h^2} \tag{5.9c}$$

Combining the above equations, we have

$$A_{ABC} = \cos^{-1}(1-\frac{2h}{D})\frac{D^2}{8} - \frac{1}{2}(\frac{D}{2}-h)\sqrt{hD-h^2} \tag{5.10}$$

Thus, the soil buoyancy force can be expressed in dimensionless form as

$$\frac{F_b}{W} = \Gamma[\frac{1}{4}\cos^{-1}(1-2H) - (\frac{1}{2}-H)\sqrt{H-H^2} \tag{5.11a}$$

where $\Gamma = \frac{\gamma L D^2}{W}$

γ =soil unit weight

If *h/D*>0.5 (Figure 5.2b), the volume of the displaced soil is simply $\frac{\pi L D^2}{8} + (h - \frac{D}{2})LD$. Therefore, the soil buoyancy force can be expressed by

$$\frac{F_b}{W} = \Gamma(\frac{\pi}{8} + H - \frac{1}{2}) \tag{5.11b}$$

Given the soil shearing resistance force and the buoyancy force defined above, the procedure to predict the penetration depth may be summarized as follows:

1. The soil shearing resistance force F_s and the buoyancy force F_b may be evaluated by Eqs. 5.7 and 5.11 respectively at each time step;
2. Acceleration A at each time step is determined by Eq 5.1;
3. Acceleration is integrated over each time step to update velocity V and embedment depth H.
4. The maximum penetration depth H_{max} occurs when velocity declines to zero.

A MATLAB program entitled MINE_BURIAL has been developed for this penetration model (Appendix D). Variables controlling predicted penetration can be expressed in terms of the strain rate multiplier, the boundary conditions at the soil-cylinder interface, impact velocity at the mudline, soil shearing resistance, soil unit weight effects, threshold strain rate and variable strength profile. The integration is achieved numerically due to the non-linear relationships between the resistance forces F_s , F_b and penetration depth H.

5.1.2 Parametric Studies

Fig. 5.3 illustrates the general nature of the predictions from the impact penetration model for conditions of a uniform strength profile ($\eta = 0$), a soil-cylinder adhesion $\alpha = 1$, mudline velocities V_0 of 0 and 2, shear resistance C_0 ranging from 0.1 to 0.5, unit weight $\Gamma = 0.5$, a threshold strain rate $E_0 = 2\text{x}10^{-8}$. The analyses consider strain rate mulipliers, λ_0 , for the range 0.05 to 0.15. One should note that for the case of $V_0 = 0$, substantial accelerations and velocities can develop until sufficient soil resistance is mobilized at greater penetration depths. Hence, $V_0 = 0$ cannot be considered a quasi-static condition, except under the special circumstance in which the soil resistance, C_0, is sufficiently high to preclude significant accelerations and velocities (Aubeny and Shi, 2005a).

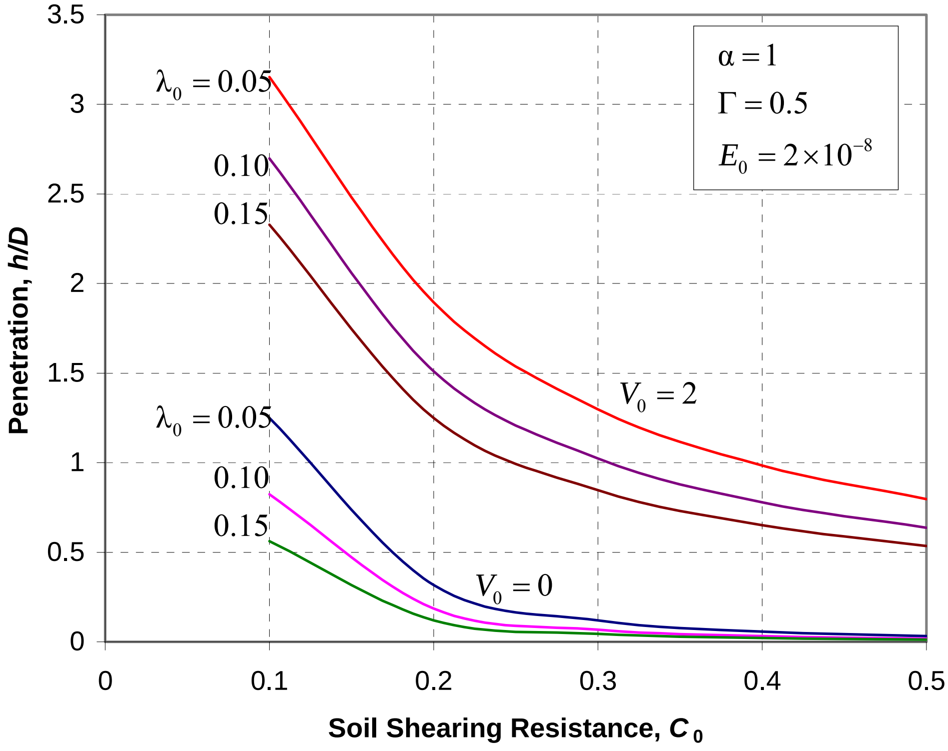

Figure 5.3 Parametric Study of Cylinder Penetration

Fig. 5.3 shows that mudline velocity is, as might be expected, of major significance, with predicted penetrations, *h/D*, for V_0 of 0 and 2 differing by nearly an order of magnitude in some cases. The magnitude of the strain rate multiplier can also be significant, with penetrations corresponding to $\lambda_0 = 0.05$ typically exceeding those for $\lambda_0 = 0.15$ by 50 to 100%.

5.1.3 Rate-Dependent Strength and Sensitivity

Due to the very soft soils under consideration, conventional laboratory tests involving uniform distributions of strains and strain rates were not feasible. In such circumstances, recourse must be taken to intrusive methods for strength measurements involving highly non-uniform distributions of strain and strain rates for which any assessment of strain rate effects entails considerable uncertainty. In the case of this study the MV shear apparatus was used to estimate soil strength, but a similar observation would apply to alternative intrusive test methods such as the cone penetrometer or the T-bar.

An assessment of the dependence of shear strength on strain rate is possible by varying the rate of rotation, $\dot{\theta}$, in the MV shear test. Fig. 5.4 illustrates the results of this procedure for the reconstituted marine soils under consideration in this study. While the MV shear strength versus rotation rate relationship in Fig. 5.4 is relatively simple, applying the data to the impact penetration model actually requires a number of assumptions, some of which have limited theoretical or experimental support at present. For the present study we assume that the MV shear strength fits a framework analogous to that defined by Eqs. 4.2; i.e., it may be expressed in terms of rotation rate as follows (Aubeny and Shi, 2005a):

$$c_{mv} = c_{mv0}\left[1+\lambda_{mv0}\log_{10}\left(\dot{\theta}/\ \dot{\theta}_0\right)\right] \tag{5.12}$$

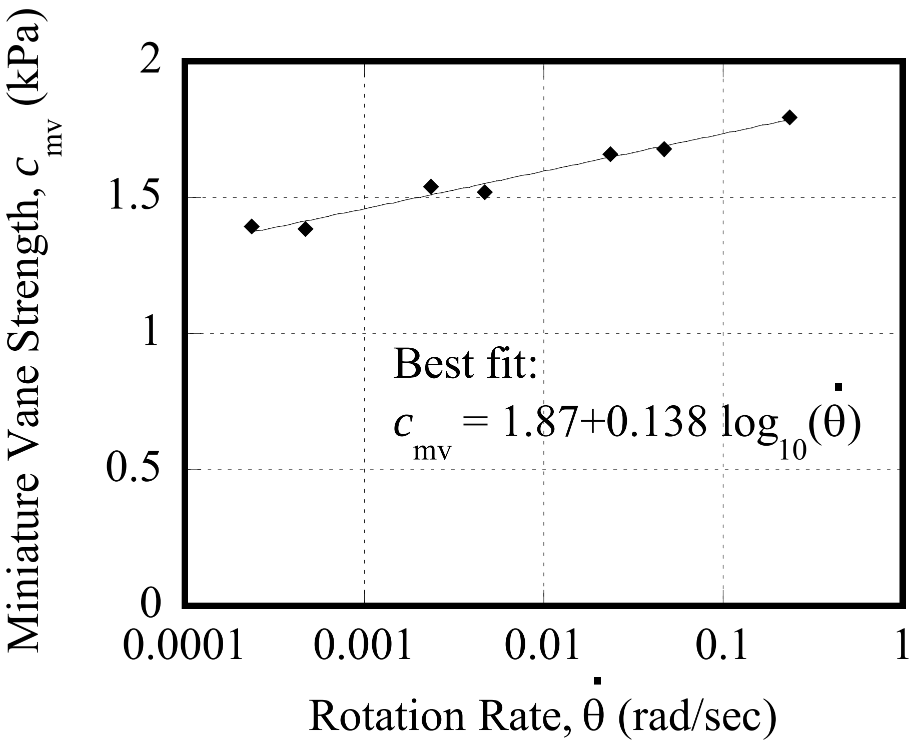

Figure 5.4 Strain Rate Dependence from MV Test (Aubeny and Shi, 2005a)

where c_{mv} is the shear strength associated with rotation rate $\dot{\theta}$, c_{mv0} is the threshold shear strength associated with the threshold rotation rate $\dot{\theta}_0$, and λ_{mv0} is the strain rate multiplier for the MV test.

We also assume that the MV strain rate multiplier λ_{mv0} approximates the strain rate multiplier for collapse loading of a horizontal cylinder and ρ_0. Furthermore, we assume that the threshold rotation rate $\dot{\theta}_0$ can be taken as the threshold strain rate $\dot{\varepsilon}_0$ (Aubeny and Shi, 2005a).

Regarding the first assumption, Biscontin and Pestana (2001) present a compilation of data supporting the form of Eq. 5.12, although a power law function is also possible. While the second assumption is certainly open to debate, it is at least intuitively plausible in view of the comparisons between λ_0 and ρ_0 presented earlier in this paper. The third assumption is perhaps of most concern; therefore, to assess its implications, the data in Fig. 5.4 were interpreted for the three arbitrarily assumed threshold rotation rates shown in Table 5.1. Using the parameters in Table 5.1 in conjunction with the range of mudline velocities, cylinder weights, and diameters relevant to this study yielded the parametric evaluation summarized in Figure 5.5. In all cases predicted penetrations proved to be insensitive to the assumed threshold rotation rate.

Table 5.1 Strain Rate Multipliers and Threshold Strengths for Various Assumptions of Threshold Strain Rate (Aubeny and Shi, 2005a)

Assumption	Threshold Rotation Rate, $\dot{\theta}_0$ (rad/sec)	Threshold Strength, c_{mv0} (kPa)	Strain Rate Multiplier, λ_{mv0}
1	1.4×10^{-7}	0.928	0.15
2	1.4×10^{-6}	1.07	0.13
3	1.4×10^{-5}	1.20	0.12

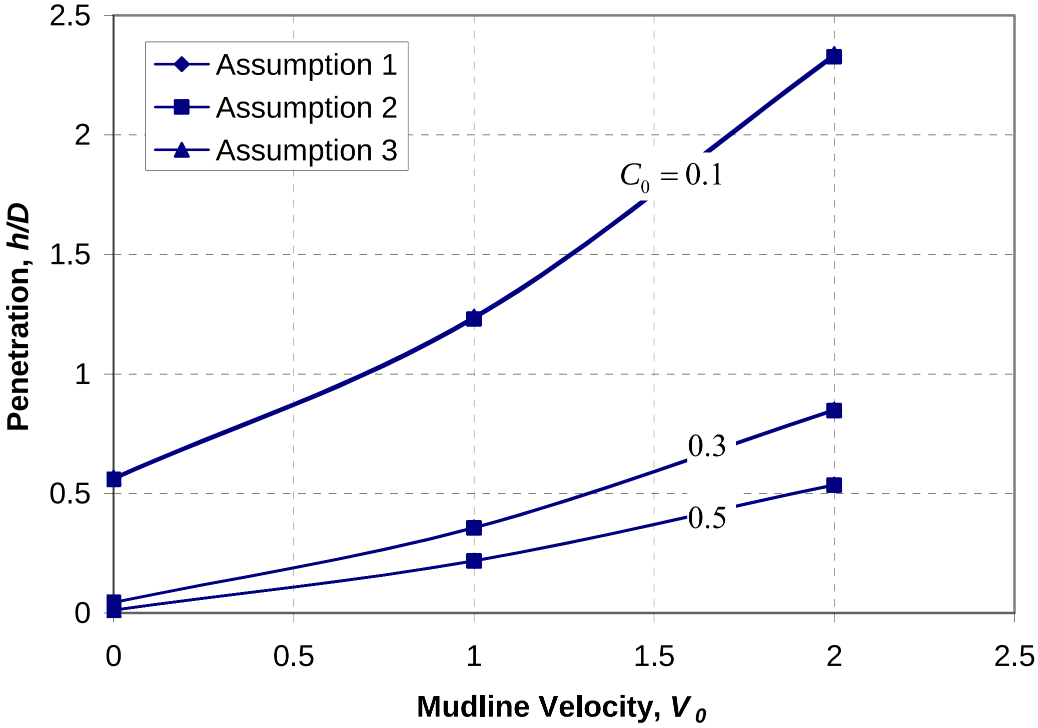

Figure 5.5 Effect of Assumed Threshold Strain Rate on Penetration Predictions (Γ=0.5)

The penetration predictions require an estimate of the boundary conditions at the soil-cylinder interface. In this study, this estimate proceeded on the basis of the sensitivity, S_t, of the soil, with the adhesion factor α taken as the reciprocal of S_t. The model cylinder penetration tests described previously entailed a procedure in which, prior to each test, the soil in the test basin was thoroughly mixed and remolded and allowed to set for 24 hours prior to testing. The measured thixotropic strength increase over a 24-hr setup period is shown in Figure 5.6. The sensitivity of the soil after the 24-hr setup period was therefore estimated by two approaches. The first method related the peak MV 24-hr strength to the MV strength measured immediately following remolding.

The second approach related the peak 24-hr strength to the residual strength measured at large rotations. Sensitivity measured on a residual strength basis was somewhat greater than that measured on a thixotropic peak strength gain basis, 1.3 versus 1.2. For the purpose of the penetration predictions, the sensitivity was taken as the average of these two values, resulting in a selected adhesion value for the analyses of α=0.8 (Aubeny and Shi, 2005a).

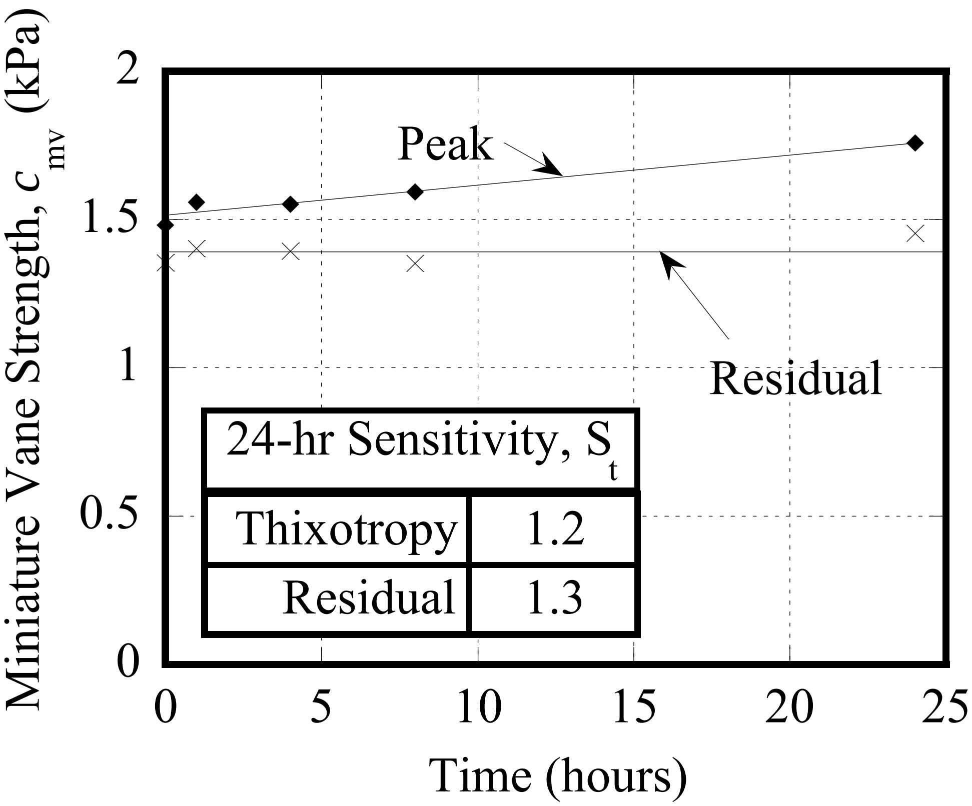

Figure 5.6 Estimated Sensitivity of Clays Used in Experimental Study (Aubeny and Shi, 2005a)

5.1.4 Comparison to Experimental Data

The model described above was used to interpret the experimental data in Table 2.1. Recalling that the cylinder had hemispherical ends (Figure 5.7), the effective length of the cylinder L_C was taken as the footprint area divided by the cylinder diameter to evaluate C_0 (Aubeny and Shi, 2005a). Thus

$$L_C = [(0.337)(0.168) + \frac{\pi(0.168)^2}{4}) / 0.168 = 0.467m \quad (5.13)$$

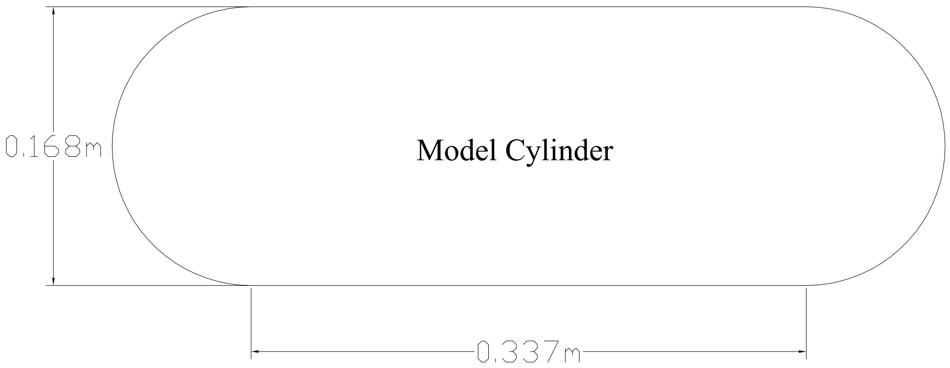

Figure 5.7 Geometry of the Model Cylinder

A similar approach was used for evaluating Γ, i.e., L_C was taken as the volume of the cylinder divided by the cross-sectional area. Thus

$$L_C = [\frac{\pi(0.168)^2(0.337)}{4} + \frac{4\pi}{3}(\frac{0.168}{2})^3]/[\frac{\pi}{4}(0.168)^2] = 0.449m \quad (5.14)$$

For cases in which the cylinder was inclined at an angle β, the horizontal projection of the cylinder length, $L_C' = L_C \cos\beta$, was taken as the effective cylinder length (Aubeny and Shi, 2005a). Based on experimental measurements, the value of γ used in this study is 16.7 kN/m^3.

Table 5.2 Test Conditions for Basin Tests Measuring Penetration of Cylinders into Reconstituted Marine Clay (Aubeny and Shi, 2005a)

Test Designation	Mudline Velocity V_0	Shearing Resistance $C_0{}^1$	Soil Unit Weight Γ
1	0	0.374	1.31
5	0	0.119	0.466
7	0	0.0839	0.384
8	0	0.0945	0.336
9	0	0.0850	0.284
22	1.41	0.297	0.758
23	1.61	0.117	0.466
24	1.39	0.117	0.283
25^2	1.31	0.220	0.758
26^2	1.36	0.134	0.466
27^2	1.46	0.0935	0.284
28^3	1.48	0.179	0.758
29^3	1.35	0.134	0.466
30^3	1.23	0.0828	0.284

1- Computed on a basis of c_0 referenced to a threshold strain rate = $1.4\text{x}10^{-7}$ sec^{-1}.
2- Axis of cylinder inclined 10^o from horizontal.
3- Axis of cylinder inclined 20^o from horizontal.

Mudline velocities, soil strengths, and soil unit weights of the penetration tests expressed in dimensionless form were summarized in Table 5.2. Tests performed at non-zero inclination angles are noted in Table 5.2. Predicted penetrations *h/D* were based on the dimensionless variables shown in Table 5.2, adhesion factors α of 0.8 and 1, a E_0 value corresponding to $\dot{\varepsilon}_0 = 1.4\text{x}10^{-7}$ sec^{-1} (0.05%/hr), a strain rate multiplier $\lambda_0 = 0.15$ (see Table 5.1), and a uniform strength profile ($\eta = 0$).

The predicted penetrations were compared to the measurements taken after 1 minute for the non-impact tests and 1 second for the impact tests. Figure 5.8 shows predicted versus measured penetrations. Hollow and solid symbols designate predictions based on adhesion factors α of 0.8 and 1, respectively. Tests performed at non-zero inclination angles β are also designated on the plot by crosses superimposed on the symbols. Predicted penetrations using $\alpha = 1$ were actually in slightly closer agreement with measurements than for $\alpha = 0.8$. That is, statistical analyses indicated a correlation coefficient between predictions and measurements $r^2 = 0.88$ for the $\alpha = 0.8$ predictions versus $r^2 = 0.90$ for the $\alpha = 1$ predictions. This may be viewed as somewhat unexpected in view of the sensitivity measurements, since an overestimate of the adhesion factor α should lead to an underestimate of penetration. One possible explanation is compensating errors. Specifically, as noted earlier, the predictions assume the formation of a vertical trench in the wake of the advancing cylinder. Neglecting the tendency of the walls of the trench to close in around the cylinder will tend to under-estimate the soil shearing resistance and over-estimate penetration. The soil inertial resistance was also neglected in this analysis. In addition, the soil shear resistance force is estimated from plane solutions; hence, end resistance effects are neglected. An over-estimate of the adhesion factor, $\alpha = 1$, may actually compensate for these effects, resulting in somewhat better predictions (Aubeny and Shi, 2005a).

The overall level of agreement between predicted and measured penetrations for the tests performed at inclinations β of 10 and 20 degrees is comparable to that for the horizontal tests, suggesting that predictions based on a horizontally oriented cylinder can provide reasonable penetration estimates for shallow inclination angles. Overall, given the level of uncertainty in characterizing the strength properties of the soil, the predicted penetrations agree reasonably well with measurements.

Figure 5.9 presents the predictions of penetrations without strain rate correction ($\lambda = 0$) for the $\alpha = 1$ case. We can see that the predictions distinctly over-estimate the penetrations when the effect of strength increase with strain rate is neglected, and the value of the statistical correlation coefficient r^2 is only 0.64. By comparison of Figure 5.8 and Figure 5.9 we may conclude that the mechanism of strain rate correction incorporated in this penetration model is effective.

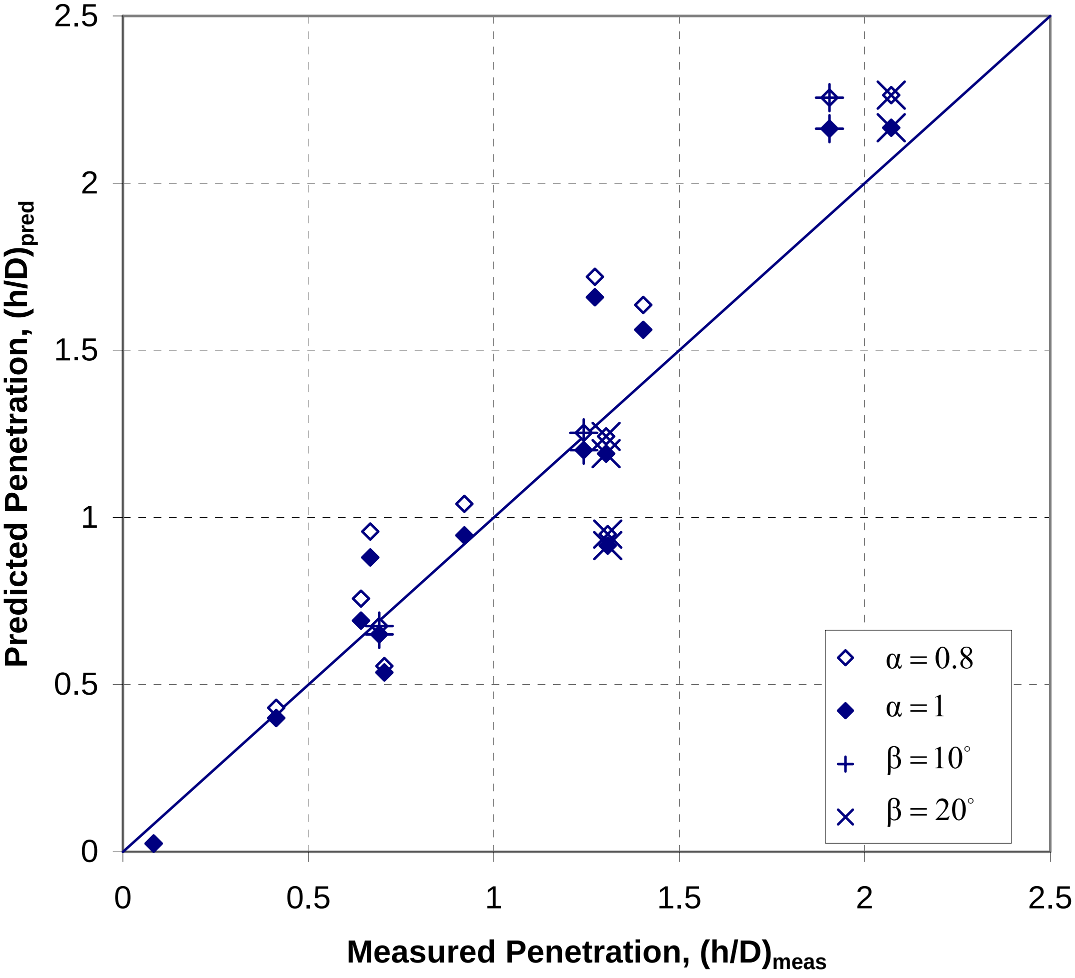

Figure 5.8 Predictions versus Experimental Measurements of Penetration

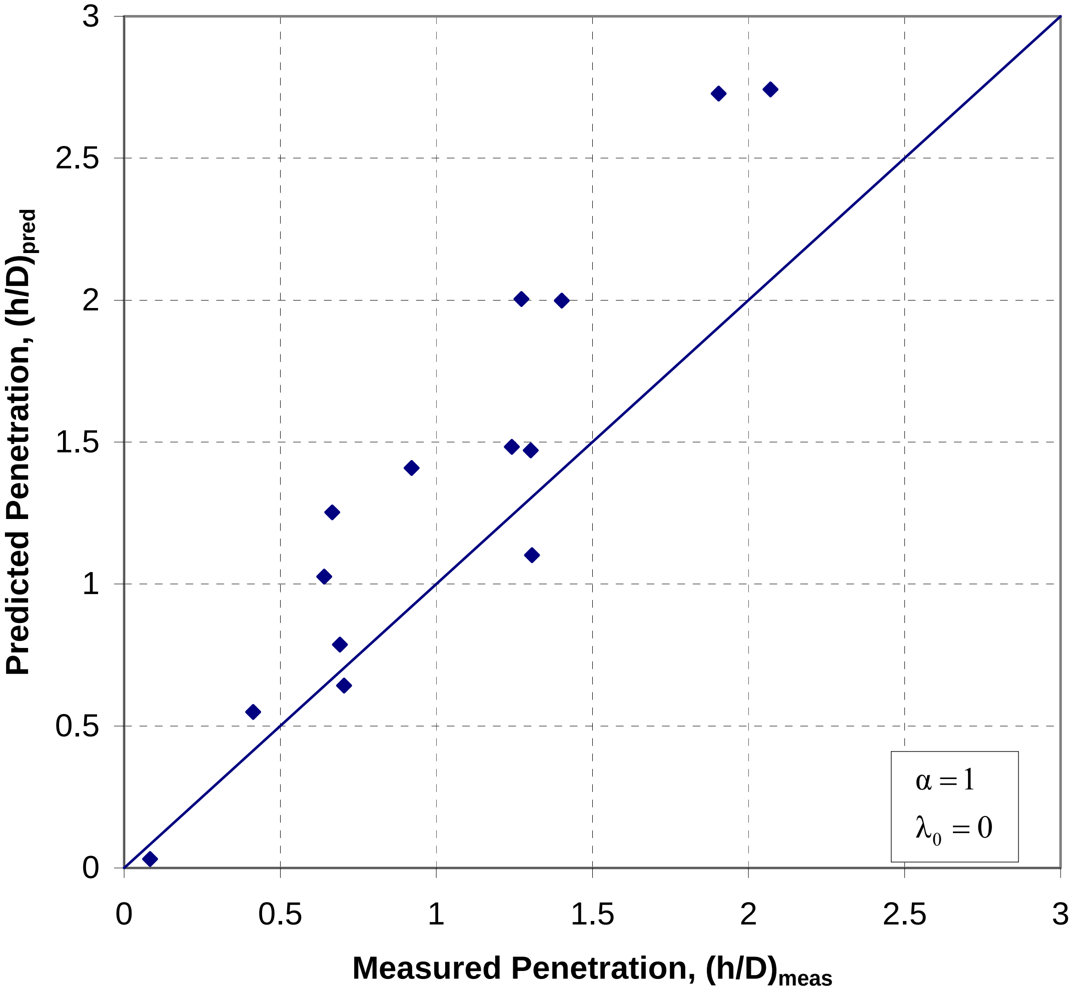

Figure 5.9 Predictions without Strain Rate Correction versus Measurements

5.2 XBP Interpretations

The XBP interpretation is a reverse process of the penetration studies. The soil strength is an input parameter for the penetration studies whereas it is the target parameter to be solved for the XBP studies. The XBP studies employed the same single particle model as illustrated by Eq. 5.1, while the soil strength is back-calculated from acceleration measurements in this case.

5.2.1 Algorithm for XBP Interpretation

Eq. 5.1 can be rewritten into the following form:

$$F_s / W = 1 - F_b / W - a / g \tag{5.15}$$

The buoyancy force of water for the XBP is 1.57 N. The soil buoyancy force is the soil unit weight multiplied by the volume displaced by the penetrometer. The volume is calculated as follows: before the XBP penetrates past the maximum section ($h/d < 1.2$), it is interpolated from the calculated volumes at a series of embedment depths as illustrated in Table 5.3; after the open trench forms ($h/d > 1.2$), the volume V in cm^3 is calculated by

$$V = 89.35 + A(h - 6.1) \tag{5.16}$$

The empirical soil resistance relationship may be established by combining Eqs. 3.23 and 4.7, which gives

If $h/d < 1.2$

$$F_s / c_0 A = 8.55(h/d)^{0.756}[1 + \lambda_0 \log_{10}(v / d\dot{\varepsilon}_0)] \tag{5.17a}$$

Table 5.3 Calculated Volume Displaced by the XBP (*h/d*<1.2)

Penetration (cm)	Volume (cm^3)
0	0
0.1	0.20
0.3	0.96
0.6	2.66
1.1	6.52
1.6	11.63
2.1	17.77
2.6	24.82
3.1	32.72
3.6	41.25
4.1	50.24
4.6	59.67
5.1	69.39
5.6	79.30
6.1	89.35

If $h/d > 1.2$

$$F_s / c_0 A = 9.60(h/d)^{0.210}[1+\lambda_0 \log_{10}(v/d\dot{\varepsilon}_0)] \tag{5.17b}$$

With the soil shearing resistance force and the buoyancy force characterized within the framework described above, estimation of the soil undrained shear strength profile from XBP data is possible through the following steps (Aubeny and Shi, 2005b):

1. The accelerometer provides a history of acceleration versus time $a(t)$ throughout the penetration process.
2. Invoking Eq. 5.15 permits a determination of the soil shearing resistance force F_s at each time step.

3. Acceleration is integrated to obtain a history of velocity v and embedment depth h throughout penetration.
4. Undrained shear strength c_0 corresponding to the reference strain rate $\dot{\varepsilon}_0$ is evaluated from Eqs. 5.17.

A MATLAB computer code implementing this algorithm entitled XBP_SOFTCLAY was developed for this research (Appendix E).

5.2.2 Field Measurements

Investigations by the Office of Naval Research on mine burial prediction have included XBP tests at offshore sites for which independent estimates of shallow seafloor sediment strengths are available. These data provided a valuable opportunity for an evaluation the proposed framework for XBP interpretation which is discussed below.

The field data under consideration involve two XBP drops at each of five test sites (designated Sites 4, 5, 12, 19, and 20) in the Gulf of Mexico near Corpus Christi, Texas, in water depths ranging from 20.4 to 43.0 m (Abelev, 2005). At each test site, one to two 2-m long by 8.9-cm diameter drop core samples were obtained for total density and laboratory miniature vane (MV) shear strength tests. Table 5.4 shows data provided by Valent (2003) relevant to the penetration depth range of the XBP's. Soil classification tests were not performed on the specific core samples associated with the test drops; however, laboratory tests on samples from nearby locations in the Corpus Christi test area typically classified the sediments as clays ranging from medium to high plasticity (CL, CH). Exact positions were not measured for the XBP tests and the drop core locations, with the distance between these locations at a given test being influence by local wind, current and tide conditions. Based on estimates by personnel conducting the investigations (Abelev, 2005), the drop core locations are likely within 20 to 100 m of the XBP test locations.

Table 5.4 Soil Properties at Corpus Christi Test Site (Aubeny and Shi, 2005b)

Site/Core	Depth (cm)	Wet Density* (g/cm^3)	MV Strength (kPa)
4/1	0-10	1.60	1.1
	10-20	1.76	2.7
	20-30	1.77	4.3
5/1	0-10	1.64	1.5
	10-20	1.75	3.1
	20-30	1.60	3.8
5/2	0-10	1.57	0.8
	10-20	1.82	2.1
	20-30	1.74	2.4
12/1	0-10	1.64	0.7
	10-20	1.76	1.7
	20-30	1.67	2.6
12/2	0-10	1.68	1.0
	10-20	1.79	1.9
	20-30	1.67	2.4
19/1	0-10	1.64	1.3
	10-20	1.74	2.1
	20-30	1.66	2.2
20/1	0-10	1.74	0.8
	10-20	1.90	1.7
	20-30	1.74	2.4

*From nuclear data-logger.

Figure 5.10 shows a typical deceleration and velocity profile from an XBP drop. The penetrometer impacted the seafloor at a velocity of 727 cm/sec. Decelerations increase almost linearly to a depth of 15 cm and then taper to a plateau of about 15*g* at a depth of 20 cm. An upward spike in the decelerations occurs between 23 and 24 cm depth. Similar spikes occur in other tests. The cause of their occurrence is not fully certain at present, but thin sand seams in the soil profile are a likely explanation.

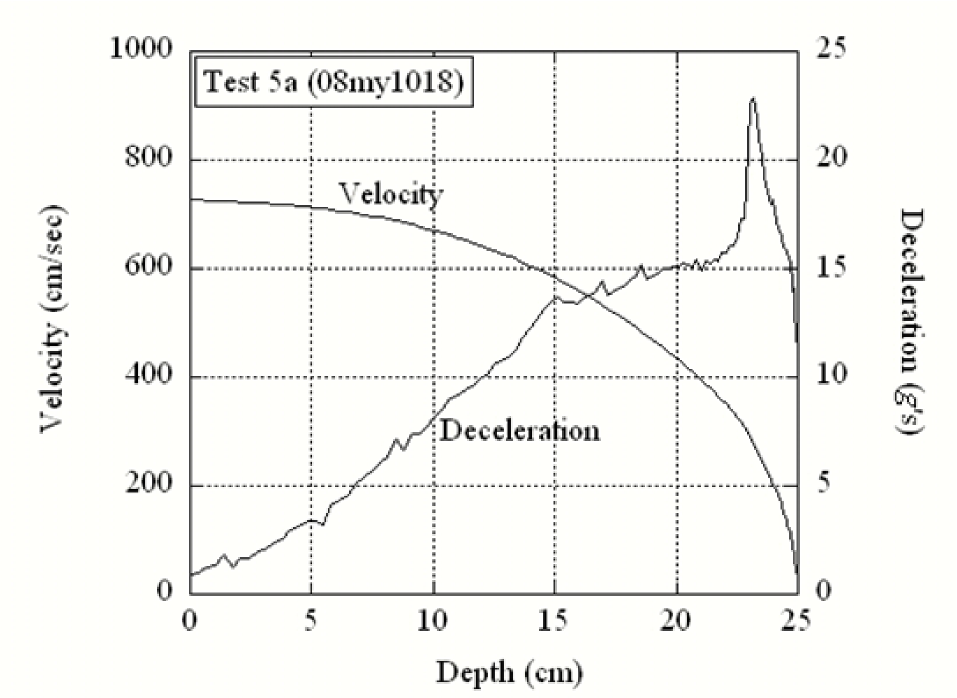

Figure 5.10 Typical Velocity and Deceleration Histories during XBP Penetration (Aubeny and Shi, 2005b)

5.2.3 Interpreted Undrained Shear Strength Profiles

Figures 5.11 through 5.15 show sediment strength profiles interpreted from the XBP drops. Penetration measurements were interpreted under assumptions of strain rate dependence ($\lambda_0 = 0.15$, $\dot{\varepsilon}_0 = 0.05\% / hr$) and rate-independence ($\lambda_0 = 0$). The same strain rate multiplier as in the penetration studies was used, because the previously noted MV tests conducted at variable rotation rates to estimate λ_0 were also performed on remolded soil samples from the Corpus Christi test area, although not on the specific core samples discussed herein. Superimposed on the plots are profiles of undrained shear strength from the miniature vane (MV) tests. To compensate for the relatively high strain rate levels in the MV tests, $\dot{\theta}$ = 77^{o}/min (80.6 radians/hr), the XBP c_0 strengths were scaled upward to a comparable strain rate level using Eq. 5.12 assuming $\dot{\theta} = \dot{\varepsilon}$. This assumption obviously involves some uncertainty, but it provides an objective basis for accounting for the strain rate effects associated with the five orders of magnitude difference between the rate of shearing in the MV test relative to the reference strain rate $\dot{\varepsilon}_0$ (Aubeny and Shi, 2005b).

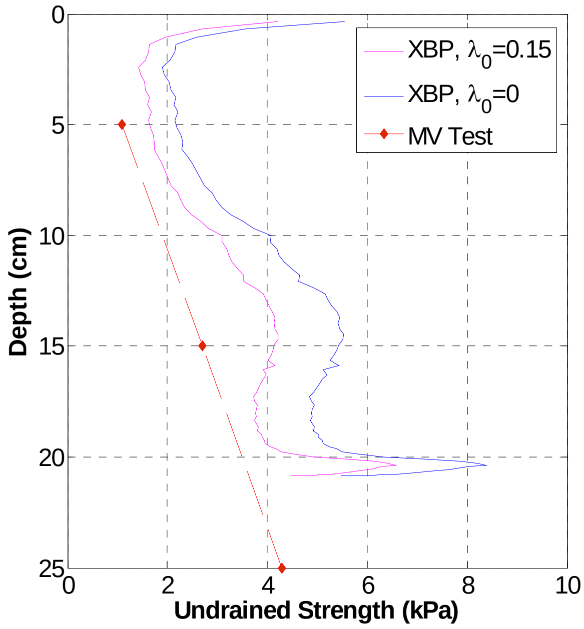
Test 4a (07my1508)

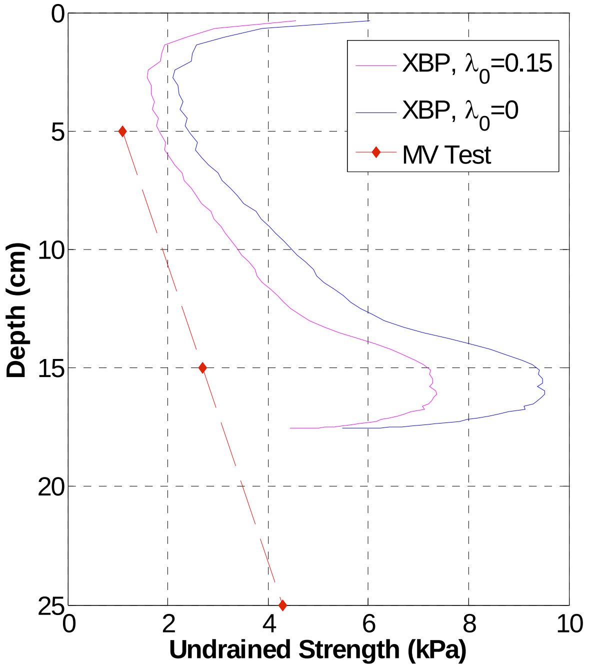
Test 4b (07my1510)

Figure 5.11 Interpreted XBP Strength Profile at Site 4

Test 5a (08my1018)

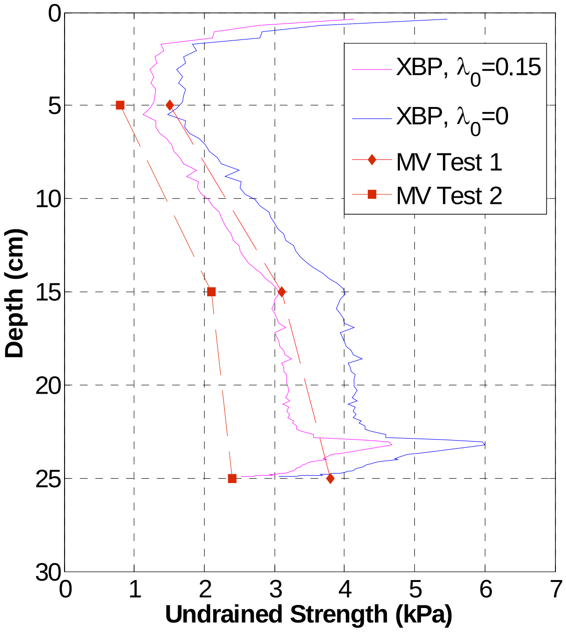

Test 5b (08my1020)

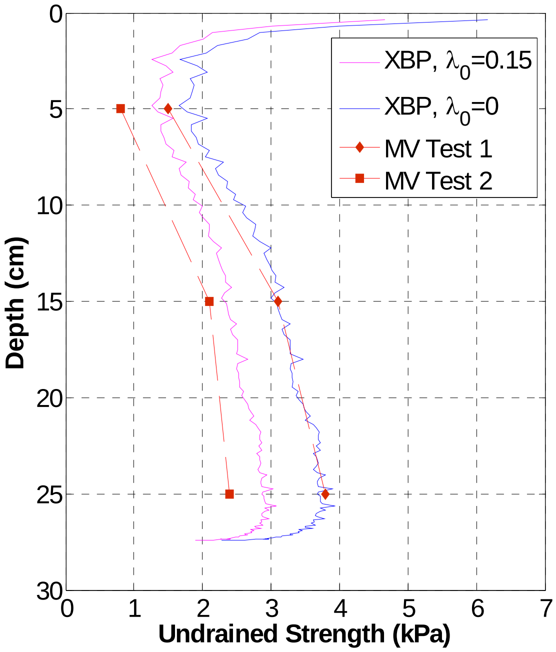

Figure 5.12 Interpreted XBP Strength Profile at Site 5

Test 12a (10my1353)

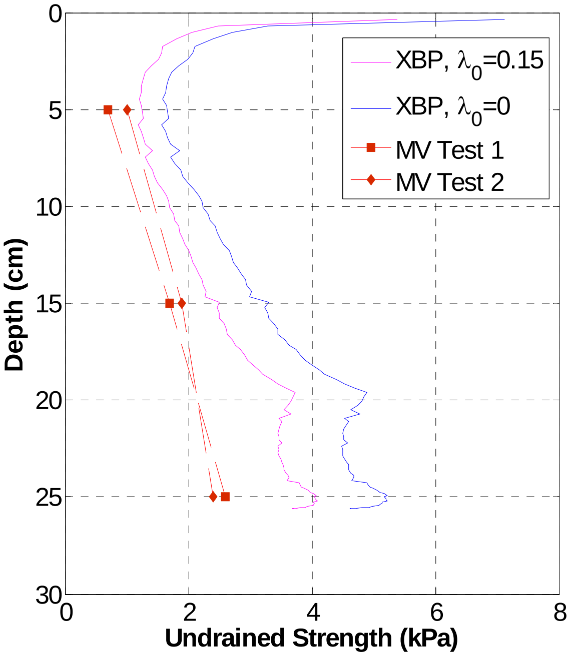

Test 12b (10my1354)

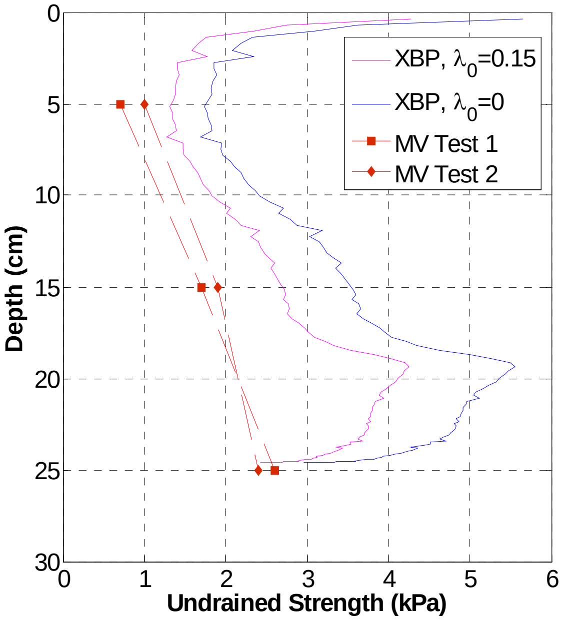

Figure 5.13 Interpreted XBP Strength Profile at Site 12

Test 19a (15my0929)

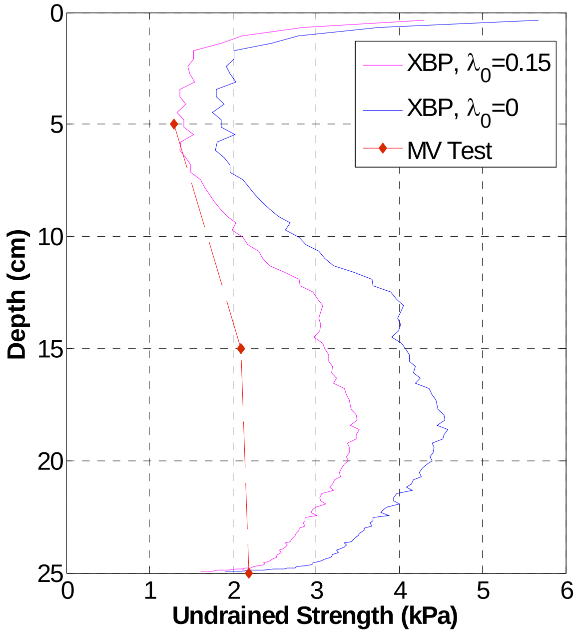

Test 19b (15my0933)

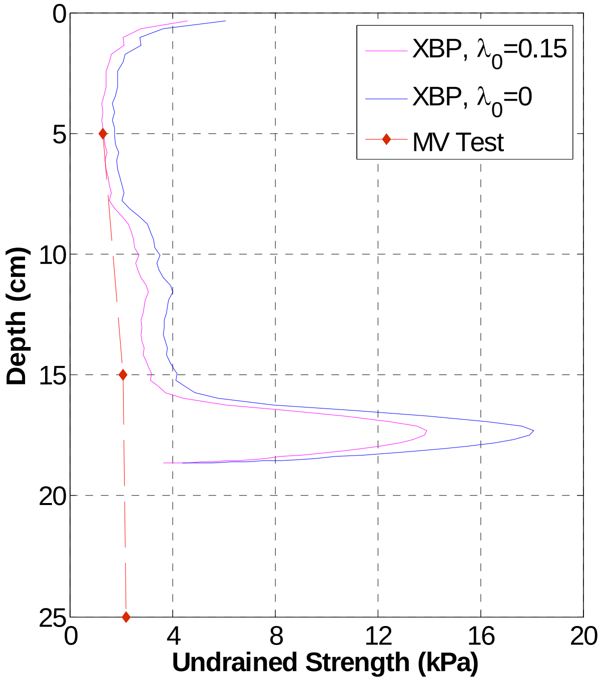

Figure 5.14 Interpreted XBP Strength Profile at Site 19

Test 20a (15my1452)

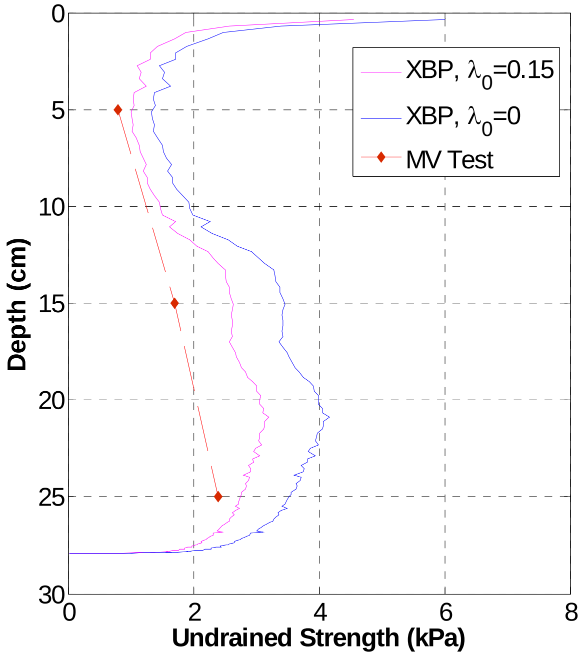

Test 20b (15my1453)

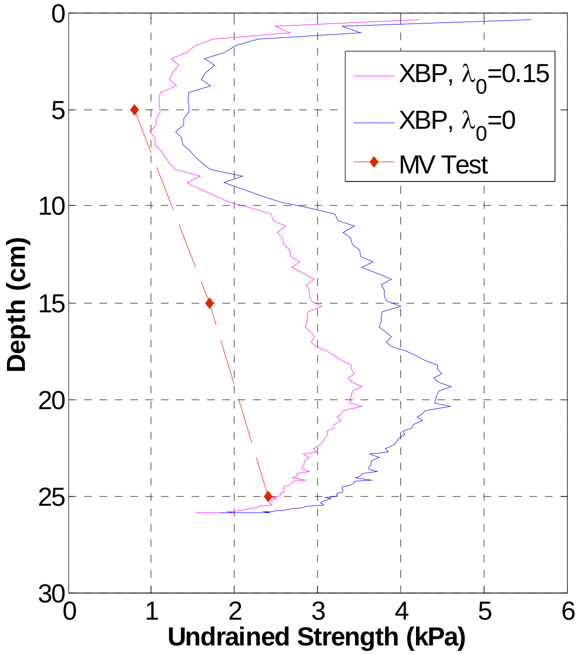

Figure 5.15 Interpreted XBP Strength Profile at Site 20

Examination of the interpreted XBP strength profiles vis-à-vis the MV strength profiles reveals two regions where the XBP strengths are consistently unrealistic (Aubeny and Shi, 2005b):

1. During the initial stages of penetration, the interpreted XBP strengths severely over-estimate the reference MV strengths in all cases. A possible source of this discrepancy is that this analysis does not account for the inertial resistance from the soil and the hydrodynamic resistance from the water column that may be significant during early stages of penetration. Neglecting resistance from this source can lead to over-estimates of the sediment shearing resistance. The depth of this initial phase of penetration for which valid XBP strength interpretations are considered unreliable is taken as the depth at which the apparent interpreted strength reaches a local minimum. Figures 5.11 through 5.15 indicate unreliable strength estimates from the XBP in the initial 5 cm ($h/d \approx 1$) of penetration.
2. The apparent XBP strength precipitously declines in the final stages of penetration. Elastic rebound of the soil as the penetration velocity declines to zero, an effect not considered in Eq. 5.1, is a probable source of this discrepancy.

Penetration measurements from intermediate depths between the initial and final phases of penetration described above appear to provide a valid basis for estimating sediment undrained shear strength. Comparisons between MV and interpreted XBP strengths within this range of depths indicate the following (Aubeny and Shi, 2005b):

1. The interpreted XBP strengths match reasonably well to the reference MV strength profile in Tests 4a, 5a, 5b, 12a, and 12b, 19a, 20a, and 20b. Considering that the MV tests are conducted at discrete 10 cm depth intervals and that they do not necessarily match the exact location where the XBP actually impacted the seafloor, the overall level of agreement is considered satisfactory.
2. The most serious deviations between MV reference strengths occur in Tests 4b (Figure 5.11) and 19b (Figure 5.14). In the case of Test 4b, the most severe mismatch occurs at a depth interval of 14 to 18 cm. In Test 19b, the XBP interpreted strength profile matches well with the reference MV profile between 5 and 15 cm. Below that depth, a large ‘spike’ occurs in the XBP profile, with the XBP strengths exceeding the MV strength by a factor of 6. The source of these spikes is at present uncertain. A plausible explanation under consideration is the possible existence of thin sandy seams in the soil profiles at these locations. The behavior of sands under dynamic loading appears to differ considerably from that of clays (Stoll et al., 2004) and will be discussed subsequently in this dissertation.
3. Overall, the XBP test interpretations that assume strain rate dependence (λ = 0.15) match the reference MV strength profiles better than those which assume rate independence. The strain rate independent interpretations generally overestimate the MV strength, resulting from neglect of strength increase at elevated strain rates.

4. The algorithm evaluates the soil shearing resistance force by Eqs. 5.17, which is based on the finite element result of a uniform strength and no slippage case. While the use of the result of a general strength profile seems to be more desirable, it will not necessarily generate better predictions. As with the cylinder studies, the normalized collapse loads for the general strength case would be lower than the uniform case, hence it will predict higher strengths. Yet from Figures 5.11 to 5.15 we can see that this will generally cause deviation from the measurements. This again may be viewed as the effect of compensation errors, i.e., neglecting the tendency of the soil to close into the void formed in the wake of the advancing penetrometer, the inertial resistance of soil and the hydrodynamic forces during penetration will tend to over-estimate the soil strength. The use of the results from the uniform strength case may have somewhat offset these errors and generated better predictions. Meanwhile, based on the penetration studies, the predictions with $\alpha = 1$ appear to be reasonable.

Comparison to the most recent and more extensive strength profiles at sites 4, 5, 12 and 19 from Naval Research Laboratory (data provided by Abelev and Valent, 2005) also indicates good agreement between interpreted XBP strength profiles and the MV strength profiles (Figures 5.16 through 5.19). The wide scatter of the MV strength measurements introduces some ambiguity in interpreting the results, but overall the XBP profiles match reasonably well with the measurements except the spike for Test 19b, which may be caused by thin sandy seams.

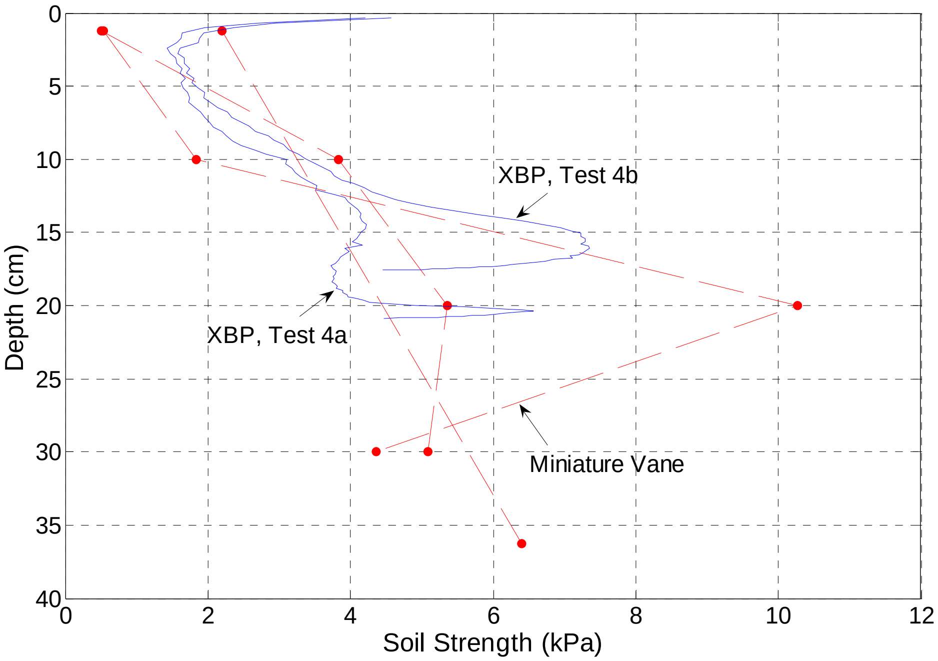

Figure 5.16 Comparison between XBP Strength Profiles and MV Strength Profiles at Site 4 (after Abelev and Valent, 2005)

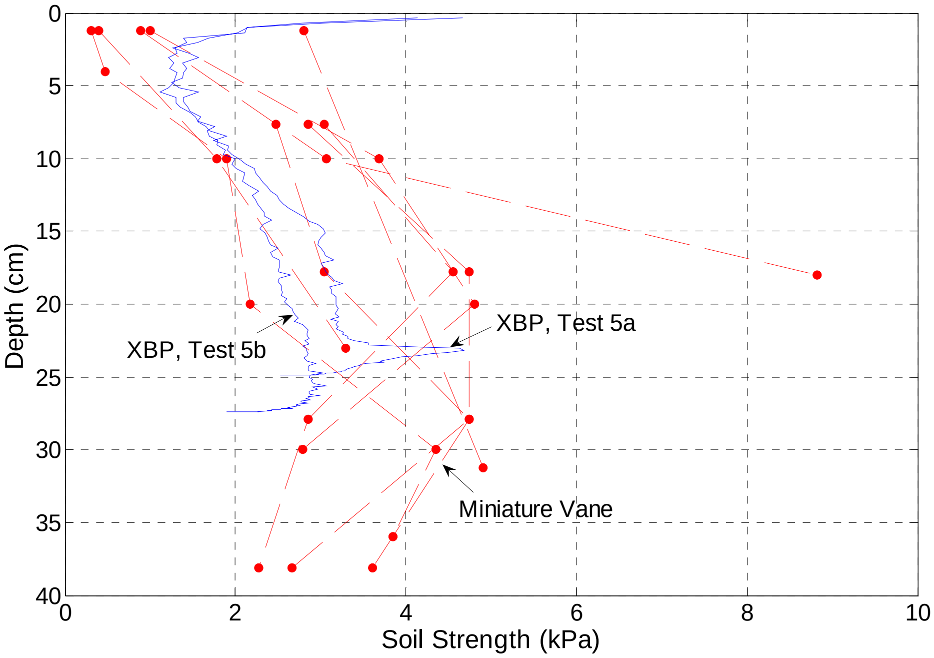

Figure 5.17 Comparison between XBP Strength Profiles and MV Strength Profiles at Site 5 (after Abelev and Valent, 2005)

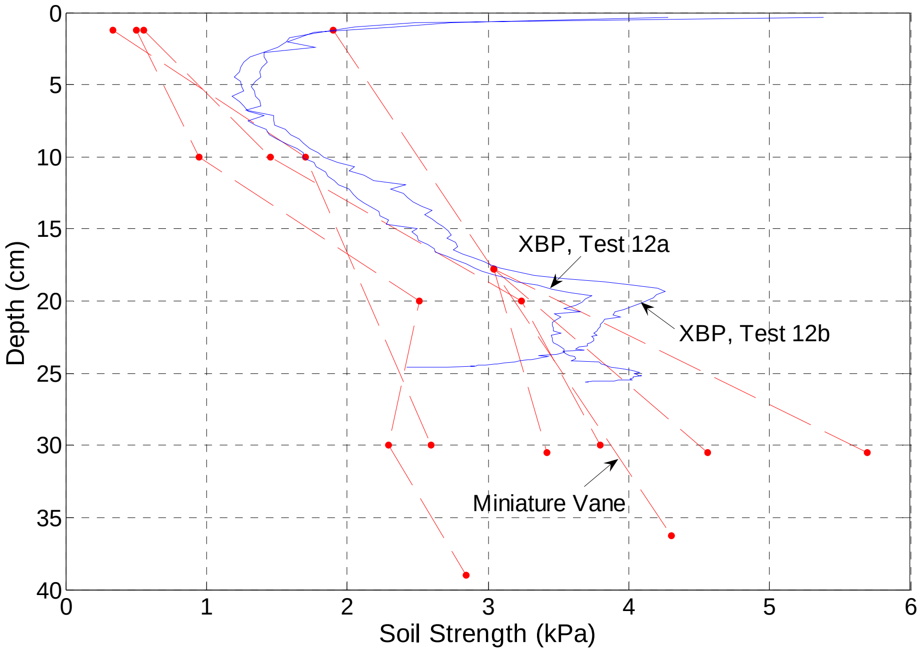

Figure 5.18 Comparison between XBP Strength Profiles and MV Strength Profiles at Site 12 (after Abelev and Valent, 2005)

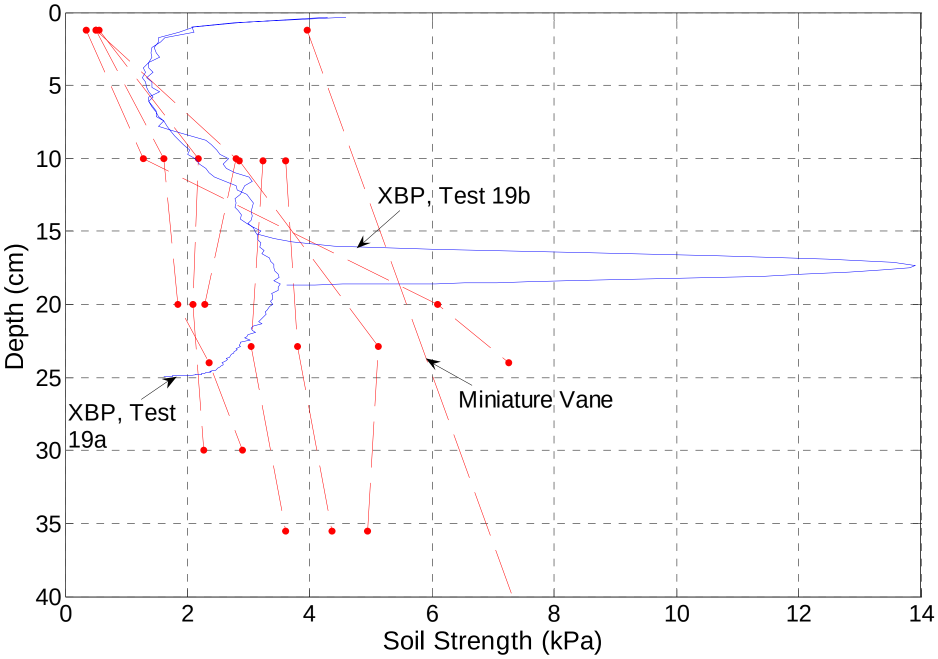

Figure 5.19 Comparison between XBP Strength Profiles and MV Strength Profiles at Site 19 (after Abelev and Valent, 2005)

As noted above, the existence of thin seams in the soil profiles has been postulated as a possible cause of the spikes in the interpreted XBP strength profiles. Indeed, these phenomena spurred an experimental study by Stoll et al. (2004) investigating the behavior of sands under impact loading using instrumented probes capable of measuring tip resistance and pore pressures during impact penetration. The Stoll study showed the rate sensitivity of sands to be much higher than that of the clays under consideration in this study, and conditions of partial drainage are also a likely critical factor. High negative pressures measured by the pore water pressure transducers suggested the tendency for dilation to be related to the apparent strain rate effects.

At present, it appears that more work is needed both to develop a theoretical framework and to acquire experimental data for analyzing impact penetration in sands. Accordingly, the framework presented herein for interpreting impact penetration measurements in soft clays should not be extended to sands until a number of questions relating to rate effects in sands have been resolved (Aubeny and Shi, 2005b).

CHAPTER VI

CONCLUSIONS AND RECOMMENDATIONS*

6.1 Conclusions

There are two aspects in this study: cylinder penetrations and XBP interpretations. For cylinder penetrations, this study first considers quasi-static collapse loads for a cylinder embedded in a purely cohesive soil mass. At embedments greater than one-half diameter, a vertical trench is assumed to exist above the cylinder. The finite element and plasticity collapse load calculations show the following (Aubeny et al., 2005):

1. For cylinder embedments less than one-half diameter, $h/D < 0.5$, computed finite element collapse loads are bracketed by the upper and lower bound estimates from plasticity theory (Figures 3.15 and 3.16), thus supporting the validity of the finite element estimates. At shallow embedments, $h/D < 0.3$, the lower bound MOC collapse load estimates are virtually in full agreement with the finite element estimates.
2. For cylinder embedments less than one-half diameter, $h/D < 0.5$, in a uniform soil, two velocity fields for upper bound solutions are applied to partially embedded cylinders, one based on the solution of Randolph and Houlsby (1984) for a fully embedded translating cylinder, and one based on the consistent solution of Murff et al. (1989) for a partially embedded cylinder.

---

* Part of this chapter is reprinted with permission of ASCE from “Collapse loads for a cylinder embedded in trench in cohesive soil.” by C. P. Aubeny, H. Shi and J. D. Murff, 2005, *International Journal of Geomechanics*, ASCE, scheduled to be published in the 2005.

Both solutions (Figure 3.15) provide reasonable estimates of collapse loads, although the Murff et al. (1989) consistent solution gives somewhat better overall agreement with finite element estimates. Application of either the Randolph-Houlsby or the Murff et al. velocity fields to non-uniform soil strength conditions (Figure 3.16) provides reasonable upper bound collapse load estimates in the embedment range $0.3 \leq h / D \leq 0.5$ for the smooth case. At shallower embedments, the disparity between these upper bound estimates and both finite element and lower bound MOC solutions becomes increasingly severe.

3. For cylinder embedments greater than one-half diameter, $h/D > 0.5$, extension of the Randolph-Houlsby velocity field to the side wall of the trench and the ground surface (Figure 3.4), while providing valid upper bound solutions, tends to substantially over-estimate the finite element collapse load estimates (Figures 3.17 and 3.18).
4. Collapse loads normalized by the soil strength at the bottom of the cylinder, c_h, are relatively insensitive to strength gradients η. Figure 3.19 shows the maximum variation in predicted collapse loads due to variation in η is on the order of 10%.

The study then evaluates the strain rate effects on the collapse loads for a penetrating cylinder through rate-dependent finite element analyses. A predictive model for the penetration depth of cylinders was developed subsequently based on a single particle model. The findings suggest the following (Aubeny and Shi, 2005a):

1. If the soil strength c increases semi-logarithmically with strain rate (Eq. 4.1), the total shearing resistance F_s will, to a reasonable degree of accuracy, increase in a proportionate manner (Eq. 4.3). Specifically, if ρ_0 is the semi-logarithmic strain rate multiplier for soil strength, then $\lambda_0 \cong \rho_0$ is a reasonably accurate estimate of the strain rate multiplier for the total soil shearing resistance force acting on the cylinder.
2. The approximate power law equations defined by Eq. 3.22 in conjunction with the approximate approach to accounting for strain rate effects (Conclusion 1 and Eq. 4.3) provide realistic estimates of the total soil shearing resistance to penetration of a horizontal cylinder for variable conditions of velocity v and penetration depth h.
3. Realistic estimates of penetration require a proper accounting of strain rate effects.
4. The rate-dependent plasticity framework utilized in this study requires an estimate of a threshold strain rate, below which soil shear strength remains constant. Limited data are available on this issue, so estimates of this value entail considerable uncertainty. For the range of conditions considered in this study, penetration predictions were not sensitive to the magnitude of the threshold strain rate; however, this observation will not necessarily hold under all conditions.

The XBP studies were conducted within a framework similar to that of the cylinder studies. The interpretation is achieved by back-calculating soil strength from impact penetration measurements in soft clays. The development and evaluation of a framework for relating impact penetration measurements to soil strength lead to the following conclusions (Aubeny and Shi, 2005b):

1. The highly variable velocity conditions associated with impact penetration dictate a somewhat different approach to test interpretation than is usually adopted for constant penetration rate tests. In a constant penetration rate test, it is reasonable to adopt a single strain rate correction factor relating soil strength under conditions of penetration to soil strength under other conditions of interest. However, conditions of variable velocity dictate a variable strain rate correction (Eq. 4.7) throughout the penetration process.
2. The continuously varying conditions of embedment during XBP penetration similarly dictate continuous updating of the penetrometer tip resistance related to soil strength (Eqs. 3.23).
3. Acceleration measurements provide an attractive approach to estimating strength from impact penetration measurements. In addition to being the fundamental variable that can be related to soil shearing resistance (Eq. 5.15), acceleration measurements can be integrated to obtain velocity data for characterizing rate effects (Eq. 4.7) and depth data for characterizing embedment effects (Eqs. 3.23).
4. Sediment strength interpreted from XBP measurements agrees reasonably well with MV shear strength values performed on nearby core samples. Occasional anomalous spikes in the XBP strength profiles cannot be fully

explained at present, but sand seams in the soil profiles are a suspected cause of this phenomenon.

6.2 Recommendations

The following recommendations can be made for future study (Aubeny and Shi, 2005a):

1. This study assumes a vertical trench is formed in the wake of the advancing object. In reality the soil will tend to cave in at a certain depth. Therefore, to which depth this assumption is valid remains an issue to be resolved.
2. The lack of data on the threshold strain rate for very soft normally consolidated soils is a particular obstacle to using the proposed model with confidence. It might be noted that if the threshold strain rate is extremely low, a viscous fluid model could be a preferable model for soil shearing resistance.
3. Much experimental data indicate that the simple semi-logarithmic equation (Eq. 4.1) relating shear strength to strain rate is not strictly valid over a large range of strain rates. Accordingly, a need exists for more data and possibly more comprehensive models.
4. The strength of very soft soils usually cannot be measured directly in tests having uniform strain and strain rate conditions; i.e., intrusive test methods (e.g., vane shear, T-bar, cone penetration) are required. Inferring rate-dependent soil properties from tests involving non-uniform strain rates at

present involves considerable ambiguity, pointing to a research need for improved interpretation of intrusive tests in rate-dependent materials.

5. Further study on the interpretation of the “hard layer effects”, particularly study on the impact penetration in sands is needed.
6. Although only two geometries (the cylinder and the XBP) were considered in this research, the methodology described in this study is likely to be feasible for other geometries, e.g., the spherical penetrometer (Randolph et al., 2000) etc.
7. Further study taking into account the large strain aspects of the problem may be considered. The Shallow Strain Path Method (SSPM) proposed by Sagaseta et al. (1995) combines the Strain Path Method (SPM; Baligh 1985) with the consideration of the influence of the free surface for shallow penetration problems by means of image sources and sinks. A strain path finite element method as described by Teh and Houlsby (1988) may also be incorporated.
8. Extend study of cylinder penetration to inclined cylinders rotating at some angular velocity.

REFERENCES

Aas, G. (1965). “Study of the effect of vane shape and rate of strain on measured values of in situ shear strength of clays,” *Proceedings, 6th International Conference on Soil Mechanics and Foundation Engineering,* Montreal, I, 141-145.

Abelev, A. (2005). Personal communication, Naval Research Laboratory, Stennis Space Center, Mississippi.

Abelev, A. and Valent P. (2005). Personal communication, Naval Research Laboratory, Stennis Space Center, Mississippi.

Alberro, J., and Santoyo, E. (1973). “Long term behavior of Mexico City clay.” *Proc., 8th International Conference on Soil Mechanics and Foundation Engineering,* 1, 1-9.

ASTM (2001). “Standard test method for laboratory miniature vane shear test for saturated fine-grained clayey soil.” *Annual Book of ASTM Standards*, Vol. 04.08, American Society for Testing and Matererials, Philadelphia, 810-815.

Aubeny, C.P. (2003). *Advanced numerical methods class notes*. Department of Civil Engineering, Texas A&M University, College Station, Texas.

Aubeny, C.P, and Dunlap, W.A. (2003). “Penetration of cylindrical objects in soft mud.” *Proc., Oceans 2003*, San Diego, 4, 2068-2073.

Aubeny, C.P. and Shi, H. (2005a). “Effect of rate-dependent soil strength on cylinders penetrating into soft clay.” Submitted for publication in *IEEE Journal of Oceanic Engineering, Special Issue: Predicting Burial on the Littoral Seafloor*.

Aubeny, C.P. and Shi, H. (2005b). “Interpretation of impact penetration measurements in soft clays.” Submitted for publication in *Journal of Geotechnical and Geoenvironmental Engineering*, ASCE.

Aubeny, C.P., Shi, H. and Murff, J.D. (2005). “Collapse loads for a cylinder embedded in trench in cohesive soil.” *International Journal of Geomechanics*, ASCE, scheduled to be published in the 2005.

Baligh, M.M. (1985). “Strain path method.” *Journal of Geotechnical Engineering*, ASCE, 111(9), 1108-1136.

Berre, T., and Bjerrum, L. (1973). "Shear strength of normally consolidated clays." *Proc., 8th International Conference on Soil Mechanics and Foundation Engineering,* 1, 39-49.

Biscontin, G., and Pestana, J.M. (2001). "Influence of peripherial velocity on vane shear strength of an artificial clay." *ASTM. Geotechnical Testing Journal*, 24(4), 423-429.

Bjerrum, L., Simons, N., and Toblaa, I. (1958). "The effect of time on the shear strength of a soft marine clay." *Proc., Conference on Earth Pressure Problems,* 1, 148-158.

Bridge, C., Laver, K., Clukey, E., and Evans, T. (2004). "Steel catenary riser touchdown point vertical interaction models." *Offshore Technology Conference*, Houston, OTC 16628.

Cadling, L., and Odenstad, S. (1950). "The vane borer: an apparatus for determining the shear strength of clay soils directly in the ground." *Royal Swedish Geotechnical Institute, Proceedings,* 2, 1-87.

Calladine, C.R. (1969). *Engineering plasticity,* Pergamon Press, Oxford.

Casagrande, A., and Wilson, S.D. (1951). "Effect of rate of loading on the strength of clays and shales at constant water content." *Geotechnique*, 2(3), 251-263.

Chen, W.F. (1975). *Limit analysis and soil plasticity,* Elsevier, New York.

Chu, P.C., Evans, A., Gilles, A., Smith, T., and Taber, V. (2004). "Development of the Navy's 3D Mine Impact Burial Prediction Model (IMPACT35)." *Journal of Counter-Ordnance Technology*, *6th International Symposium on Technology and Mine Problem.*

Davis E.H., and Booker, J.R. (1973). "The effect of increasing strength with depth on the bearing capacity of clays." *Geotechnique*, 23(4), 551-563.

Drucker, D.C. and Prager, W. (1952). "Soil mechanics and plastic analysis or limit design." *Quarterly of Applied Mathematics*, 10, 157-165.

Ghazzaly, O.I. and Lim, S.T. (1975). "Experimental investigation of pipeline stability in very soft clays." *Offshore Technology Conference,* OTC 2277, 315-326.

Halwachs, J.E. (1972). "Analysis of sediment shear strength at varying rates of shear." *Trident Scholar Project Report, TSPR 28*, United States Naval Academy.

Hight, D. W. (1983). "Laboratory investigations of sea bed clays." PhD thesis, Imperial College, London, U.K.

HKS (2003). *ABAQUS Version 6.4 User's Manuals*. Hibbitt, Karlson and Sorensen, Inc.

Ladd, C.C., Williams, C.E., Connell, D.H., and Edgers, L. (1972). "Engineering properties of soft foundation clays at two south Louisiana levee sites." *Research Report No. R72-26,* Massachusetts Institute of Technology, Cambridge, Massachusetts.

Lefebvre, G., and LeBoeuf, D. (1987). "Rate effects and cyclic loading of sensitive clays." *Journal of Geotechnical Engineering.,* ASCE, 113(5), 476-489.

Martin (2001). "Vertical bearing capacity of skirted circular foundations on Tresca soil." *15th International Conference on Soil Mechanics and Geotechnical Engineering*, Istanbul, International Society for Soil Mechanics and Geotechnical Engineering, 743-746.

Munim, M. (2003). "Experimental investigation of mine penetration in soft sediments." MS thesis, Department of Civil Engineering, Texas A&M University, College Station, Texas.

Murff, J.D. (1978). "Upper bound analysis of incompressible, anisotropic media." *Proc., 15th Annual Meeting of the Society of Engineering Science*, 521-526.

Murff, J.D. (1980). "Vane shear testing of anisotropic, cohesive soils." *International Journal for Numerical and Analytical Methods in Geomechanics*, 4, 285-289.

Murff, J.D. (2002). *Geo-mechanics class notes*. Department of Civil Engineering, Texas A&M University, College Station, Texas.

Murff, J.D. (2003). *Advanced numerical methods class notes*. Department of Civil Engineering, Texas A&M University, College Station, Texas.

Murff, J.D., Wagner, D.A., and Randolph, M.F. (1989). "Pipe penetration in cohesive soil." *Geotechnique*, 39(2), 213-229.

Perlow, M., and Richards, A.F. (1977). "Influence of shear velocity on vane shear strength." *Journal of the Geotechnical Engineering Division*, ASCE, 103(GT1), 19-32.

Randolph, M.F., and Houlsby, G.T. (1984). "The limiting pressure on a circular pile loaded laterally in cohesive soil." *Geotechnique*, 34(4), 613-623.

Randolph, M.F., Martin, C.M. and Hu, Y. (2000). "Limiting resistance of a spherical penetrometer in cohesive material." *Geotechnique*, 50(5), 573-582.

Reddy, J.N. (1993). *An introduction to the finite element method*, McGraw-Hill, New York.

Richardson, A.M. (1963). “The relationship of the effective stress-strain behavior of a saturated clay to the rate of strain.” ScD thesis, Massachusetts Institute of Technology, Cambridge, Massachusetts.

Richardson, A.M., and Whitman, R.V. (1963). “Effect of strain-rate upon undrained shear resistance of a saturated remoulded fat clay.” *Geotechnique,* 13(4), 310-324.

Roy, M., and LeBlanc, A. (1988). “The in-situ measurement of the undrained shear strength of clays using the field vane.” *Vane Shear Strength Testing in Soils: Field and Laboratory Studies, ASTM STP 1014*, A.F. Richards, Ed., Philadelphia, 117-128.

Sagaseta, C., Whittle, A., and Santagata, M. (1995). “Deformation analysis of shallow penetration in saturated clay.” *Research Report R94-09*, Massachusetts Institute of Technology, Cambridge, Massachusetts.

Schapery, R.A., and Dunlap, W.A. (1978). “Prediction of storm-induced sea bottom movement and platform forces.” *Offshore Technology Conference*, Houston, OTC 3259.

Schapery, R.A. and Dunlap, W.A. (1984). “Theoretical and experimental investigation of mud forces on offshore pipelines.” *Report No. RF4534-1*, Texas A&M University, College Station, Texas.

Sharifounnasab, M., and Ullrich, R.C. (1985). “Rate of shear effects on vane shear strength.” *Journal of Geotechnical Engineering,* ASCE, 111(1), 135-139.

Sheahan, T.C., Ladd, C.C., and Germaine, J.T. (1996). “Rate-dependent undrained shear strength behavior of saturated clay.” *Journal of Geotechnical Engineering*, ASCE,122(2), 99-108.

Skempton, A.W. (1948). “Vane tests in the alluvial plain of the river forth near Grangemouth.” *Geotechnique,* 1(2), 111-124.

Small, S.W., Tambuvello, R. D., and Piaseckyj, P. J. (1971). “Submarine pipeline support by marine sediments.” *Offshore Technology Conference*, Houston, OTC 1357, 309-318.

Smith, A.D., and Richards, A.F. (1975). “Vane shear strength at two high rotation rates,” *Proc., Civil Engineering in the Oceans III,* Newark, Delaware, Vol. I, 421-433.

Sokolovskii, V.V. (1965). *Statics of granular media*, Pergamon Press, Oxford.

Stoll, R.D., Sun, Y.F. and Bitte, I. (2004). *Measuring Sea Bed Properties Using Static and Dynamic Penetrometers*, Lamont-Doherty Earth Observatory of Columbia University, New York.

Teh, C.I., and Houlsby, G.T. (1988). “Analysis of the cone penetration test by the strain path method.” *Proc., 6th International Conference on Numerical and Analytical Methods in Geo-mechanics*, Innsbruck, 2, 1443-1448.

Terzaghi, K. (1943). *Theoretical soil mechanics*, Wiley, New York.

Torstensson, B.A. (1977). “Time-dependent effects in the field vane test.” *International Symposium on Soft Clay*, Bangkok, 387-397.

Vaid, Y.P., and Campanella, R.G. (1977). “Time-dependent behavior of undisturbed clay.” *Journal of the Geotechnical Engineering Division*, ASCE, 103(7), 693-709.

Valent, P. (2003). Personal communication, Naval Research Laboratory, Stennis Space Center, Mississippi.

Whitney, M.J., and Rodin, G.J. (2001). “Force-velocity relationships for rigid bodies translating through unbounded shear-thinning power-law fluids.” *International Journal of Non-Linear Mechanics*, 36, 947-953.

Wiesel, C.E. (1973). “Some factors influencing in-situ vane tests results.” *Proc., 8th International Conference on Soil Mechanics and Foundation Engineering,* Moscow, Vol. 1.2, 475-479.

Willis, N.R.T. and West, P.T.J. (2001). “Interaction between deepwater catenary risers and a soft seabed: large scale sea trials.” *Offshore Technology Conference*, Houston, OTC 13113.

Yao, Z. (2003). “Numerical simulations of mine penetration in soft sediments.” MS thesis, Department of Civil Engineering., Texas A&M University, College Station, Texas.

APPENDIX A

MATLAB PROGRAM: MOC_CYLINDER

```
% MOC collapse load solution for smooth pipe penetration problem
%(penetration less than one radius) with linearly increasing strength.
%  xa,ya,xb,yb,xc,yc: coordinates; aa,ab,ac: angles between principal
%stress and x coordinate; fa,fb,fc: mean stresses; suaa,subb,succ etc.:
%shear strength.

clear;
p=input('Enter the depth of penetration, h/r: ');
eta=input('Enter the strength ratio(-1 for infinity): ');
incr=input('Enter the increment size at the free surface: ');
m=input('Enter number of increments divided across the fan: ');
r=1;
omega=asin(1-p/r);
if eta==-1
    su0=0;
    su1=1;
else
    su0=1;
    su1=eta*su0/2/r;
end

% Degenerate alpha characteristics
aa(1,1)=0;
xa(1,1)=r*cos(omega);
ya(1,1)=0;
suaa(1,1)=su0;
fa(1,1)=su0;
for i=2:m+1
     xa(1,i)=r*cos(omega);
     ya(1,i)=0;
     aa(1,i)=aa(1,i-1)+omega/m;
     suaa(1,i)=su0;
     fa(1,i)=fa(1,i-1)+2*suaa(1,i)*omega/m;
end

% k: number of alpha characteristics
for k=1:400
     temp3=k;
     xb(k,1)=r*cos(omega)+k*incr;
     yb(k,1)=0;
     ab(k,1)=0;
     fb(k,1)=su0;
     subb(k,1)=su0;

% j: number of beta characteristics
for j=1:m-1+2*k
     temp=1;
     tca(k,1)=tan((aa(k,j)/2+aa(k,j)/2+pi/4));
     tcb(k,1)=tan((ab(k,j)/2+ab(k,j)/2-pi/4));
     xc(k,1)=(yb(k,j)-ya(k,j)+xa(k,j)*tca(k,1)-xb(k,j)*tcb(k,1))/...
         (tca(k,1)-tcb(k,1));
     yc(k,1)=(yb(k,j)+ya(k,j)+(xc(k,1)-xb(k,j))*tcb(k,1)+(xc(k,1)-...
         xa(k,j))*tca(k,1))/2;
```

```
     succ(k,1)=su0+yc(k,1)*su1;
     suca(k,1)=(succ(k,1)+suaa(k,j))/2;
     sucb(k,1)=(succ(k,1)+subb(k,j))/2;
     ac(k,1)=(fa(k,j)-fb(k,j)+2*sucb(k,1)*ab(k,j)+2*suca(k,1)*...
         aa(k,j)+su1*(2*xc(k,1)-xa(k,j)-xb(k,j)))/(2*suca(k,1)...
         +2*sucb(k,1));

% Recycle
for i=1:99
     temp=temp+1;
     tca(k,i+1)=tan(aa(k,j)/2+ac(k,i)/2+pi/4);
     tcb(k,i+1)=tan(ab(k,j)/2+ac(k,i)/2-pi/4);
     xc(k,i+1)=(yb(k,j)-ya(k,j)+xa(k,j)*tca(k,i+1)-xb(k,j)*...
         tcb(k,i+1))/(tca(k,i+1)-tcb(k,i+1));
     yc(k,i+1)=(yb(k,j)+ya(k,j)+(xc(k,i+1)-xb(k,j))*tcb(k,i+1)+...
         (xc(k,i+1)-xa(k,j))*tca(k,i+1))/2;
     succ(k,i+1)=su0+yc(k,i+1)*su1;
     suca(k,i+1)=(succ(k,i+1)+suaa(k,j))/2;
     sucb(k,i+1)=(succ(k,i+1)+subb(k,j))/2;
     ac(k,i+1)=(fa(k,j)-fb(k,j)+2*sucb(k,i+1)*ab(k,j)+2*...
         suca(k,i+1)*aa(k,j)+su1*(2*xc(k,i+1)-xa(k,j)-xb(k,j)))/...
         (2*suca(k,i+1)+2*sucb(k,i+1));
     if abs(ac(k,i)-ac(k,i+1))<0.000001
        break;
     elseif i==99
        disp('Not converged')
     end
end

% Progress to the next step on alpha characterstics
fc(k,j)=(fa(k,j)+fb(k,j)+2*sucb(k,temp)*(ac(k,temp)-ab(k,j))-...
    2*suca(k,temp)*(ac(k,temp)-aa(k,j))+su1*(xb(k,j)-xa(k,j)))/2;
xb(k,j+1)=xc(k,temp);
yb(k,j+1)=yc(k,temp);
ab(k,j+1)=ac(k,temp);
fb(k,j+1)=fc(k,j);
subb(k,j+1)=succ(k,temp);
temp4=j;
end

% Boundary condition
temp2(k)=temp4+1;
aaa=0;
bbb=p-.00000001;
faa=fff(aaa,xb(k,temp2(k)),yb(k,temp2(k)),ab(k,temp2(k)),r,p);
fbb=fff(bbb,xb(k,temp2(k)),yb(k,temp2(k)),ab(k,temp2(k)),r,p);
if faa*fbb>0
    yb(k,temp2(k)+1)=p;
    xb(k,temp2(k)+1)=0;
    ab(k,temp2(k)+1)=pi/2;
    subb(k,temp2(k)+1)=su0+su1*yb(k,temp2(k)+1);
    fb(k,temp2(k)+1)=fb(k,temp2(k))+2*(subb(k,temp2(k))/2+...
        subb(k,temp2(k)+1)/2)*(ab(k,temp2(k)+1)-ab(k,temp2(k)))...
```

```
        -su1*(xb(k,temp2(k)+1)-xb(k,temp2(k)));
    ff(k)=fb(k,temp2(k)+1)+subb(k,temp2(k)+1);
    hold on;
    plot(xb(k,:),-yb(k,:));
    break;
end
cc=(aaa+bbb)/2;
fcc=fff(cc,xb(k,temp2(k)),yb(k,temp2(k)),ab(k,temp2(k)),r,p);
while abs(fcc)>=.000001
    if fcc*faa<0
        bbb=cc;
        cc=(aaa+bbb)/2;
        fcc=fff(cc,xb(k,temp2(k)),yb(k,temp2(k)),ab(k,temp2(k)),r,p);
        fbb=fff(bbb,xb(k,temp2(k)),yb(k,temp2(k)),ab(k,temp2(k)),r,p);
    elseif fcc*fbb<0
        aaa=cc;
        cc=(bbb+aaa)/2;
        fcc=fff(cc,xb(k,temp2(k)),yb(k,temp2(k)),ab(k,temp2(k)),r,p);
        faa=fff(aaa,xb(k,temp2(k)),yb(k,temp2(k)),ab(k,temp2(k)),r,p);
    else
        disp('Bottom of cylinder not reached');
        break;
    end
end
yb(k,temp2(k)+1)=cc;
xb(k,temp2(k)+1)=sqrt(r*r-(cc+r-p)^2);
ab(k,temp2(k)+1)=atan((cc+r-p)/xb(k,temp2(k)+1));
subb(k,temp2(k)+1)=su0+su1*yb(k,temp2(k)+1);
fb(k,temp2(k)+1)=fb(k,temp2(k))+2*(subb(k,temp2(k))/2+...
    subb(k,temp2(k)+1)/2)*(ab(k,temp2(k)+1)-ab(k,temp2(k)))-...
    su1*(xb(k,temp2(k)+1)-xb(k,temp2(k)));
ff(k)=fb(k,temp2(k)+1)+subb(k,temp2(k)+1);

% Plot alpha characteristics
figure(1)
hold on;
axis equal;
plot(xb(k,:),-yb(k,:))

% Progress to the next alpha characteristics
for j=1:temp2(k)+1
     xa(k+1,j)=xb(k,j);
     ya(k+1,j)=yb(k,j);
     aa(k+1,j)=ab(k,j);
     fa(k+1,j)=fb(k,j);
     suaa(k+1,j)=subb(k,j);
end
end

% Calculate collapse load
f1=ff(1)*sin(ab(1,temp2(1)+1))*r*(ab(1,temp2(1)+1)-aa(1,21));
for i=1:temp3-1
     f1=f1+ff(i+1)*sin(ab(i+1,temp2(i+1)+1))*...
```

```
         (ab(i+1,temp2(i+1)+1)-ab(i,temp2(i)+1));
end
f2=fa(1,21)*sin(aa(1,21))*r*(ab(1,temp2(1)+1)-aa(1,21));
for i=1:temp3-1
     f2=f2+ff(i)*sin(ab(i,temp2(i)+1))*(ab(i+1,temp2(i+1)+1)-...
         ab(i,temp2(i)+1));
end
f=(f1+f2)/2;

% Normalize by the soil strength at the bottom of cylinder
cavg=su0+su1*p;
disp(' ');
disp('Normalized collapse load');
fv=2*f/2/r/cavg

% Plot beta characteristics
for k=1:temp3-1
    for j=1:temp2(k)+1
         xx(1)=xb(k,j);
         yy(1)=yb(k,j);
         xx(2)=xb(k+1,j+1);
         yy(2)=yb(k+1,j+1);
         figure(1)
         hold on;
         plot(xx,-yy);
    end
end
xs(1)=xa(1,1);
ys(1)=ya(1,1);
xs(2)=xb(1,2);
ys(2)=yb(1,2);
figure(1)
hold on;
plot(xs,-ys);

% Plot cylinder
yp=linspace(-p,2-p,100);
for i=1:100
     xp(i)=sqrt(r*r-(yp(i)-r+p)^2);
end
figure(1);
hold on;
axis equal;
plot(xp,yp);

% Plot free surface
x00=sqrt(r*r-(r-p)^2);
xh=linspace(x00,2.8,100);
yh(1:100)=0;
figure(1)
hold on;
plot(xh,yh)
axis([0,2.8,-2,2]);
```

```
function[f]=fff(y,xc,yc,ac,r,p)
x=sqrt(r*r-(y+r-p)^2);
af=atan((y+r-p)/x);
f=yc+(x-xc)*tan((atan((y+r-p)/x)+ac)/2-pi/4)-y;
```

APPENDIX B

MATLAB PROGRAM: RH_CYLINDER

```
%  Program  for  modified  Randolph-Houlsby  upperbound  for  cylinder
%penetration with linearly increasing strength

clear;

% Input data
p=input('Enter the depth of penetration, h/r: ');
eta=input('Enter the strength ratio(-1 for infinity): ');
delta=input('Enter the adhesion angle(0~pi/2): ');
%note: enter pi/2-0.000001 for pi/2 to avoid singularity
r0=1;
ksai=pi/4-delta/2;
v0=1;
if eta==-1
    su0=0;
    su1=1;
else
    su0=1;
    su1=eta*su0/2/r0;
end
if p>r0
    omega=0;
else
    omega=asin((r0-p)/r0);
end

% Interface AF
if p<=r0
   a1=r0*cos(delta/2)-r0*sin(omega);
   b1=r0*cos(delta/2)-r0*sin(omega)+r0*sin(delta/2);
elseif p>r0
   a1=p-r0+r0*cos(delta/2);
   b1=p-r0+r0*cos(delta/2)+r0*sin(delta/2);
end
w(1)=su0*v0*(b1-a1)+su1*v0*(b1*b1-a1*a1)/2;

% Interface ABC
w(2)=intABC(ksai,v0,r0,su0,su1,delta,omega,pi/2-delta/2,p,omega);

% Interface CDE
rr1=r0*(sqrt(2)*sin(delta/2)+(pi/2-delta/2-omega)*cos(ksai));
if p<=r0
   w(3)=v0*su0/sqrt(2)*rr1*(delta/2+omega+pi/4)+...
       su1*rr1*rr1*v0/sqrt(2)*(1-cos(pi/4+delta/2+omega));
else
    w(3)=v0*su0/sqrt(2)*rr1*(delta/2+omega+pi/4)+su1*(p-r0)*...
        v0/sqrt(2)*rr1*(delta/2+omega+pi/4)+su1*rr1*rr1*v0/...
        sqrt(2)*(1-cos(pi/4+delta/2+omega));
end

% Interface FGH
w(4)=intFGH(ksai,v0,r0,su0,su1,delta,omega,pi/2-delta/2,p,omega);
```

```
% Interface HIJ
rr2=r0*(pi/2-delta/2-omega)*cos(ksai);
vt=v0*cos(delta/2)/cos(ksai)-v0/sqrt(2);
if p<=r0
   w(5)=vt*su0*rr2*(delta/2+omega+pi/4)+su1*rr2*rr2*vt*...
       (1-cos(pi/4+delta/2+omega));
else
    w(5)=vt*su0*rr2*(delta/2+omega+pi/4)+vt*su1*(p-r0)*rr2*...
        (delta/2+omega+pi/4)+su1*rr2*rr2*vt*(1-...
        cos(pi/4+delta/2+omega));
end

% Interface FKQ
w(6)=int1(ksai,v0,r0,su0,su1,delta,omega,pi/2-delta/2,p,omega);

% Region ABCHGF
w(7)=dblint1(ksai,v0,r0,su0,su1,omega,pi/2-delta/2,delta,p,omega);

% Region CDEJIH
r3=r0*(pi/2-delta/2-omega)*cos(ksai);
r4=r0*(sqrt(2)*sin(delta/2)+(pi/2-delta/2-omega)*cos(ksai));
w(8)=dblint4(ksai,v0,r0,su0,su1,0,pi/4+delta/2+omega,r3,r4,p,1);

% Region FGHQK
w(9)=dblint2(ksai,v0,r0,su0,su1,omega,pi/2-delta/2,p,omega);

% Region HIJQ
w(10)=dblint3(ksai,v0,r0,su0,su1,omega,pi/2-delta/2,0,pi/4+...
    delta/2+omega,omega,p,1);

if (p>r0&p<=r3+r0)
% Region EOMJ
beta1=asin((p-r0)/r4);
w(11)=dblint4(ksai,v0,r0,su0,su1,0,beta1,r3,r4,p,2);

% Region OMN
beta2=asin((p-r0)/r3);
w(12)=dblint5(ksai,v0,r0,su0,su1,beta1,beta2,delta,omega,p);

% Region JNQ
w(13)=dblint3(ksai,v0,r0,su0,su1,omega,pi/2-delta/2,0,beta2,omega,p,2);

% Region NQP
w(14)=dblint6(ksai,v0,r0,su0,su1,beta2,pi/2,omega,p);

% Interface EO
r23=r0*(sqrt(2)*sin(delta/2)+(pi/2-delta/2-omega)*cos(ksai));
w(15)=(su0+su1*(p-r0))*v0/sqrt(2)*r23*beta1+su1*r23*r23*v0/...
    sqrt(2)*(cos(beta1)-1);
```

```
% Interface JMN
r15=r0*(pi/2-delta/2-omega)*cos(ksai);
w(16)=(su0+su1*(p-r0))*vt*r15*beta2+su1*r15*r15*vt*(cos(beta2)-1);

elseif (p>r3+r0&p<r4+r0)
% Region EOMJ
beta1=asin((p-r0)/r4);
w(11)=dblint4(ksai,v0,r0,su0,su1,0,beta1,r3,r4,p,2);

% Region OMN
w(12)=dblint5(ksai,v0,r0,su0,su1,beta1,pi/2,delta,omega,p);

% Region JNQ
w(13)=dblint3(ksai,v0,r0,su0,su1,omega,pi/2-delta/2,0,pi/2,omega,p,2);

% Interface EO
r23=r0*(sqrt(2)*sin(delta/2)+(pi/2-delta/2-omega)*cos(ksai));
w(14)=(su0+su1*(p-r0))*v0/sqrt(2)*r23*beta1+su1*r23*r23*v0/...
    sqrt(2)*(cos(beta1)-1);

% Interface JMN
r15=r0*(pi/2-delta/2-omega)*cos(ksai);
w(15)=(su0+su1*(p-r0))*vt*r15*pi/2+su1*r15*r15*vt*(cos(pi/2)-1);

elseif p>=r4+r0
% Region EOMJ
w(11)=dblint4(ksai,v0,r0,su0,su1,0,pi/2,r3,r4,p,2);

% Region JNQ
w(12)=dblint3(ksai,v0,r0,su0,su1,omega,pi/2-delta/2,0,pi/2,omega,p,2);

% Interface EO
r23=r0*(sqrt(2)*sin(delta/2)+(pi/2-delta/2-omega)*cos(ksai));
w(13)=(su0+su1*(p-r0))*v0/sqrt(2)*r23*pi/2+su1*r23*r23*v0/...
    sqrt(2)*(cos(pi/2)-1);

% Interface JMN
r15=r0*(pi/2-delta/2-omega)*cos(ksai);
w(14)=(su0+su1*(p-r0))*vt*r15*pi/2+su1*r15*r15*vt*(cos(pi/2)-1);
end

% Calculate collapse load
fv=2*sum(w(:))/v0;
cp=su0+su1*p;
disp(' ');
disp('Normalized collapse load: ');
fv=fv/2/r0/cp
```

```
% Integration function for interface ABC
function[sum2]=intABC(ksai,v0,r0,su0,su1,delta,a,b,p,omega)
sum2=0;
xsum=0;
d=(b-a)/100;
for theta2=a:d:b
    xsum=xsum+1;
    if p<=r0
        z=r0*sin(theta2)-r0*sin(omega)+cos(theta2-omega)*(r0*...
            sqrt(2)*sin(delta/2)+r0*(pi/2-delta/2-theta2)*cos(ksai));
    elseif p>r0
        z=p-r0+r0*sin(theta2)+cos(theta2-omega)*(r0*sqrt(2)*...
            sin(delta/2)+r0*(pi/2-delta/2-theta2)*cos(ksai));
    end
    c2=su0+su1*z;
    v2=v0/sqrt(2);
    w(xsum)=c2*v0/sqrt(2)*r0*(sqrt(2)*sin(delta/2)+sin(ksai)+...
        (pi/2-delta/2-theta2)*cos(ksai));
end
for i=1:xsum
    sum2=sum2+w(i)*d;
end
sum2=sum2-w(1)*d/2-w(xsum)*d/2;
```

```
% Integration function for interface FGH
function[sum2]=intFGH(ksai,v0,r0,su0,su1,delta,a,b,p,omega)
sum2=0;
xsum=0;
d=(b-a)/100;
for theta2=a:d:b
    xsum=xsum+1;
    if p<=r0
        z=r0*sin(theta2)-r0*sin(omega)+cos(theta2-omega)*r0*...
            (pi/2-delta/2-theta2)*cos(ksai);
    elseif p>r0
        z=p-r0+r0*sin(theta2)+cos(theta2-omega)*r0*(pi/2-...
            delta/2-theta2)*cos(ksai);
    end
    c3=su0+su1*z;
    vt=v0*cos(delta/2)/cos(ksai)-v0/sqrt(2);
    w(xsum)=c3*vt*r0*(sin(ksai)+(pi/2-delta/2-theta2)*cos(ksai));
end
for i=1:xsum
    sum2=sum2+w(i)*d;
end
sum2=sum2-w(1)*d/2-w(xsum)*d/2;
```

```
% Integration function for region FKQ
function[sum2]=int1(ksai,v0,r0,su0,su1,delta,a,b,p,omega)
sum2=0;
xsum=0;
d=(b-a)/100;
for theta1=a:d:b
    xsum=xsum+1;
    if p<=r0
       z=r0*sin(theta1)-r0*sin(omega);
    elseif p>r0
       z=r0*sin(theta1)+p-r0;
    end
    c3=su0+su1*z;
    v3=v0*(cos(theta1)+sin(theta1)*tan(ksai));
    w(xsum)=c3*sin(delta)*v3*r0;
end
for i=1:xsum
    sum2=sum2+w(i)*d;
end
sum2=sum2-w(1)*d/2-w(xsum)*d/2;
```

```
% Integration function for region ABCHGF
function[sum2]=dblint1(ksai,v0,r0,su0,su1,a,b,delta,p,omega)
xsum=0;
sum2=0;
d1=(b-a)/100;
for theta2=a:d1:b
    xsum=xsum+1;
    ysum=0;
    c=r0*(sin(ksai)+(pi/2-delta/2-theta2)*cos(ksai));
    d=r0*(sqrt(2)*sin(delta/2)+sin(ksai)+(pi/2-delta/2-theta2)...
        *cos(ksai));
    d2=(d-c)/100;
    if c==d
       for ysum=1:101
           w(xsum,ysum)=0;
       end
    else
    for r=c:d2:d
        ysum=ysum+1;
        if p<=r0
            z=r0*sin(theta2)-r0*sin(omega)+(r-r0*sin(ksai))...
                *cos(theta2-ksai);
        elseif p>r0
            z=p-r0+r0*sin(theta2)+(r-r0*sin(ksai))*cos(theta2-ksai);
        end
        c4=su0+su1*z;
        g1=v0/r/sqrt(2);
        w(xsum,ysum)=c4*v0/r/sqrt(2)*r;
    end
    end
end
for i=1:xsum
    sum1(i)=0;
    for j=1:ysum
        sum1(i)=sum1(i)+w(i,j)*d2;
    end
    sum1(i)=sum1(i)-w(i,1)*d2/2-w(i,ysum)*d2/2;
    sum2=sum2+sum1(i)*d1;
end
sum2=sum2-sum1(1)*d1/2-sum1(xsum)*d1/2;
```

```
% Integration function for region FGHQK
function[sum2]=dblint2(ksai,v0,r0,su0,su1,a,b,p,omega)
xsum=0;
sum2=0;
d1=(b-a)/100;
for theta1=a:d1:b
    xsum=xsum+1;
    ysum(xsum)=0;
    for theta2=a:d1:theta1
        ysum(xsum)=ysum(xsum)+1;
        rr=r0*(sin(ksai)+(theta1-theta2)*cos(ksai));
        if p<=r0
            z=r0*sin(theta2)-r0*sin(omega)+(rr-r0*sin(ksai))...
                *cos(theta2-ksai);
        elseif p>r0
            z=r0*sin(theta2)+p-r0+(rr-r0*sin(ksai))*cos(theta2-ksai);
        end
        c5=su0+su1*z;
        g2=v0*sin(theta1)/rr/cos(ksai)-v0*cos(theta1)/r0/...
            cos(ksai)/cos(ksai);
        w(xsum,ysum(xsum))=abs(c5*g2*rr*r0*cos(ksai));
    end
end
for i=1:xsum
    sum1(i)=0;
    for j=1:ysum(i)
        sum1(i)=sum1(i)+w(i,j)*d1;
    end
    sum1(i)=sum1(i)-w(i,1)*d1/2-w(i,ysum(i))*d1/2;
    sum2=sum2+sum1(i)*d1;
end
sum2=sum2-sum1(1)*d1/2-sum1(xsum)*d1/2;
```

```
% Integration function for region HIJQ and JNQ
function[sum2]=dblint3(ksai,v0,r0,su0,su1,a,b,c,d,omega,p,flg)
xsum=0;
sum2=0;
if (a==b|c==d)
    sum2=0;
else
d1=(b-a-.000001)/100;
for theta1=a+.000001:d1:b
    xsum=xsum+1;
    ysum=0;
    d2=(d-c)/100;
    for theta3=c:d2:d
        ysum=ysum+1;
        r=r0*(theta1-omega)*cos(ksai);
        if flg==1
        if p<=r0
            z=r*sin(theta3);
        elseif p>r0
            z=p-r0+r*sin(theta3);
        end
        elseif flg==2
            z=p-r0-r*sin(theta3);
        end
        c6=su0+su1*z;
        g3=v0*sin(theta1)/r/cos(ksai)-v0*cos(theta1)/r0/...
            cos(ksai)/cos(ksai);
        w(xsum,ysum)=c6*g3*r*r0*cos(ksai);
    end
end
for i=1:xsum
    sum1(i)=0;
    for j=1:ysum
        sum1(i)=sum1(i)+w(i,j)*d2;
    end
    sum1(i)=sum1(i)-w(i,1)*d2/2-w(i,ysum)*d2/2;
    sum2=sum2+sum1(i)*d1;
end
sum2=sum2-sum1(1)*d1/2-sum1(xsum)*d1/2;
end
```

```
% Integration function for region CDEJIH and EOMJ
function[sum2]=dblint4(ksai,v0,r0,su0,su1,a,b,c,d,p,flag)
xsum=0;
sum2=0;
d1=(b-a)/100;
if (a==b|c==d)
    sum2=0;
else
for theta3=a:d1:b
    xsum=xsum+1;
    ysum=0;
    d2=(d-c)/100;
    for r=c:d2:d
        ysum=ysum+1;
    if flag==1
        if p<=r0
           z=r*sin(theta3);
        elseif p>r0
           z=p-r0+r*sin(theta3);
        end
    elseif flag==2
       z=p-r0-r*sin(theta3);
    end
        c4=su0+su1*z;
        g1=v0/r/sqrt(2);
        w(xsum,ysum)=c4*v0/r/sqrt(2)*r;
    end
end
for i=1:xsum
    sum1(i)=0;
    for j=1:ysum
        sum1(i)=sum1(i)+w(i,j)*d2;
    end
    sum1(i)=sum1(i)-w(i,1)*d2/2-w(i,ysum)*d2/2;
    sum2=sum2+sum1(i)*d1;
end
sum2=sum2-sum1(1)*d1/2-sum1(xsum)*d1/2;
end
```

```
% Integration function for region OMN
function[sum2]=dblint5(ksai,v0,r0,su0,su1,a,b,delta,omega,p)
xsum=0;
sum2=0;
sum1(1:101)=0;
d1=(b-a)/100;
if a==b
    sum2=0;
else
for theta3=a:d1:b
    c=r0*(pi/2-delta/2-omega)*cos(ksai);
    d=(p-r0)/sin(theta3);
    d2=(d-c)/100;
    if c==d
        break;
    end
    xsum=xsum+1;
    ysum=0;
    for r=c:d2:d
        ysum=ysum+1;
        z=p-r0-r*sin(theta3);
        c4=su0+su1*z;
        g1=v0/r/sqrt(2);
        w(xsum,ysum)=c4*v0/r/sqrt(2)*r;
        sum1(xsum)=sum1(xsum)+w(xsum,ysum)*d2;
    end
    sum1(xsum)=sum1(xsum)-w(xsum,1)*d2/2-w(xsum,ysum)*d2/2;
    sum2=sum2+sum1(xsum)*d1;
end
sum2=sum2-sum1(1)*d1/2-sum1(xsum)*d1/2;
end
```

```
% Integration function for region NQP
function[sum2]=dblint6(ksai,v0,r0,su0,su1,a,b,omega,p)
xsum=0;
sum2=0;
sum1(1:101)=0;
d1=(b-a)/100;
for theta3=a:d1:b
    xsum=xsum+1;
    ysum=0;
    c=0;
    d=(p-r0)/sin(theta3);
    d2=(d-c)/100;
    for r=c+.000001:d2:d
        ysum=ysum+1;
        theta1=r/r0/cos(ksai);
        z=p-r0-r*sin(theta3);
        c6=su0+su1*z;
        g3=v0*sin(theta1)/r/cos(ksai)-v0*cos(theta1)/r0/...
            cos(ksai)/cos(ksai);
        w(xsum,ysum)=c6*g3*r;
        sum1(xsum)=sum1(xsum)+w(xsum,ysum)*d2;
    end
    sum1(xsum)=sum1(xsum)-w(xsum,1)*d2/2-w(xsum,ysum)*d2/2;
    sum2=sum2+sum1(xsum)*d1;
end
sum2=sum2-sum1(1)*d1/2-sum1(xsum)*d1/2;
```

APPENDIX C

MATLAB PROGRAM: CU_CYLINDER*

---

* Functions are the same as defined in Appendix B.

```
% Program for modified consistent upperbound for cylinder penetration
%with linearly increasing strength

clear;

% Input data
p=input('Enter the depth of penetration, h/r: ');
eta=input('Enter the strength ratio(-1 for infinity): ');
delta=input('Enter the adhesion angle(0~pi/2): ');
%note: enter pi/2-0.000001 for pi/2 to avoid singularity
r0=1;
ksai=pi/4-delta/2;
omega=asin((r0-p)/r0);
v0=1;
if eta==-1
    su0=0;
    su1=1;
else
    su0=1;
    su1=eta*su0/2/r0;
end

% Interface AF
a1=r0*cos(delta/2)-r0*sin(omega);
b1=r0*cos(delta/2)-r0*sin(omega)+r0*sin(delta/2);
w(1)=su0*v0*(b1-a1)+su1*v0*(b1*b1-a1*a1)/2;

% Interface ABC
w(2)=intABC(ksai,v0,r0,su0,su1,delta,omega,pi/2-delta/2,p,omega);

% Interface CD
rr1=r0*(sqrt(2)*sin(delta/2)+(pi/2-delta/2-omega)*cos(ksai));
w(3)=v0*su0/sqrt(2)*rr1*(delta/2+omega)+su1*rr1*rr1*v0/sqrt(2)*...
    (sqrt(2)/2-cos(pi/4+delta/2+omega));

% Interface DE
w(4)=v0/sqrt(2)*su0*rr1+v0*su1*rr1*rr1/4;

% Interface FGH
w(5)=intFGH(ksai,v0,r0,su0,su1,delta,omega,pi/2-delta/2,p,omega);

% Interface HI
rr2=r0*(pi/2-delta/2-omega)*cos(ksai);
vt=v0*cos(delta/2)/cos(ksai)-v0/sqrt(2);
w(6)=vt*su0*rr2*(delta/2+omega)+su1*rr2*rr2*vt*(sqrt(2)/2-...
    cos(pi/4+delta/2+omega));

% Interface IJ
w(7)=su0*vt*rr2+su1*vt*sqrt(2)*rr2*rr2/4;

% Interface FKQ
w(8)=int1(ksai,v0,r0,su0,su1,delta,omega,pi/2-delta/2,p,omega);
```

```
% Region ABCHGF
w(9)=dblint1(ksai,v0,r0,su0,su1,omega,pi/2-delta/2,delta,p,omega);

% Region CDIH
r3=r0*(pi/2-delta/2-omega)*cos(ksai);
r4=r0*(sqrt(2)*sin(delta/2)+(pi/2-delta/2-omega)*cos(ksai));
w(10)=dblint4(ksai,v0,r0,su0,su1,pi/4,pi/4+delta/2+omega,r3,r4,p,1);

% Region FGHQK
w(11)=dblint2(ksai,v0,r0,su0,su1,omega,pi/2-delta/2,p,omega);

% Region HIQ
w(12)=dblint3(ksai,v0,r0,su0,su1,omega,pi/2-delta/2,pi/4,pi/4+...
    delta/2+omega,omega,p,1);

% Region IJQ
w(13)=v0*su0*r0*(sin(delta/2)+(pi/2-delta/2-omega)*cos(delta/2)-...
    cos(omega))+sqrt(2)/4*v0*su1*r0*r0*cos(ksai)*(rr2*rr2*...
    sin(rr2)-2*sin(rr2)+2*rr2*cos(rr2)-2*omega*cos(rr2)-...
    2*omega*rr2*sin(rr2)+omega^2*sin(rr2)+2*omega);

% Calculate collapse load
fv=2*sum(w(:))/v0;
cp=su0+su1*p;
disp(' ');
disp('Normalized collapse load: ');
fv=fv/2/r0/cp

.
```

APPENDIX D

MATLAB PROGRAM: MINE_BURIAL

```
% Accounts for:
%               buoyancy
%               variable soil strengh profile
%               strain rate effects
%               soil-cylinder adhesion
%               open trench
clear all
% Inputs
srr=input('Enter soil resistance ratio   ');
v0=input('Enter impact velocity ratio   ');
gamma=input('Enter soil unit weight ratio   ');
epsref=input('Enter reference normalized strain rate     ');
lambda=input('Enter strain rate multiplier     ');
dt=input('Enter dimensionless time increment   ');
alpha=input('Enter adhesion factor  ');
eta=input('Enter strength ratio(-1 for infinity)  ');

% Initialize
h=0;
v=v0;
% For loop for penetration process
for i=1:1000000
    if eta==0
    if alpha==0
        if h<=0.5
           fs=srr*10^0.7341*h^0.2881;
       else
           fs=srr*10^0.7122*h^0.2077;
       end
    elseif alpha==1
        if h<=0.5
           fs=srr*10^0.87*h^0.3703;
       else
           fs=srr*10^0.802*h^0.1551;
       end
    else
        if h<=0.5
           fs=srr*10^0.7341*h^0.2881+alpha*(srr*10^0.87*h^0.3703-...
               srr*10^0.7341*h^0.2881);
       else
           fs=srr*10^0.7122*h^0.2077+alpha*(srr*10^0.802*h^0.1551-...
               srr*10^0.7122*h^0.2077);
       end
    end
    elseif eta==-1
      if alpha==0
          if h<=0.5
             fs=srr*10^0.6478*h^1.1707;
         else
             fs=srr*10^0.6649*h^1.2086;
         end
      elseif alpha==1
          if h<=0.5
```

```
             fs=srr*10^0.7797*h^1.2042;
         else
             fs=srr*10^0.7745*h^1.1527;
         end
      else
          if h<=0.5
             fs=srr*10^0.6478*h^1.1707+alpha*(srr*10^0.7797*h^1.2042...
                 -srr*10^0.6478*h^1.1707);
         else
             fs=srr*10^0.6649*h^1.2086+alpha*(srr*10^0.7745*h^1.1527...
                 -srr*10^0.6649*h^1.2086);
         end
      end
    else
      if alpha==0
          if h<=0.5
             fs=srr*10^0.6962*h^0.235*(1+eta*h);
         else
             fs=srr*10^0.6885*h^0.2081*(1+eta*h);
         end
      elseif alpha==1
          if h<=0.5
             fs=srr*10^0.8282*h^0.2914*(1+eta*h);
         else
             fs=srr*10^0.7883*h^0.1539*(1+eta*h);
         end
      else
          if h<=0.5
             fs=srr*10^0.6962*h^0.235*(1+eta*h)+alpha*(srr*10^0.8282...
                 *h^0.2914*(1+eta*h)-srr*10^0.6962*h^0.235*(1+eta*h));
         else
             fs=srr*10^0.6885*h^0.2081*(1+eta*h)+alpha*(srr*...
                 10^0.7883*h^0.1539*(1+eta*h)-srr*10^0.6885*...
                 h^0.2081*(1+eta*h));
         end
      end
    end
    if h<0.5
        fb=gamma*(.25*acos(1-2*h)-(.5-h)*sqrt(h-h^2));
    end
    if h>=0.5
        fb=gamma*(pi/8+h-.5);
    end
% Strain rate correction
    if v<=epsref
        src=1;
    else
        src=1+lambda*log10(v/epsref);
    end;
    fs=fs*src;
% Acceleration (assumed constant in time increment)
a=1-fs-fb;
% Velocity at end of time increment
ve=v+a*dt;
```

```
% Check for zero velocity
if ve<=0
    dt=-v/a;
    vavg=v/2;
    hmax=h+vavg*dt
    break;
end
% Average velocity in time increment
vavg=(v+ve)/2;
% Update velocity and penetration
v=ve;
h=h+vavg*dt;
end

% Inputs:
%Soil resistance ratio= c*A/W for uniform case (eta=0), A=projected
%                       mine area, W=mine weight, c=soil strength
%                     = c1*d*A/W for linear increasing strength case
%                       (eta=Inf.). c1=strength gradient, c0=soil
%                       strength at ground surface, d=mine diameter
%                     = c0*A/W for general stength profile (0<eta<Inf.)
%Impact velocity ratio= v0/(g*d)^1/2, v0=impact velocity
%                       g=gravitational acceleration
%Soil unit weight ratio= gamma*A*d/W, gamma=soil unit weight
%Threshold normalized strain rate= e0/sqrt(g/d), e0=threshold strain
%                                  rate
%Strain rate multiplier
%Dimensionless time increment (recommended: 0.001)
%Adhesion factor = 0~1
%Strength ratio = c1*d/c0
```

APPENDIX E

MATLAB PROGRAM: XBP_SOFTCLAY

```
% XBP Interpretation
% Units: kg, cm

clear all
% Inputs
v0=input('enter impact velocity, cm/s  ');
gamma=input('enter soil buoyant unit weight, kg/cm^3  ');
load mmt.dat;  %XBP measurements
t=mmt(:,1);    %Time, msec, start from t=0
h=mmt(:,2);    %Depth, cm, start from h=0
a=-mmt(:,3);   %Deceleration, g
nt=length(t);
epsref=1.39/10000000; %Reference strain rate: 0.05%/hr
lambda=0.15; %Strain rate multiplier
dt=0.5/1000; %Time increment
d=5.0673; %Diameter of XBP,cm
W=0.544; %Weight of XBP,kg
h=h/d;
% Initialize
v(1)=v0;
x=[0,0.0195,0.059,0.1185,0.217,0.3155,0.4145,0.513,0.6115,0.7105,...
    0.809,0.9075,1.0065,1.105,1.2035];
%x is the depth used for interpolation
y=[0,0.1999,0.9649,2.6597,6.5165,11.6255,17.7709,24.8164,32.7174,...
    41.2456,50.2374,59.6665,69.3861,79.3021,89.3526];
%y is the volume of soil displaced by XBP corresponding to x
% For loop for penetration process
for i=1:nt
    if h(i)<=1.2035
        svol=interp1(x,y,h(i));
        fb(i)=gamma*svol/W;
        fs(i)=1-fb(i)-a(i);
    end
    if h(i)>1.2035
        svol=89.3526+pi*d*d/4*(h(i)-1.2035)*d;
        fb(i)=gamma*svol/W;
        fs(i)=1-fb(i)-a(i);
    end
% Strain rate correction
    src=1;
    if v(i)>epsref*d
        src=1+lambda*log10(v(i)/epsref/d);
    end;
    fs1(i)=fs(i)/src;
    if h(i)<=1.2035&h(i)>0
        su(i)=fs1(i)*W/(pi*d*d/4)/(10^0.932*(h(i)^0.756))*100/1.0197;
    end
    if h(i)>1.2035
        su(i)=fs1(i)*W/(pi*d*d/4)/(10^0.9822*(h(i)^0.2102))*100/1.0197;
    end
    if i>1
       su02(i-1)=su(i)*(1+lambda*log10(0.0224/epsref));
    end
```

```
    if i==nt
        break;
    else
       v(i+1)=v(i)+[a(i)+a(i+1)]/2*981*dt;
    end
end
h02=h(2:nt);
plot(su02,h02*d);
set(gca,'YDir','reverse');
ylabel('Depth (cm)','FontSize',12,'FontWeight','Demi');
xlabel ('Soil Strength (kPa)','FontSize',12,'FontWeight','Demi');
title('Soil Strength Profile','FontSize',14,'FontWeight','Demi');
```

APPENDIX F

A TYPICAL ABAQUS INPUT FILE (GENERATED BY ABAQUS CAE)

```
*Heading
** Job name: fr04 Model name: Model-1
*Preprint, echo=NO, model=NO, history=NO, contact=NO
**
** PARTS
**
*Part, name=Part-1
*End Part
**
** ASSEMBLY
**
*Assembly, name=Assembly
**
*Instance, name=Part-1-1, part=Part-1
*Node
      1,           0.,         -10.
      2,           0.,        -100.
      3,         100.,        -100.
                  ⋮
   6248,    3.895229,    -12.94132
   6249,    4.252222,    -13.79167
   6250,    4.176704,    -13.55151
*Element, type=CPE4
   1,  959,  742,  743,  960
   2,  620,  619,  378,  379
   3,  612,  627,  936,  626
                  ⋮
6057, 6240, 5276, 5316, 5432
6058, 6243, 5782, 5760, 5637
6059, 6248, 6246, 5645, 5614
** Region: (Section-1:Picked)
*Elset, elset=_PickedSet2, internal, generate
    1,  6059,     1
** Section: Section-1
*Solid Section, elset=_PickedSet2, material=Material-1
1.,
*End Instance
*Nset, nset=Set-1, instance=Part-1-1
   1,   5,   6,   7,   8, 292, 293, 294, 295, 296, 297, 298, 299, 300, 301, 302
 303, 304, 305, 306, 307, 308, 309, 310, 311, 312, 313, 314, 315, 316, 317, 318
 319, 320, 321, 322, 323, 324, 325, 326, 327, 328, 329, 330, 331, 332, 333, 334
 335, 336, 337, 338, 339, 340, 341, 342, 343, 344, 345, 346, 347, 348, 349, 350
 351, 352, 353, 354, 355, 356, 357, 358, 359, 360, 361, 362, 363, 364, 365, 366
 367, 368, 369, 370, 371, 372, 373, 374, 375, 376, 377, 378, 379, 380
```

```
*Elset, elset=Set-1, instance=Part-1-1
  2,  4,  6,  7,  9,  10,  12,  14,  16,  17,  19,  21,  24,  25,  26,  31
 38,  41,  43,  44, 228, 229, 233, 234, 235, 237, 242, 243, 246, 249, 250, 251
 253, 257, 259, 261, 262, 263, 264, 265, 266, 267, 268, 270, 271, 272, 273, 279
 280, 283, 285, 287, 289, 291, 292, 295, 296, 297, 300, 301, 303, 305, 306, 309
 310, 312, 480, 482, 485, 490, 491, 492, 500, 502, 503, 529, 531, 533, 537, 539
 541, 544, 547, 553, 557, 560, 563, 565, 567, 573, 585, 698, 811
*Nset, nset=_PickedSet5, internal, instance=Part-1-1
  1,  2,  9,  10,  11,  12,  13,  14,  15,  16,  17,  18,  19,  20,  21,  22
 23,  24,  25,  26,  27,  28,  29,  30,  31,  32,  33,  34,  35,  36,  37,  38
 39,  40,  41,  42,  43,  44,  45,  46,  47,  48,  49,  50,  51,  52,  53,  54
 55,  56,  57,  58,  59,  60,  61,  62,  63,  64,  65,  66,  67,  68,  69,  70
 71,  72,  73,  74,  75,  76,  77,  78,  79,  80,  81,  82,  83,  84,  85,  86
 87,  88,  89,  90,  91,  92,  93,  94,  95,  96,  97,  98,  99, 100, 101, 102
 103, 104, 105, 106, 107, 108, 109, 110, 111, 112, 113, 114, 115, 116, 117, 118
 119, 120, 121, 122, 123, 124, 125, 126, 127, 128, 129, 130, 131, 132, 133, 134
 135, 136, 137, 138, 139, 140, 141, 142, 143, 144, 145, 146, 147, 148, 149, 150
 151, 152, 153, 154, 155, 156, 157, 158, 159, 160, 161, 162, 163, 164, 165, 166
 167, 168, 169, 170, 171
*Elset, elset=_PickedSet5, internal, instance=Part-1-1
  5,  8,  18,  29,  30,  32,  35,  36,  37,  39,  40,  46,  47,  54,  58,  60
 63,  64,  67,  68,  70,  71,  72,  73,  74,  75,  76,  78,  80,  81,  82,  83
 84,  87,  90,  91,  93,  97, 108, 109, 110, 111, 112, 113, 114, 116, 118, 120
 122, 123, 124, 130, 134, 151, 152, 155, 158, 159, 163, 184, 186, 187, 188, 197
 201, 203, 204, 207, 208, 209, 211, 212, 213, 215, 216, 217, 219, 220, 221, 223
 225, 269, 274, 276, 284, 288, 304, 305, 307, 308, 318, 333, 335, 337, 339, 341
 343, 347, 349, 352, 353, 355, 359, 360, 364, 366, 367, 369, 371, 373, 375, 376
 378, 379, 383, 384, 415, 421, 427, 428, 431, 436, 438, 439, 442, 453, 460, 463
 468, 471, 543, 545, 548, 549, 551, 552, 554, 558, 559, 566, 569, 570, 571, 576
 582, 587, 595, 597, 600, 604, 610, 615, 659, 670, 671, 697, 702, 703, 857, 862
 866, 873, 906, 907
*Nset, nset=_PickedSet6, internal, instance=Part-1-1
  3,  4, 205, 206, 207, 208, 209, 210, 211, 212, 213, 214, 215, 216, 217, 218
 219, 220, 221, 222
*Elset, elset=_PickedSet6, internal, instance=Part-1-1
 101,  103,  105,  173,  177,  179,  180,  182,  183,  192,  193,  322,  327,  403,  408,
424
 623,  709, 1055
*Nset, nset=_PickedSet7, internal, instance=Part-1-1
  2,  3, 172, 173, 174, 175, 176, 177, 178, 179, 180, 181, 182, 183, 184, 185
 186, 187, 188, 189, 190, 191, 192, 193, 194, 195, 196, 197, 198, 199, 200, 201
 202, 203, 204
*Elset, elset=_PickedSet7, internal, instance=Part-1-1
 102, 125, 127, 129, 131, 136, 140, 141, 144, 145, 147, 149, 150, 152, 156, 161
```

```
 162, 164, 165, 168, 174, 176, 178, 180, 181, 323, 324, 326, 368, 374, 382, 390
 393, 405
*Nset, nset=_PickedSet8, internal, instance=Part-1-1
   1,   5,   6,   7,   8, 292, 293, 294, 295, 296, 297, 298, 299, 300, 301, 302
 303, 304, 305, 306, 307, 308, 309, 310, 311, 312, 313, 314, 315, 316, 317, 318
 319, 320, 321, 322, 323, 324, 325, 326, 327, 328, 329, 330, 331, 332, 333, 334
 335, 336, 337, 338, 339, 340, 341, 342, 343, 344, 345, 346, 347, 348, 349, 350
 351, 352, 353, 354, 355, 356, 357, 358, 359, 360, 361, 362, 363, 364, 365, 366
 367, 368, 369, 370, 371, 372, 373, 374, 375, 376, 377, 378, 379, 380
*Elset, elset=_PickedSet8, internal, instance=Part-1-1
   2,   4,   6,   7,   9,  10,  12,  14,  16,  17,  19,  21,  24,  25,  26,  31
  38,  41,  43,  44, 228, 229, 233, 234, 235, 237, 242, 243, 246, 249, 250, 251
 253, 257, 259, 261, 262, 263, 264, 265, 266, 267, 268, 270, 271, 272, 273, 279
 280, 283, 285, 287, 289, 291, 292, 295, 296, 297, 300, 301, 303, 305, 306, 309
 310, 312, 480, 482, 485, 490, 491, 492, 500, 502, 503, 529, 531, 533, 537, 539
 541, 544, 547, 553, 557, 560, 563, 565, 567, 573, 585, 698, 811
*End Assembly
**
** MATERIALS
**
*Material, name=Material-1
*Elastic
 5e+06, 0.499
*Plastic
400.,0.
**
** BOUNDARY CONDITIONS
**
** Name: BC-1 Type: Displacement/Rotation
*Boundary
_PickedSet5, 1, 1
** Name: BC-2 Type: Displacement/Rotation
*Boundary
_PickedSet6, 1, 1
** Name: BC-3 Type: Displacement/Rotation
*Boundary
_PickedSet7, 1, 1
_PickedSet7, 2, 2
** ----------------------------------------------------------------
**
** STEP: Step-1
**
*Step, name=Step-1
```

refined p/r=0.4

```
*Static
0.001, 1., 1e-05, 0.05
**
** BOUNDARY CONDITIONS
**
** Name: BC-4 Type: Displacement/Rotation
*Boundary
_PickedSet8, 1, 1
_PickedSet8, 2, 2, -0.5
**
** OUTPUT REQUESTS
**
*Restart, write, frequency=1
**
** FIELD OUTPUT: F-Output-1
**
*Output, field
*Node Output, nset=Set-1
COORD, RF, U
*Node Print, nset=Set-1
COORD, RF, U
**
** HISTORY OUTPUT: H-Output-1
**
*Output, history, variable=PRESELECT
*El Print, freq=999999
*Node Print, freq=999999
*End Step
```

VITA

Han Shi was born on August 9, 1975 in Huanggang, China. He received his Bachelor of Science degree in Hydrogeology & Engineering Geology from China University of Geosciences, Wuhan in July 1995. He received his Master of Science degree in Hydrogeology & Engineering Geology from China University of Geosciences, Wuhan in June 1998. His permanent address is: 93 D3 District, 202, Huazhong University of Science & Technology, Wuhan, Hubei 430074, China.